CHAR CRYSTALLINE TRANSFORMATIONS DURING COAL COMBUSTION AND THEIR IMPLICATIONS FOR CARBON BURNOUT

FINAL REPORT

Reporting Period Start Date: 07/01/1995 End Date: 06/30/1999

Author: Robert H. Hurt

Report Issue Date: 07/07/1999

DE-FG22-95PC95205--07

Robert H. Hurt
Division of Engineering
Box D"," Brown University
Providence, RI 02912-9104

Disclaimer

TABLE OF CONTENTS

1 Project Description 10
2 Project Background 12
3 Approach 19
4 Equipment Development 21
4.1 Transient Heat Treatment Device 21
4.2 High-speed Pyrometer 24
4.3 Graphite Heater Driver file Generator and Recorder 25
5 Thermal Annealing of Chars from Diverse Organic Precursors under Combustion-Like Conditions 35
5.1 Char Samples 35
5.2 Heat Treatments 36
5.3 Nonisothermal Thermogravimetric Analysis 37
5.4 High-Resolution Transmission Electron Microscopy 39
5.5 Results and Discussion 40
5.5.1 Example Normalized Rate of Weight Loss Profile 40
5.5.2 Effect of Hold Time at a Peak Temperature 42
5.5.3 Comparative Reactivity Loss for Various Precursors 45
5.5.4 Structural Evolution vs. Reactivity Loss 46
6 A Methodology for Analysis of 002 Lattice Fringe Images and Its Application to Combustion-derived Carbons 51
6.1 Image Analysis Algorithm 51
6.1.1 Digitization 51
6.1.2 Noise Reduction 53
6.1.3 Fringe Identification 54
6.1.4 Skeletonization and Post-Processing 56
6.2 Structure Parameters 64
6.2.1 Fringe Length 64
6.2.2 Tortuosity 65
6.2.3 Apparent Crystalline Fraction 66
6.2.4 Orientational Order Parameters 67

6.3 An Application to Combustion-derived Solid Fuel Chars 79
6.3.1 Sample Preparation 79
6.3.2 Quantitative Analysis of Structure 81
6.4 Reactivity and Structure Parameters 94
7 Conclusions 98
7.1 Characterization of Carbon Nanostructure 98
7.2 Transient Thermal Deactivation 100
8 References 102

LIST OF TABLES

Table 5-1. Properties of the Samples 36
Table 6-1 Dimensional calibrations and Resolution limits in Digitization 52
Table 6-2 Properties of the Solid Fuels and Chars..... 81

LIST OF FIGURES

Figure 2-1 Reactivities of various chars and residual carbon samples. Rates are for 100 μm particles in a selected standard combustion environment with a gas temperature of 1500 K, containing 6 mol% oxygen. The plot shows the systematically low reactivity of residual carbon samples from commercial-scale boilers..... 13

Figure 2-2 Dual-camera captive-particle image sequence for a typical Illinois #6 coal-char particle of roughly 200 μm in size burning in 6 mol% oxygen at a steady-state gas temperature of 1250 K. The sequence illustrates the asymptotic nature of char combustion, consisting of a rapid combustion phase followed by a near-extinction event and a slow final burnout phase..... 14

Figure 2-3 HRTEM lattice-fringe images of three partially reacted Illinois #6 coal chars after various residence times in the Sandia entrained flow reactor and a residual carbon sample from the flyash of a boiler using the same coal. 15

Figure 4-1 Sketch of the transient heat treatment apparatus: a) top view, b) graphite sheets and electrode (magnified), c) front view, and d) side view. 22

Figure 4-2 Schematic of the heating holder assembly. 23

Figure 4-3 Schematic illustration of the transient heat treatment experiment device and peripherals. 23

Figure 4-4 Unsteady, one-dimensional heat transfer calculation with 150 μm Anthracite particles inside: heat source temperatures were specified. 24

Figure 4-5 Optical fiber thermometer system: a) Pyrometer and b) Model 10 optical fiber thermometer system with a transmission cable. 25

Figure 4-6 Graphite Heater Driver file Generator (GHDG) program: a) Block diagram of the driver file generator and b) a front panel. 27

Figure 4-7 An example driver file from GHDG. Five regions are marked with module numbers. 28

Figure 4-8 a-f Modifiable regions of driver file by using different modules on the front panel of GHDG..... 32

Figure 4-9 A block diagram of the Graphite Heater Recorder (GHR). 33

Figure 4-10 Front panel of graphite heater recorder (GHR). 33

Figure 4-11 a) Typical driver file (broken line) and temperature profile (solid line) and b) hold time and HTT measurements..... 34
Figure 5-1 Maximum normalized weight loss rate $(-dm/dt)/m_i$ and as a function of initial sample weight (daf). Observed maximum rate is 0.001072 ± 0.000022 [sec^{-1}]..... 38
Figure 5-2 $Log_{10}\ k_o$ at two different carbon conversion levels, 20 and 50 % as a function of initial sample weight (daf). Observed reactivities at 20 % and 50 % are 6.78 ± 0.05 and 6.60 ± 0.03 [Log (sec^{-1})]. 39
Figure 5-3 Normalized rate of weight loss profiles for Pocahontas #3 (A), Illinois #6 (B), and Lykens valley #2 (C) char samples. Heat treatment temperatures (HTT) are shown in the legend box. The raw char sample was prepared by pyrolysis at 700 °C for 1 hr in flowing He in tube furnace. Heat treated char was prepared in the transient heat treatment device with 2.6 ± 0.4 second hold time at a peak temperature. 42
Figure 5-4 Effect of hold time for Beulah lignite (A) and Pocahontas #3 (B): $Log_{10}\ k_o$ at 20 % carbon conversion (daf) as a function of heat treatment temperature (HTT). Samples were heat treated up to a HTT at 1×10^3 deg/sec and held for a given time at the HTT. 44
Figure 5-5 $Log_{10}\ k_o$ at 20 % carbon conversion (daf) as a function of heat treatment temperature (HTT, °C). The reactivities of raw chars are plotted at 700 °C. The reactivities of fly ash samples (LOI = 20 ~ 40 %) and synthetic graphite are included. LOI stands for loss on ignition (weight loss percentage during air oxidation at 1270 K). 46
Figure 5-6 Reactivity as a function of heat treatment temperature: Pocahontas #3 and Lykens Valley #2. 47
Figure 5-7 HRTEM images from the heat treated samples: Lykens Valley #2; A-, B-, C-, and Pocahontas #3; D-, E-, F- corresponding reactivities are shown in Figure 5-6... 48
Figure 5-8 Processed images from selected HRTEM images: Lykens Valley #2, (A) raw char, (B) 1700 ºC HTD char, and (C) 2380 ºC HTD char. Pocahontas #3, (D) raw char and (E) 1870 ºC HTD char. 50
Figure 6-1 Raw, scanned fringe image of partially combusted coal char. 52
Figure 6-2 FT filtered image of Figure 6-1. 53

Figure 6-3 Effect of the threshold brightness on the number of identified fringes (from Figure 6-2). 55
Figure 6-4 Binary, filtered fringe image of partially combusted coal char. 56
Figure 6-5 Example skeletonization: objects are thinned in sequences of four passes, in which pixels are removed, without affecting the 8-connectivity of objects and removing the end pixels, from the top and left, the bottom and right, the bottom and left and the top and right in turn; the sequence is repeated until the image is stabilized. 57
Figure 6-6 Skeletonized fringe image of partially combusted coal char (from Figure 6-4). 58
Figure 6-7 An example of separation and removal. 58
Figure 6-8 An example of reconnection of the disconnected segments. 59
Figure 6-9 Mean crystallite dimension (L_a) from XRD and mean fringe length from HRTEM image analysis. 60
Figure 6-10 Processed fringe image of Figure 6-6 61
Figure 6-11 Raw and processed 002 LF image of high-rank, low-volatile bituminous coal char (Pocahontas) sampled from an entrained flow reactor in the early stages of combustion. Residence time: 47 msec; particle temperature: ~ 1700 K. Sample shows mesophasic long-range orientational order. (Smallest fringe shown is 5Å in length) 62
Figure 6-12 Raw and processed 002 LF image of lignite char generated by heat treatment at 2400 K in helium for four seconds. Sample shows primary short-range orientational order in the form of 5 – 10 nm domains along with low-grade statistical long-range orientational order among the domains. 63
Figure 6-13 Histogram of fringe length in Figure 6-10. 65
Figure 6-14 A box enclosing the fringe. 65
Figure 6-15 Histogram of tortuosity in Figure 6-10. 66
Figure 6-16 Simple orientational order modes among disk-like objects in three dimensions and their two dimensional projection. 68
Figure 6-17 Lines with random orientation generated with pseudo random function. 73

Figure 6-18 Nematic order parameter in two dimensions for sets of N randomly oriented lines (see Figure 6-17) as computed by stochasitic simulation. Analytical solution for $N = 2$ is $S_{2N} = 2/\pi$. The Shim function shown is used to define a corrected nematic order parameter for small sample sets that has an expected value of zero for random orientations. 74
Figure 6-19 Nematic order parameter (S_{m2N}) as a function of length scale from Figure 6-10. 75
Figure 6-20 A distribution of S_{m2N} with 2.5 nm, r_c in Figure 6-10. 76
Figure 6-21 Schematic of the conceptual polar order parameter calculation: u_i is a direction unit vector of fringe i, and r_i positional unit vector relative to the pole..... 77
Figure 6-22 a) and b): Raw and processed 002LF image of ethylene soot provided courtesy of Adel Sarofim and Lenore Rainey at MIT. Sample shows characteristic concentric order. c) Application of polar order parameter to the ethylene soot fringe image. Two dimensional map of S_{2P} yields the optimal pole-the apparent nucleus of the concentric structure. 78
Figure 6-23 Calculation of length dependent polar order parameter at the optimum pole from Figure 6-22 c). Positive values indicate concentric order (rather than radial order) and the extent of order increases with distance from the nucleus. 79
Figure 6-24 Example carbon nanostructures observed in young combustion-generated chars. Residence time: 47 msec; Particle temperatures: 1700 – 1900 K. Circle with embedded line gives the director for the entire field shown. 83
Figure 6-25 Example carbon nanostructures observed in combustion-generated chars from later times. Residence time: 117 msec (or 95 msec as marked with *); particle temperatures: 1700 – 1900 K 84
Figure 6-26 Set of four images from Beulah lignite char (residence time: 72 msec), demonstrating the degree of variability in fringe images within a single sample. 85
Figure 6-27 Summary of results for combustion-derived chars: mean fringe length vs. combustion residence time. Note: zero residence time represents the raw solid fuel. Image-to-image standard deviations are 1 – 3 Å, so the changes between range 47 and 117 msec are not statistically significant for some precursors. 86

Figure 6-28 Summary of results for combustion-derived chars: mean tortuosity vs. combustion residence time. Note: zero residence time represents the raw solid fuel. 87
Figure 6-29 Summary of results for combustion-derived chars: apparent crystalline fraction vs. combustion residence time. Apparent crystalline fraction is the fraction of the image area covered by recognizable ordered material and is calculated as $SL_i/(SL_i)_{max}$ where $(SL_i)_{max}$ is computed for an ideal graphitic structure. 88
Figure 6-30 Nematic order parameter (S_{m2N}) of Pocahontas #3 and Illinois #6 chars as a function of length scale. 89
Figure 6-31 Distribution of S_{m2N} for Illinois #6 char samples as a function of residence time with 5 nm dia. over whole area in the image. 90
Figure 6-32 Distribution of S_{m2N} fraction in Pocahontas #3 as a function of residence time with 5 nm dia. over whole area in the image. 91
Figure 6-33 Summary of results for combustion-derived chars: modified, length-dependent nematic order parameters, S_{m2N} (r), for chars from six solid fuels. (72 msec for coal chars, 95 msec for biomass chars). 93
Figure 6-34 Global reactivity as a function of mean fringe length. Char samples were at the residence time of 72 msec. * RC: residual carbon from fly ash. 95
Figure 6-35 Reactivity as a function of tortuosity. 96
Figure 6-36 Global reactivity as a function of fraction with $S_{m2N} > 0.6$ with a given 5 nm region of interest. 97

1 PROJECT DESCRIPTION

Residual, or unburned carbon in fly ash affects many aspects of power plant performance and economy including boiler efficiency, electrostatic precipitator operation, and ash as a salable byproduct. There is a large concern in industry on the unburned carbon problem due to a variety of factors, including low-NO× combustion system and internationalization of the coal market.

In recent work, it has been found that residual carbon extracted from fly ash is much less reactive than the laboratory chars on which the current kinetics are based. It has been suggested that thermal deactivation at the peak temperature in combustion is a likely phenomenon and that the structural ordering is one key mechanism. The general phenomenon of carbon thermal annealing is well known, but there is a critical need for more data on the temperature and time scale of interest to combustion. In addition, high resolution transmission electron microscopy (HRTEM) fringe imaging, which provides a wealth of information on the nature and degree of crystallinity in carbon materials such as coal chars, has become available. Motivated by these new developments, this University Coal Research project has been initiated with the following goals: 1) To determine transient, high-temperature, thermal deactivation kinetics as a function of parent coal and temperature history. 2) To characterize the effect of the thermal treatment on carbon crystalline structure through high-resolution transmission electron microscopy and specialized, quantitative image analysis. Works included the following three tasks:

Task 1. Experimental technique development.

A new apparatus has been developed for measuring transient, high-temperature, thermal deactivation of coal chars. While peak gas temperatures in boilers are often in the range 1800 - 2000 K, peak particle temperatures can be much higher due to high rates of heat release at the particle surface due to exothermic carbon oxidation. The newly developed transient heat treatment apparatus is based on an inert-gas purged graphite-sheet sample holder that is subjected to rapid Joule heating to temperatures approaching

3000 °C. Oxidation kinetics is measured on the heat treated samples by a nonisothermal TGA technique.

Task 2. Thermal deactivation measurements

The goal of this task was to measure thermal char deactivation as a function of temperature history and parent coal, with an emphasis on inert environments at temperatures and times found in combustion systems. The results are expected to find use in combustion models.

Task 3. Crystalline structure characterization

Crystalline structure characterization provides important insight into the mechanisms of thermal char deactivation, and the degree of crystalline transformations has shown a strong correlation with reactivity changes in recent combustion studies [2,12]. This task seeks to improve our understanding of char carbon crystalline transformations under combustion conditions by analyzing a large set of HRTEM fringe images for a series of flame-generated chars whose reactivities have been previously reported [1,2]. As a first step, a new technique has been developed for the quantitative analysis of fringe images, extending previous work to allow measurement of a complete set of crystal structure parameters including mean layer size, mean stacking height, interlayer spacing, layer curvature, amorphous fraction, and degree of anisotropy. The resulting database reveals, at a very fundamental level, the basic differences in char crystal structure due to parent coal rank and to temperature history in the range of interest to combustion systems.

This final report summarizes the above three works during the course of the project.

2 PROJECT BACKGROUND

Recent laboratory studies have provided valuable new insight into the unburned carbon problem. First, residual carbon extracted from boiler fly ash samples has been found to be much less reactive than the laboratory chars on which the existing kinetic measurements are based [1]. This is illustrated in Figure 2-1, which compares residual carbon samples extracted from boiler fly ash (open symbols) with a range of laboratory chars used to generate the existing kinetic database (closed symbols). Residual carbon—that fraction of the parent fuel that passes through a boiler unreacted—is seen to be less reactive than the corresponding laboratory chars by factors of up to seven. It appears that some mechanism is responsible for deactivating chars during their passage through the boiler, making the final burnout of the last portion of the carbon much more difficult to achieve. The only property of the residual carbon samples which appears to correlate with their low reactivity is the degree of crystalline order. Currently, the most promising explanation for this low reactivity is thermal deactivation at peak particle temperatures in the lower furnace region [2].

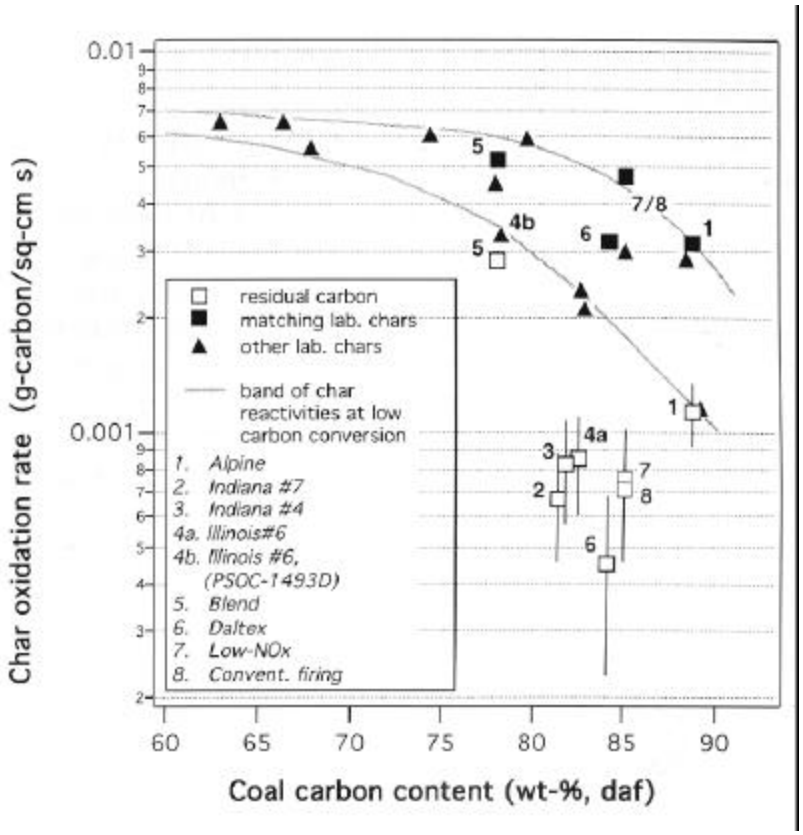

Figure 2-1 Reactivities of various chars and residual carbon samples. Rates are for 100 μm particles in a selected standard combustion environment with a gas temperature of 1500 K, containing 6 mol% oxygen. The plot shows the systematically low reactivity of residual carbon samples from commercial-scale boilers.

This initial result spawned several new efforts to account for thermal deactivation and its implications. Researchers at PowerGen, one of the two privatized utilities in the U.K., in collaboration with the University of Nottingham, have independently measured and confirmed the low reactivity of residual carbon [3]. A research group at Imperial College has also confirmed the low reactivity of residual carbon [2] and has proposed high temperature heat treatment as a test for burnout propensity of unknown coals [4]. The general phenomenon of deactivation by thermal annealing has been observed in numerous laboratory studies [5, 6, 7]. Several studies have noted the importance of thermal annealing in entrained flow combustion [8, 9]. Most of the previous data, however, is not directly relevant to the very short times and high temperatures found on particle surfaces in pulverized-coal-fired boilers.

Follow-up work at Sandia National Laboratories has documented reactivity losses and extinction phenomena occurring during laboratory combustion under simulated boiler conditions. These controlled laboratory studies have shown that char combustion can be regarded as a two-stage process, consisting of a rapid combustion phase followed by a near-extinction event and a slow final burnout phase that occurs at lower temperatures [10, 11], as illustrated in Figure 2-2. In addition, an exciting new technique, HRTEM fringe imaging has been applied to study the nature of the crystalline rearrangements that underlie the thermal deactivation process [12], as shown in Figure 2-3.

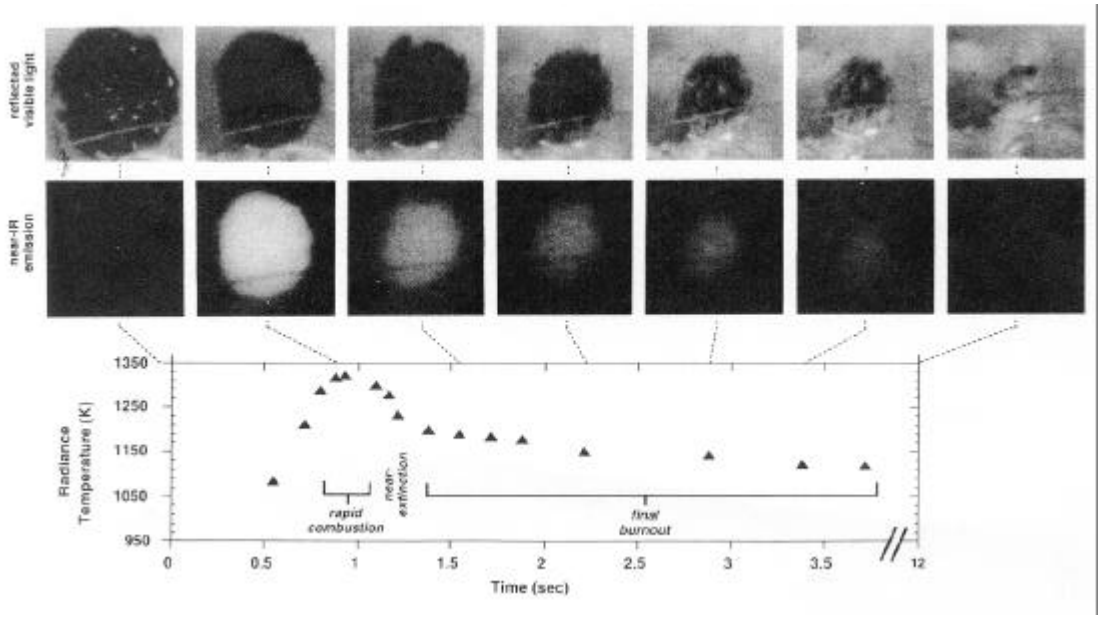

Figure 2-2 Dual-camera captive-particle image sequence for a typical Illinois #6 coal-char particle of roughly 200 μm in size burning in 6 mol% oxygen at a steady-state gas temperature of 1250 K. The sequence illustrates the asymptotic nature of char combustion, consisting of a rapid combustion phase followed by a near-extinction event and a slow final burnout phase.

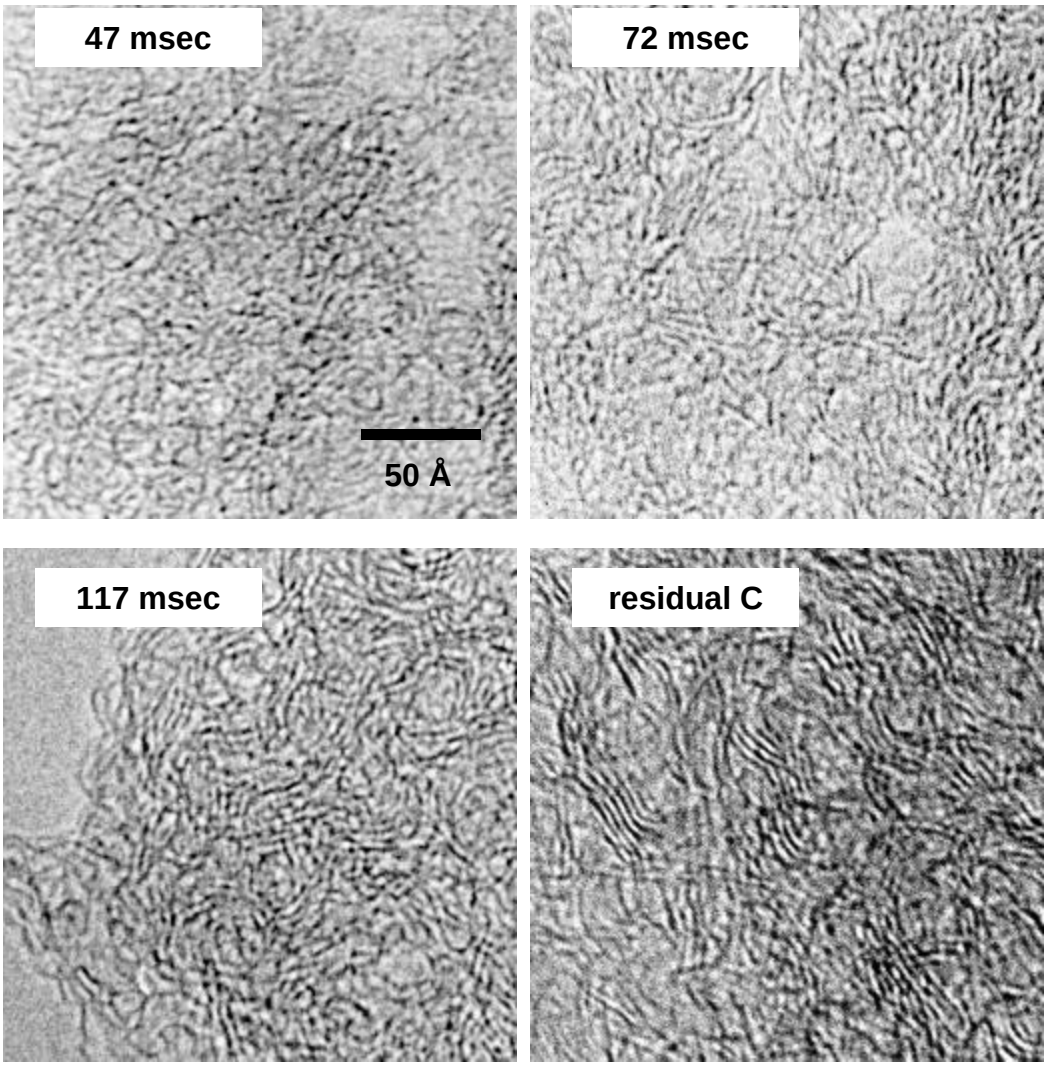

Figure 2-3 HRTEM lattice-fringe images of three partially reacted Illinois #6 coal chars after various residence times in the Sandia entrained flow reactor and a residual carbon sample from the flyash of a boiler using the same coal.

Crystal structure has long been recognized as an important contributing factor to carbon reactivity [6, 7, 13]. Although the degree of crystallinity does not appear explicitly in the fundamental equation governing global reactivity, it affects many of the terms, including intrinsic surface reactivity, microporous surface area (which is the dominant contributor to total surface area), and possibly microporous diffusion coefficient [14]. Crystallite growth is generally associated with loss of active sites, both at crystallite edges and in the form of basal plane defects. Indeed, across the spectrum of

carbon materials, reactivity tends to decrease with increasing degree of crystalline order [5, 6, 7, 8, 15]. HRTEM fringe imaging is a very powerful technique for probing the crystalline structure of carbons [16], but has only recently been applied to coal char transformations during combustion [12]. It has been applied to carbonaceous materials in order to understand the graphitization mechanism [16]. But the conditions employed in combustion are quite different from those conditions used in graphitization studies; i.e., high heating rate, 1×10^5 K/sec, and short time scales, 100 msec.

HRTEM fringe images yield a wealth of information on the degree and nature of crystallinity in carbons, including interlayer spacings, the diameters of the graphitic layers, and the extent of parallel alignment of neighboring layers (stacking heights). In another recent study, the degree of crystalline order in coal chars has been observed to increase steadily as laboratory combustion proceeds over the first 120 msec at peak particle temperatures from 1800 - 2000 K [12]. Oxygen has been shown to suppress mesophase formation and graphitization [17]; this suggests that deactivation and structural ordering may be very rank dependent. Indeed Wornat et al. [18], observed that highly oxygenated, cross-linked chars derived from biomass show only limited ordering during combustion. Digital analysis of HRTEM images has been shown to be more effective than X-ray diffraction for characterizing carbon crystalline transformations during combustion of Illinois #6 coal [12]. The very limited data suggest that HRTEM may be a useful diagnostic for correlating reactivity of flame chars.

To summarize the preceding discussion, it is possible that the high-temperature environment in boilers causes ultrafine rearrangements in char carbon that lead to a more crystalline structure and lower reactivity in the later stages of combustion. The detailed temperature history early in the lifetime of a char particle determines its reactivity in the late stages of combustion and thus the degree of difficulty in achieving high burnout. Annealing in the boiler may occur quickly, at the peak flame temperature, or more gradually over the course of combustion.

Char deactivation by pregraphitization has the following potentially important implications for combustion systems:

- It is intrinsically more difficult to achieve high carbon burnout than is predicted by models based on laboratory char oxidation kinetics. New models are needed for design and retrofit applications on current and future combustion systems.
- To identify problem coals with respect to carbon burnout, one must consider both their early combustion reactivity (as is commonly measured in the laboratory) and the propensity of the char to pregraphitize and deactivate at high temperature. However, very little is known about the reactivity of high-temperature chars (carbonized at 2000 - 2400 K for 100 - 1000 msec) from coals of various ranks and types. A database is needed on high temperature chars in order to identify coal properties that signal potential problems with carbon burnout, to aid in fuel selection.
- Char reactivity may be affected by changes in the structure of the flame zone in a boiler. For example, high peak flame temperatures may accelerate combustion only slightly (as the heterogeneous reactions become limited by boundary-layer diffusion at high temperature), but may promote char pregraphitization and deactivation, making subsequent complete burnout in the upper furnace region more difficult to achieve. This suggests that there is an optimum flame temperature for burnout. Pregraphitization may be especially detrimental in low NO_x systems, where oxidation is delayed and an opportunity may be lost to rapidly consume the young, reactive char. These insights pose the possibility of tailoring the flame zone of a furnace to minimize unburned carbon levels.

The role of thermal annealing, or char deactivation in the lower furnace, has not been fully appreciated in the design and optimization of today's combustion equipment. Thus there is great potential for using these new insights to rationally optimize new furnace designs and retrofits for both NO_x control and carbon burnout. The recent work described dramatically illustrates the importance of char deactivation in boilers. Quantitative kinetics is now needed in order to determine the implications for furnace design and operation. The work to date has been carried out under true combustion conditions involving simultaneous oxidation and heat treatment, and as a result, the deactivation cannot be definitively attributed to either oxidation or heat treatment alone. In order to formulate useful engineering models, fundamental quantitative heat treatment experiments are needed that decouple oxidation from thermal effects. More research is

also needed to pursue the transformations of carbon crystalline structure under combustion conditions and its relationship to carbon burnout. The initial work has demonstrated the usefulness of HRTEM fringe imaging and more recent work has generated a database of fringe images for a time-resolved series of partially-combusted chars from four coals and two biomass fuels. The very limited data suggest that HRTEM may be a useful diagnostic for correlating reactivity of flame chars, but much more work is needed in this new area. And fundamental understanding on the nanostructure transformation under rapid heating condition is new in the carbon research field. Quantitative analysis is needed to establish relationships between crystalline structural parameters and reactivity from the existing database and to further the state-of -the-art in the application of fringe imaging to combustion problems.

Motivated by these new developments, research has been performed with the following goals:

1. To make the first kinetic measurements of thermal deactivation at temperatures equivalent to peak particle temperatures in commercial pulverized coal-fired boilers,
2. To characterize quantitatively the effect of the thermal treatment and the oxidation on carbon crystalline structure using HRTEM, and to establish fundamental relationships between crystalline structure and reactivity.
3. To understand the transformation of carbonaceous nanostructure under rapid heating conditions.

3 APPROACH

Thermal deactivation studies were pursued using a newly developed heat treatment apparatus. In order to better understand deactivation mechanisms, fundamental heat treatment experiments in inert environments are needed which decouple oxidation from thermal effects. The deactivation study here, therefore, was performed with an emphasis on inert environments at temperatures and times found in combustion systems. The usefulness of such experiments has been demonstrated in recent works by Beeley et al. [2].

While peak gas temperatures in boilers are often in the range 1800 - 2000 K, peak particle temperatures can be much higher due to high rates of heat release at the particle surface due to exothermic carbon combustion. Recent examinations of particle temperature histories from detailed numerical simulations have revealed peak particle temperatures up to 2400 K in some full-scale boilers [19]. At present, there are no data on the reactivities, structure, or properties of chars heated to these extremely high temperatures (~ 2400 K) for very short times (< 1sec). Well controlled experiments are needed at these temperatures to quantify deactivation. A new apparatus, described in the following section has been developed in our laboratory for the high temperature experiments.

A quantitative digital image analysis technique has been developed for fringe images. Fringe images used in this study included previously published images of samples in Sandia National Lab's entrained flow reactor simulating industrial combustion process conditions [12, 18, 20]. There have been several attempts to apply digital image analysis to lattice fringe images, with promising results [12, 21, 22]. For example, Davis et al. [12] has determined crystallite diameters using object-oriented algorithms as well as the fractions of amorphous and crystalline carbon. The authors state that more work is needed to make the results fully quantitative. In this work we expanded on the previous work to make measurements of other important crystalline structure parameters, including fringe length, degree of curvature, and degree of anisotropy. Although HRTEM has been extensively used for the study of carbonaceous materials and the graphitization or pregraphitization process, little work has been reported that describes

the structural evolution of carbon on time scales relevant to pulverized-coal combustion. The investigation presented here has extended the use of this technique to partially reacted products of coal combustion and clarified the phenomena of char deactivation during pulverized-coal combustion.

4 EQUIPMENT DEVELOPMENT

4.1 Transient Heat Treatment Device

The device is based on two thin graphite sheets held at the ends by brass electrodes connected to a DC power supply (see Figure 4-1 b and Figure 4-3). The powdered carbon samples are sandwiched between the two graphite sheets, which act as an electrical resistance heater, to ensure that there is a direct contact between the heat source and the sample (see Figure 4-1-b and Figure 4-2). To prevent sample loss and give a possible gas path at the same time, the sample is placed in the rectangular frame of carbon cloth (Technical Fibre Products Ltd., NY, USA). The surface of the lower graphite sheet is optically accessible from beneath for temperature measurement. The electrode is evacuated (~ 0.5 torr) in a chamber covered with a heavy glass jar (Figure 4-1 c) and purged with an inert gas to prevent sample, graphite, or electrode oxidation while the center section is at high temperature. A high-speed pyrometer is used to measure the temperature of the surface of the lower graphite sheet. The pyrometer is capable of measuring temperatures of 450 °C - 3000 °C at 30 readings per second operating at 10 kHz. Tests with a temperature indicating liquid (OMEGALAQ™) showed that the temperature is measured within ± 13 °C.

The thermal history of the sample is determined by measuring the surface temperature of the graphite sheet. The calculated interior heat-up time to the target temperature, assuming uniform interior properties and unsteady, one-dimensional heat transfer, is less than 50 msec in the temperature range of interest (1000 ~ 3000 °C, See Figure 4-4). Calculations with the Stefan-Boltzmann law showed that this device can reach a maximum temperature over 3000 K at heating rate > 10^4 K/sec, and this can be changed by adjusting the geometric parameters, w and L_h (heated area) of the graphite sheet (See Figure 4-1-b). Peak flame temperature in boilers are often in the range of 1800 ~ 2000 K. With w=1.0 cm and L_h=1.0 cm, the heat treatment device in a test run could reach ~ 2800 °C at a heating rate of 1.4×10^3 deg/sec.

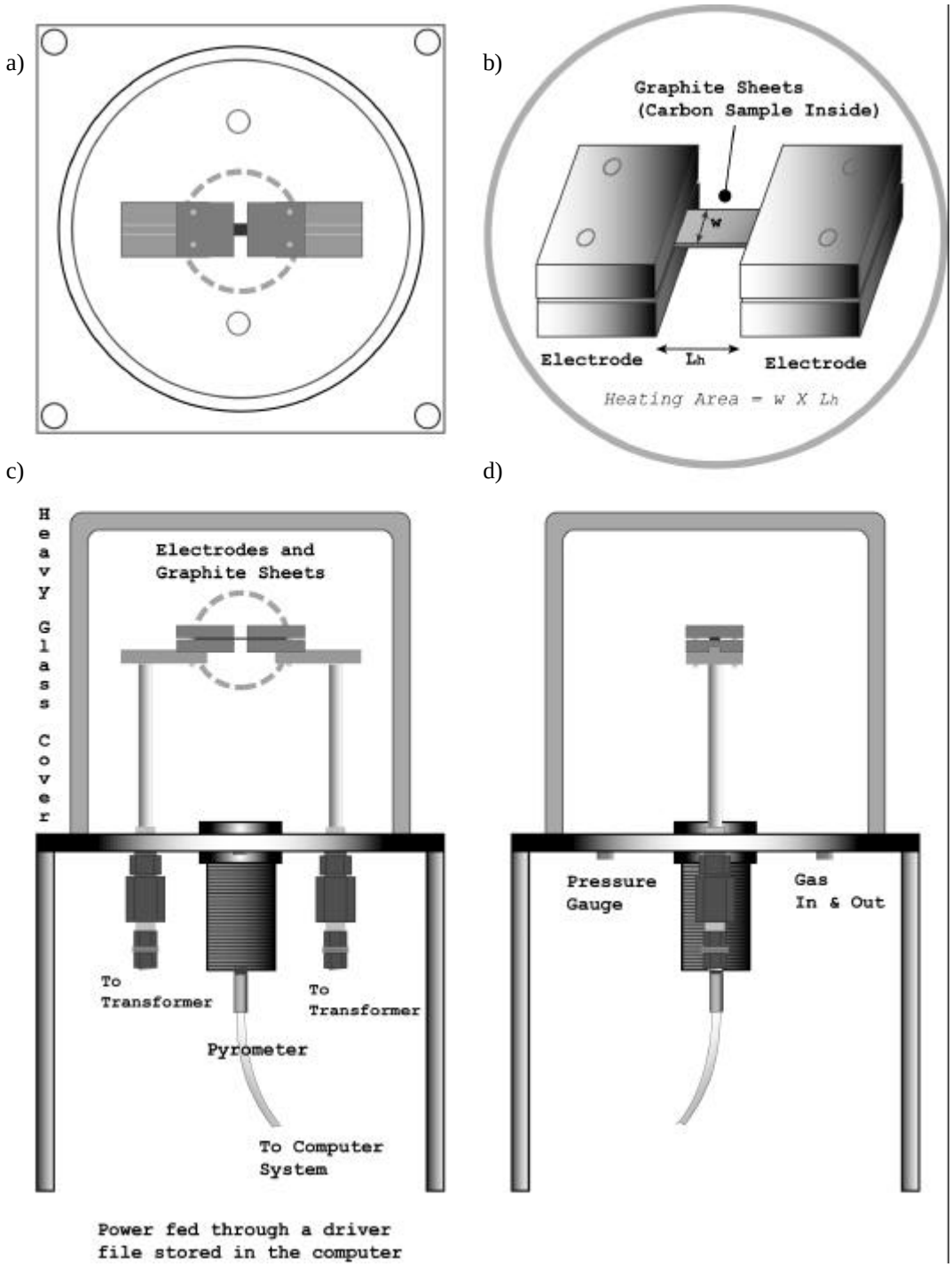

Figure 4-1 Sketch of the transient heat treatment apparatus: a) top view, b) graphite sheets and electrode (magnified), c) front view, and d) side view.

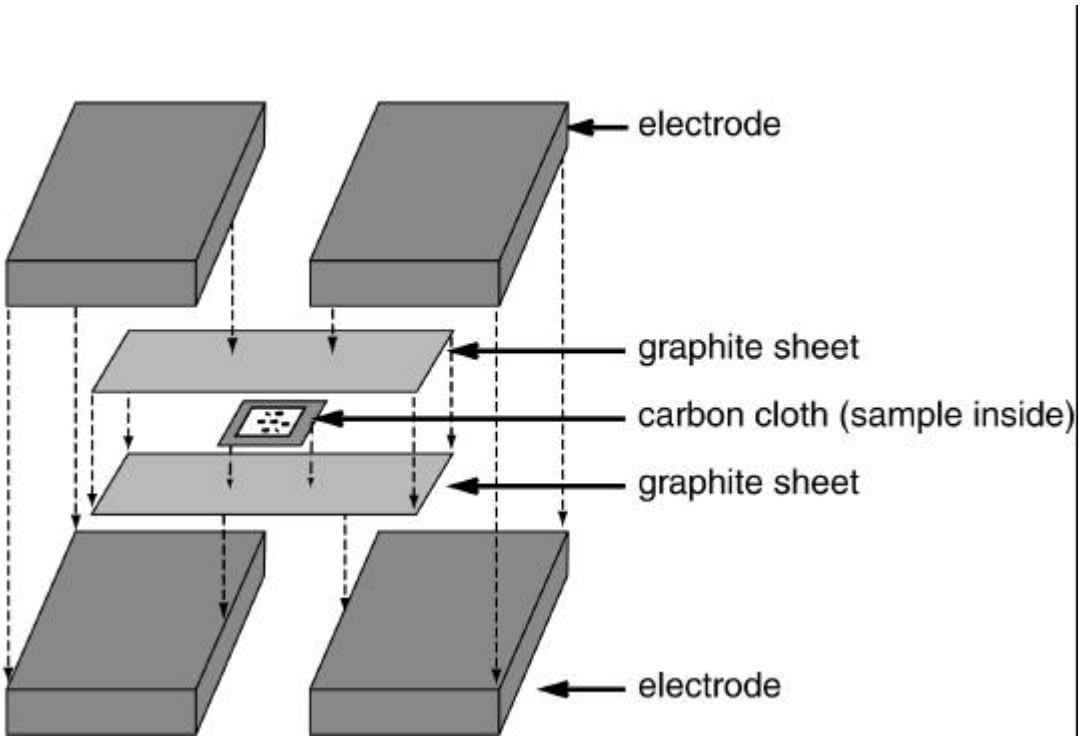

Figure 4-2 Schematic of the heating holder assembly.

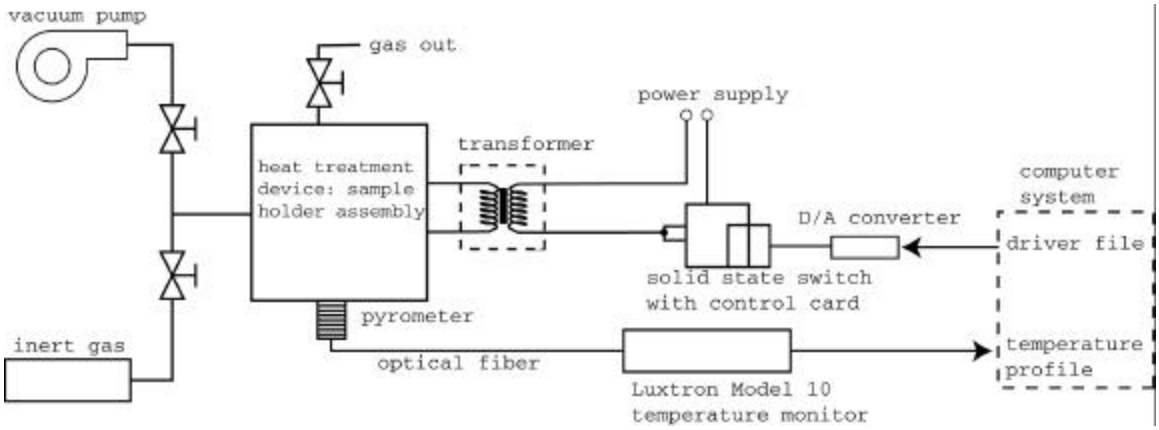

Figure 4-3 Schematic illustration of the transient heat treatment experiment device and peripherals.

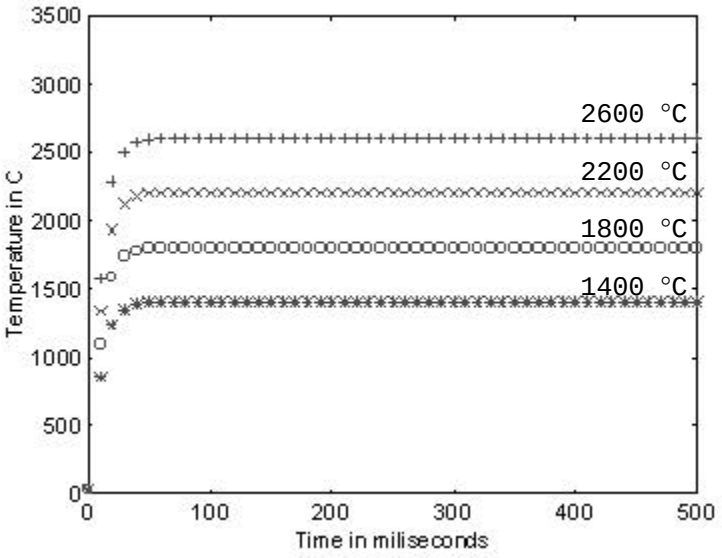

Figure 4-4 Unsteady, one-dimensional heat transfer calculation with 150 μm Anthracite particles inside: heat source temperatures were specified.

This heat treatment apparatus is operated by two computer programs, graphite heater driver file generator (GHDG) and graphite heater recorder (GHR). The first program generates a driver file for heating. The latter program reads a driver file, runs the heat treatment device according to the driver file, and simultaneously reads the signal from the pyrometer at the same time.

4.2 High-speed Pyrometer

Temperature measurement is made by an optical fiber thermometer from LUXTRON™. The system includes Model 10 optical fiber thermometer system and optical pyrometer sensor (Figure 4-5).

The readable temperature range is 450 ~ 3000 ºC at 10 readings/sec. Optical pyrometer sensor uses 600 micron transmission cable and has 2 mm target diameter and 15.2 cm lens to target distance. The pyrometer is located below and is focussed on the lower graphite sheet's center (see Figure 4-1).

a)

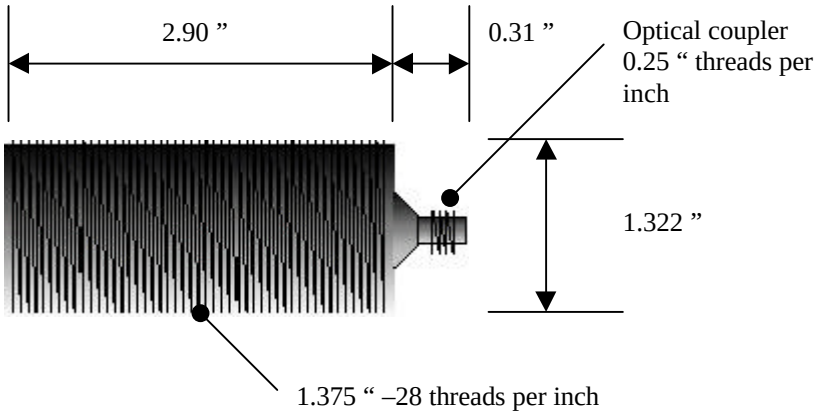

b)

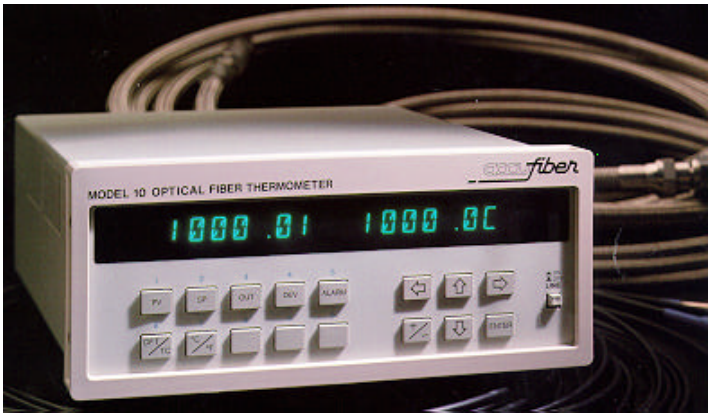

Figure 4-5 Optical fiber thermometer system: a) Pyrometer and b) Model 10 optical fiber thermometer system with a transmission cable.

Tests with a temperature indicating liquid (OMEGALAQ™) showed that the temperature can be measured within ±13 °C.

4.3 Graphite Heater Driver file Generator and Recorder

Graphite heater driver file generator (*GHDG*) and recorder (*GHR*) were programmed using LabVIEW™. LabVIEW is a program development application using a graphical programming language, G, to create programs in block diagram form. It includes libraries of functions and development tools designed specifically for data acquisition and instrument control.

The purpose of *GHDG* is to generate a voltage curve to be fed to the heat treatment device, which is called a *driver file*. It calculates necessary voltage for the electrode to reach a target temperature, a heating rate, holding time, and cooling time assuming the heating area of the graphite sheets is 1.1 cm (L_h) by 1.0 cm (w) and 0.0381 cm in thickness of each graphite sheet. Depending on the variation of the graphite sheets' geometry and a sample property, a real measured temperature profile might be different to the expected temperature profile. In a test, the resultant temperatures showed 100 ~ 200 ºC higher than the target temperature in *driver file*, using the mentioned graphite sheets' geometry (L_h and w).

The block diagram and the front panel of *GHDG* are shown in Figure 4-6-a and b. The front panel simulates the panel of a physical instrument. It consists of 6 modules (1-5 and E), which will be described in detail later in this section.

a)

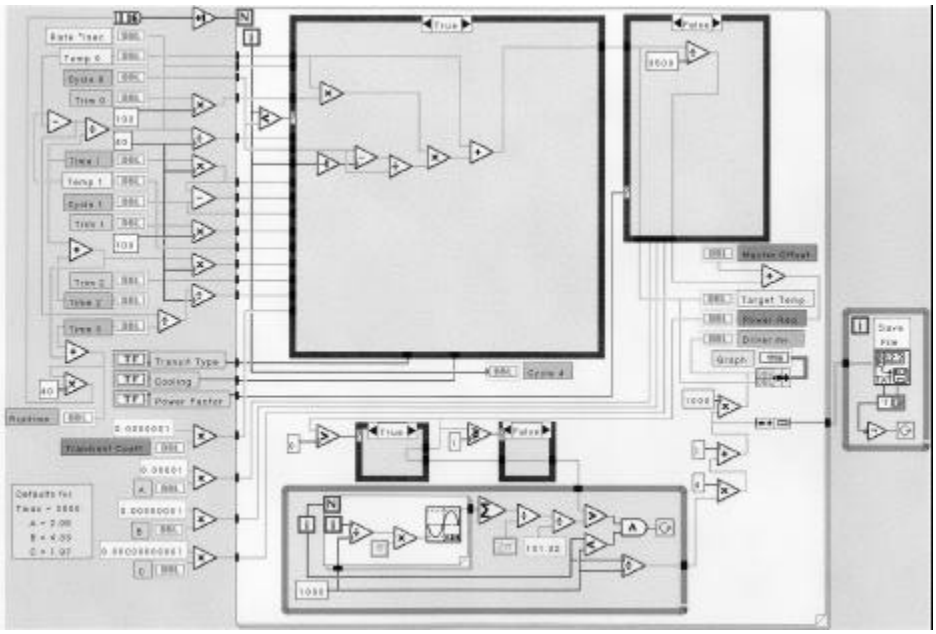

Figure 4-3 (CONTINUED)

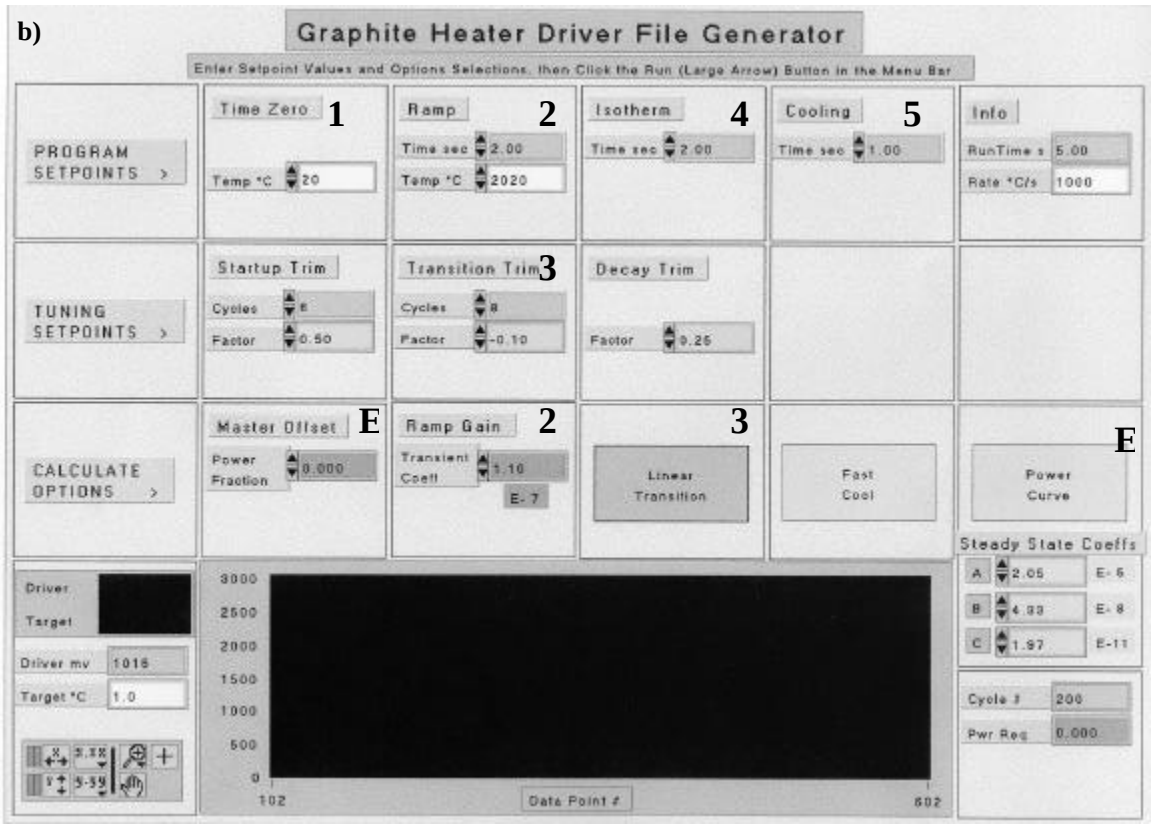

Figure 4-6 Graphite Heater Driver file Generator (GHDG) program: a) Block diagram of the driver file generator and b) a front panel.

An example driver file is shown in Figure 4-7. The shape of a driver file is made of 5 modifiable regions, as shown in Figure 4-7 : Region 1: an initial warm-up stage for the electrode; 2: ramping or heating stage; 3: transition from heating stage to an isothermal stage; 4: isothermal stage; and 5: cooling stage. Matching control module numbers are also specified on a front panel (see Figure 4-6 b).

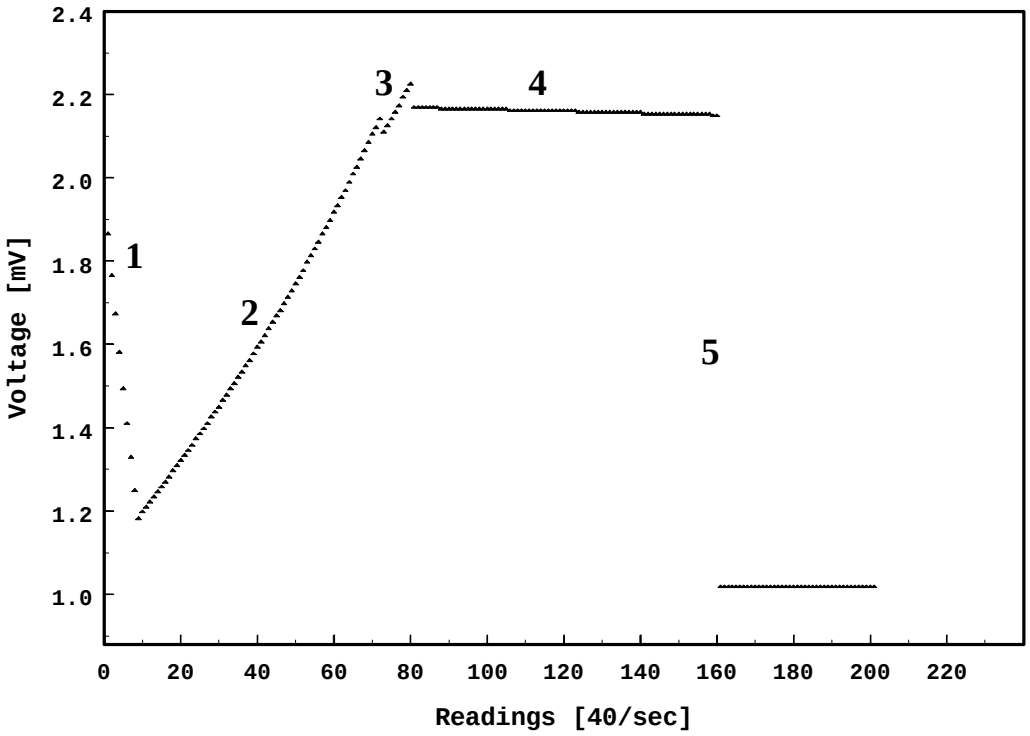

Figure 4-7 An example driver file from GHDG. Five regions are marked with module numbers.

The usage of the modules is described in the following.

In module 1, there are three values to choose, including an initial temperature in Celsius (default value is 20 ºC), startup trimming parameters, and the number of *cycles* and *factor*. An initial temperature is specified to simulate the ambient temperature. This region 1 is a warm up stage for the electrode. Ending points of region 1 and a junction to region 2 can be adjusted by increasing or decreasing the number of cycles, as shown in Figure 4-8 a. By increasing the factor in module 1 on the front panel (see Figure 4-6-b), a starting voltage becomes higher.

In module 2, which shapes region 2 in Figure 4-7, titled as *Ramp* and *Ramp gain* on the front panel, characteristics of a ramping or heating of a driver file can be specified (see Figure 4-6). In *Ramp*, the target temperature and the time duration to reach that temperature are specified. This step, basically, determines a heating rate. In *Ramp gain*,

a factor of a power supply up to the target temperature can be adjusted as shown in Figure 4-8 b. Increased factor results in over shoot with respect to the target temperature.

In module 3, which trims a transition between heating and holding stage, which are region 2 and 4, respectively. Increase in the number of *cycles* in *Transition Trim* causes the end points of region 2 decrease, but initial points of region 3 increase, as shown in Figure 4-8 c. By increasing a factor of the trim, magnitude of voltage increases but with the same slope as in *default*. Two kinds of transition type are implemented in the program, which are *linear* and *dip* transition. A default, as shown in Figure 4-8 c is *dip* transition. A selection of *linear* transition changes the slope to negative.

In module 4, a *holding time* in seconds at the *target temperature* and *decay trim factor* are specified. Increasing factor makes decays of the curve in isothermal region 4 faster, as shown in Figure 4-8 d. The decay function is decided partly in module E, which will be described later.

In module 5, characteristics of cooling are determined by specifying a cooling time and controlled or uncontrolled cooling. *Fast* cool (default mode) stops a current feeding right after the isothermal region (see Figure 4-8 e). In this case, the specified cooling time doesn't affect the shape of the curve. *Slow* cool is controlled and is determined by the cooling time and the target temperature specified earlier. It, basically, draws a linear curve from the target voltage to the initial voltage, which are converted from the target temperature and the initial temperature, respectively.

In module E, overall shape can be adjusted. The cases when *linear power* mode (a default is *power curve*) is selected, *master offset* is increased and *A*, *B*, or *C* values are increases are shown in Figure 4-8 f. Increase in *master offset* changes the region 1, 2 and the final stage. *Linear power* mode shifts the curve to higher magnitude and changes the shape of region 2. By changing the values in A, B, and C, the shape of region 2, 3, and 4 can be changed.

a)

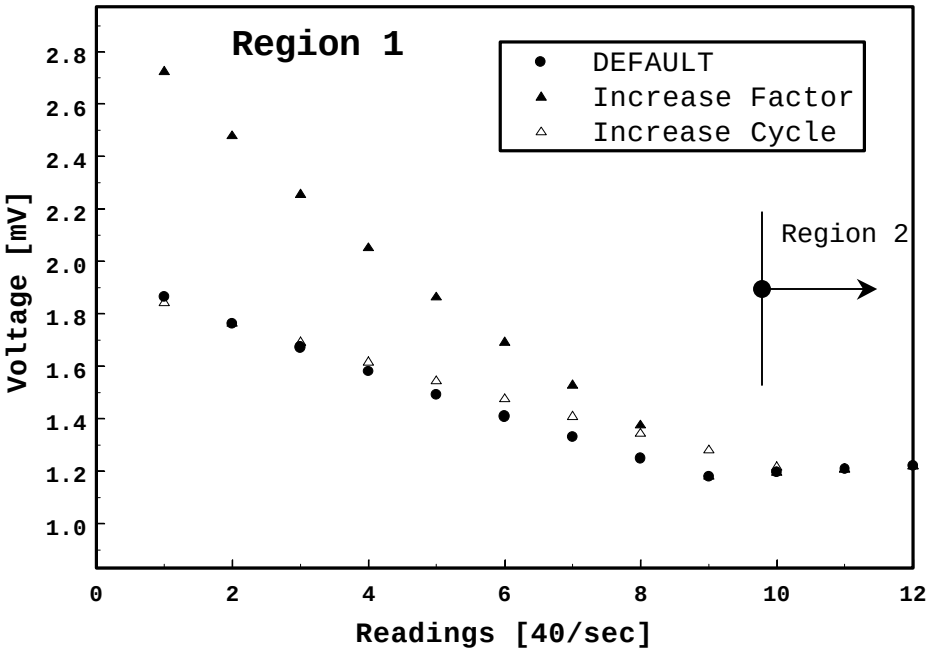

b)

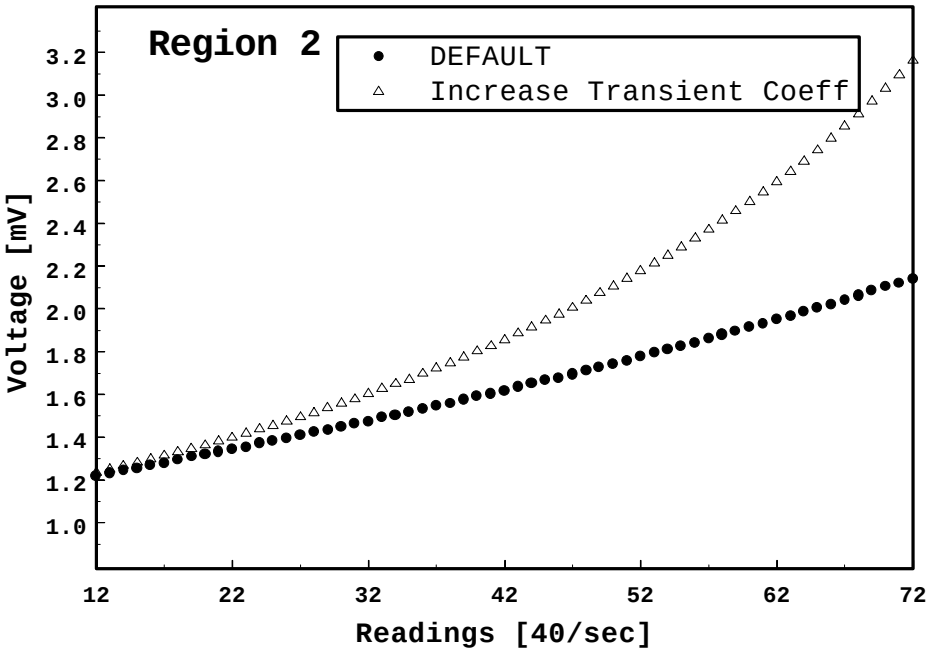

Figure 4-8 a and b (continued)

c)

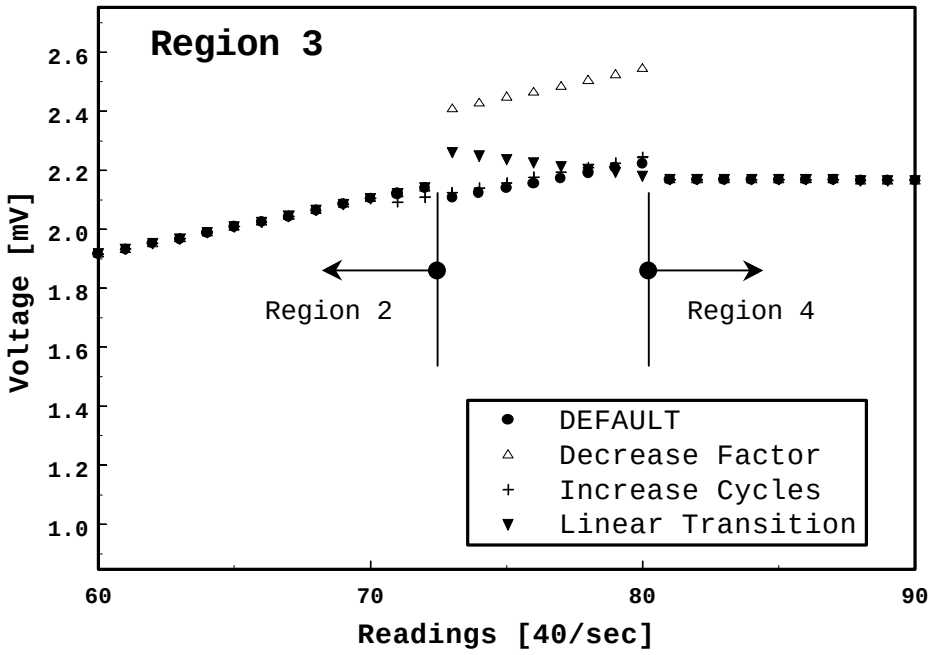

d)

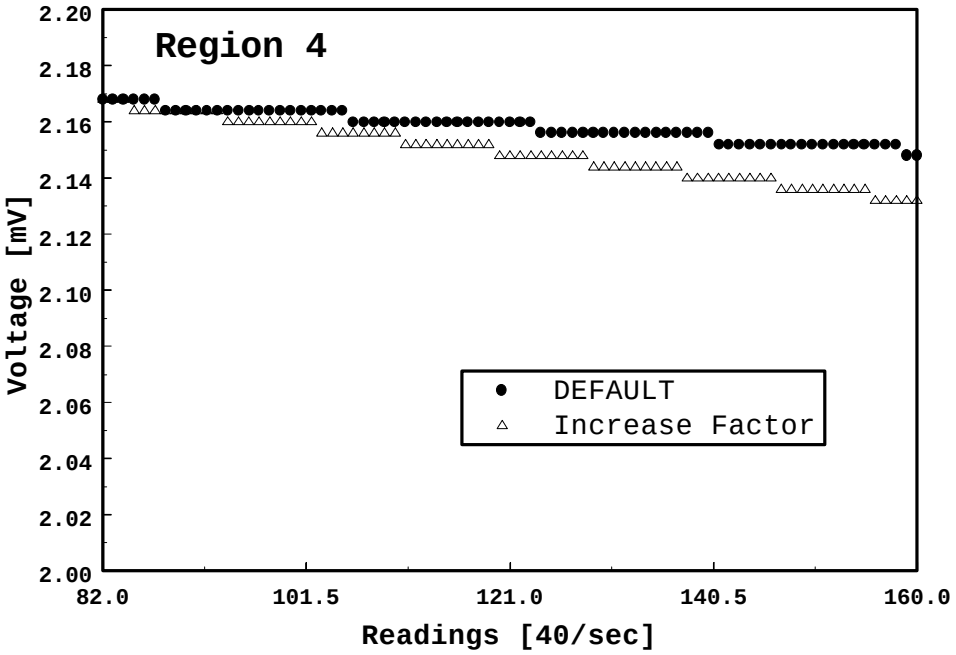

Figure 4-8 c and d (continued)

e)

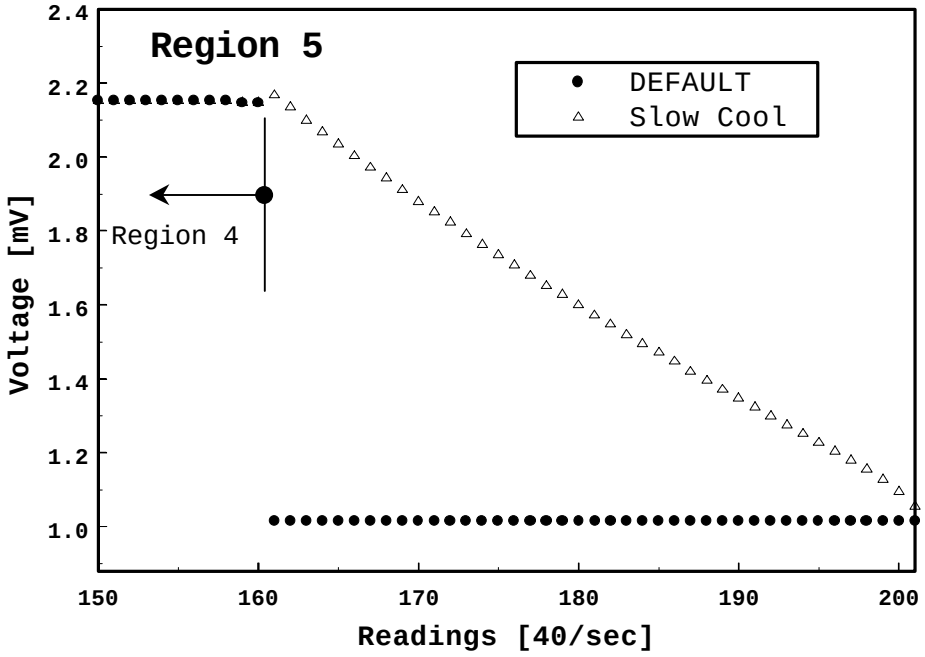

f)

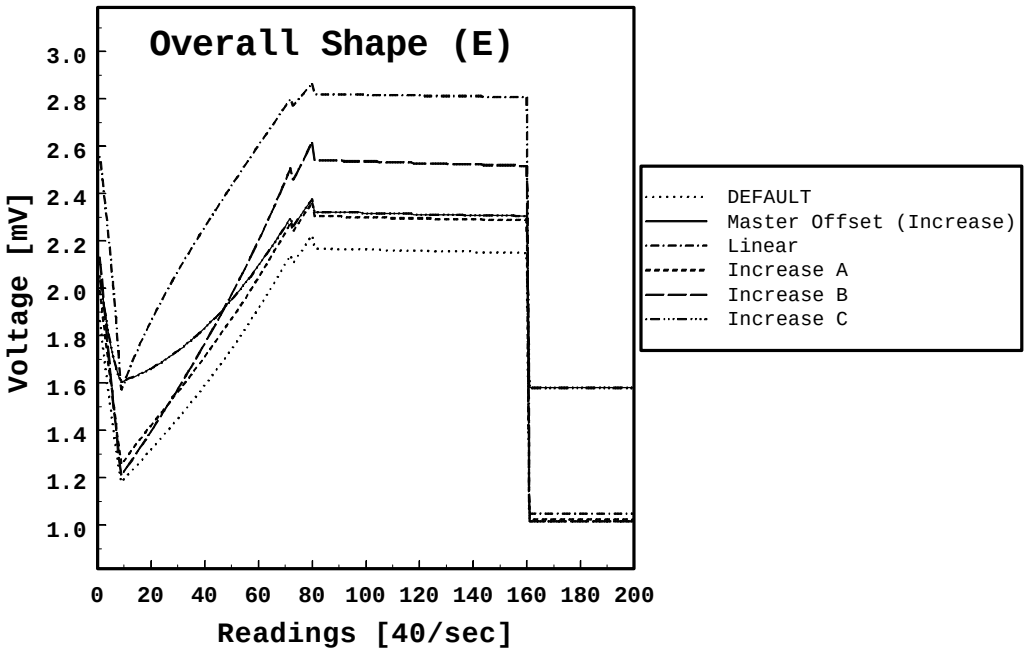

Figure 4-8 a-f Modifiable regions of driver file by using different modules on the front panel of GHDG.

Graphite Heater Recorder (GHR) is an application program of a driver file, which is generated by GHDG, previously. A block diagram of GHR is shown in Figure 4-9.

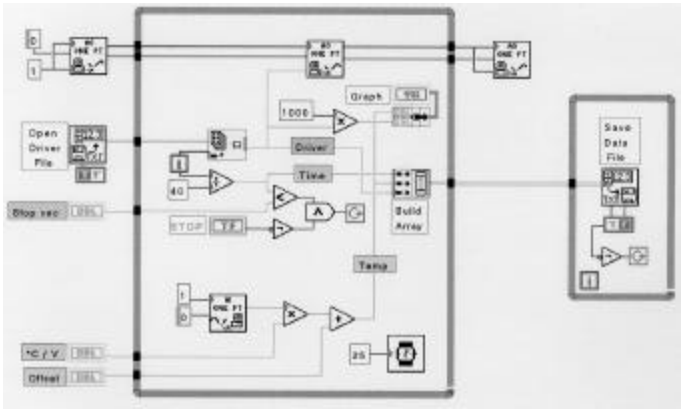

Figure 4-9 A block diagram of the Graphite Heater Recorder (GHR).

In GHR, a driver file is selected, is read, and then is applied to the heat treatment device. A front panel of GHR is shown in Figure 4-10. At the same time, GHR reads signal from the pyrometer and saves it in a computer.

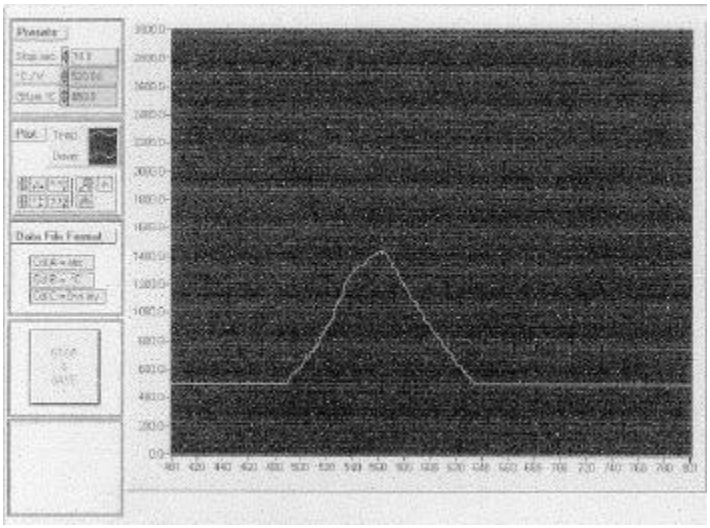

Figure 4-10 Front panel of graphite heater recorder (GHR).

Char samples in this study were heat treated at ~ 10^3 K/sec to a target temperature and held isothermally for a given holding time before uncontrolled cooling. A typical

driver file and temperature profile is shown in Figure 4-11 a. The target temperature and the holding time of the driver file were 1750 °C and 3 seconds, respectively. Depending on the sample characteristics and a slight variation of the graphite sheets' geometry, the resultant temperature profile might be different for each sample, even if the same driver file is used. Figure 4-11 b showed how to measure the holding time and the heat treatment temperature on the measured temperature profile.

a)

b)

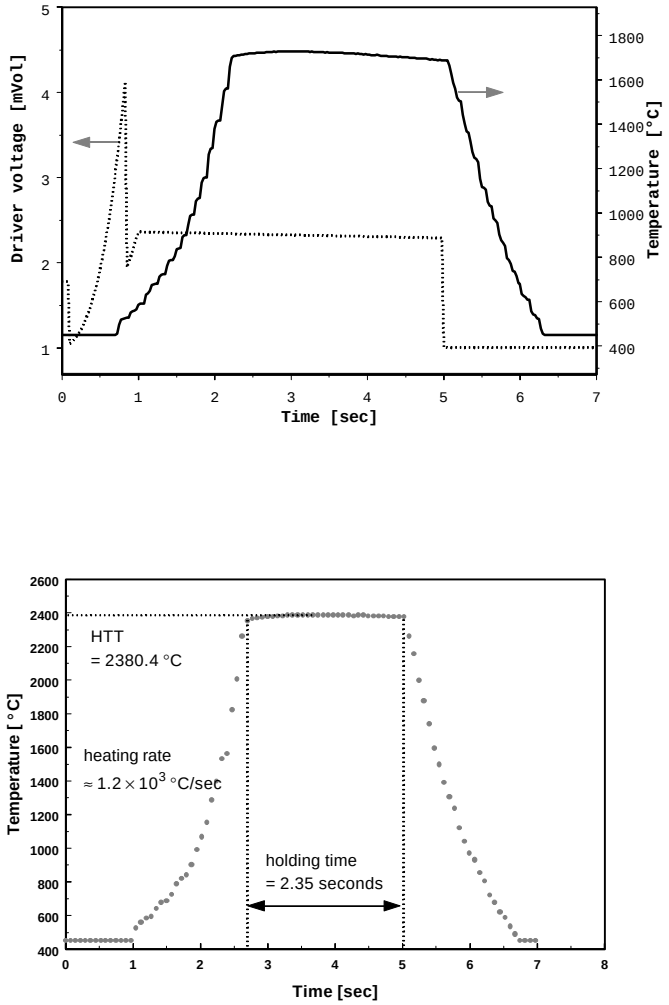

Figure 4-11 a) Typical driver file (broken line) and temperature profile (solid line) and b) hold time and HTT measurements.

5 THERMAL ANNEALING OF CHARS FROM DIVERSE ORGANIC PRECURSORS UNDER COMBUSTION-LIKE CONDITIONS

5.1 Char Samples

Three bituminous coals (Rosebud, Illinois #6, Pocahontas #3), one anthracite (Lykens valley #2), and one lignite (Beulah lignite) were obtained from the Penn State Coal Sample Bank (PA, USA) for this study. Char samples were prepared by pyrolysis at 700 °C for 1hr in He. The pyrolysis was carried out in a 25 mm diameter horizontal quartz tube furnace with a coal sample placed in a ceramic boat. Pyrolyzed sample particles were ground and size-graded to 75 ~ 106 μm in diameter for further heat treatment. The char samples prepared in the above manner are a base line material of our study and will be referred to as “raw char”.

The properties of the investigated samples are summarized in Table 5-1. Ultimate and proximate analyses were performed at Huffman Laboratories (CO, USA) except coal samples that were analyzed at the Penn State Coal Sample Bank. N_2 surface area was measured using an AUTOSORB-1 (Quantachrome) for the raw chars.

Table 5-1. Properties of the Samples

Sample		Ultimate Analysis, wt-% daf					ash	Volatile Matter	Fixed Carbon	N_2 Surface Area
		C	H	O[a]	N	S	% dry	% daf	% daf	[m^2/g]
Beulah Lignite (ligA) PSOC-1548	coal*	73.2	4.4	20.6	1.0	0.82	9.6	62.0	38.0	
	char§	83.0	1.8	12.9	1.3	1.1	13.5			7.14
Rosebud (subB) PSOC-1547	coal	78.3	4.2	15.2	1.1	1.4	12.6	47.7	52.3	
	char	84.8	1.9	11.1	1.3	1.0	15.4			36.39
Illinois #6 (hvCb) PSOC-1539	coal	78.2	5.5	9.8	1.3	5.4	16.2	45.5	54.5	
	char	87.2	1.8	5.8	1.4	3.8	21.9			38.44
Pocahontas #3 (lvb) PSOC-1556	coal	89.8	5.0	3.4	1.2	0.78	4.6	19.2	80.8	
	char	93.3	1.5	3.1	1.3	0.83	5.6			2.61
Lykens Valley #2 (an) PSOC-1558	coal	90.4	4.1	4.3	0.80	0.56	11.2	5.1	94.9	
	char	91.2	1.9	5.7	0.74	0.56	10.3			3.64

* Coal analyses from the Penn State Coal Sample Database (version 8.1, PA, USA).
§ Char samples were prepared by pyrolysis at 700 ºC for 1 hour in He, and then ground and sieved into 75 ~ 106 μm diameter. Other proximate and ultimate analyses were performed at Huffman Laboratories (CO, USA).
a Determined by difference.

5.2 Heat Treatments

Heat treatment was performed using the transient heat treatment device. About 6 ~ 10 mg of char sample was placed between the two graphite sheets. The electrode chamber was evacuated to 0.5 torr and purged with He gas. The pre-programmed driver file was fed to the heater and the temperature of the lower graphite sheet's surface was measured using a high-speed pyrometer. Each sample was heat treated with several different temperatures ranging from 1000 to 2600 °C and different hold times of 2.6, 4 seconds and 2 minutes. The heat treated char samples using the transient heat treatment device will be referred to as "HTD" samples.

5.3 Nonisothermal Thermogravimetric Analysis.

Oxidation reactivities of heat treated char samples were measured by non-isothermal thermogravimetric analysis using a standard thermogravimetric analyzer (Cahn TG-2141). The entire microbalance and sample suspension system is contained in a vacuum-tight enclosure. A sample bucket (pan style, Pt) is mounted to hang-down platinum wire from a microbalance. A furnace, which is controlled by a temperature programmer, is placed around a quartz/ceramic tube and a sample pan. Temperature is monitored by a thermocouple located right below the sample pan. Various fly ash samples from a power plant and graphite powder (size < 74 μm in diameter, Alfar Aesar™, MA) were included for comparison purposes. About 5 ~ 7 mg of char or HTD char sample were placed in the TGA pan and heated at 7 °C/min to 950 °C and held at 950 °C for 10 min at atmospheric pressure. The oxidation reaction was conducted in flowing dry-air at 34 ml/min flow rate. Sample weight and temperature were continuously monitored and recorded. Char reactivity was expressed as $log(k_o)$ at 20 % conversion, where k_o [sec^{-1}], which has been calculated using 35 kcal/mol as an activation energy for char oxidation, is the pre-exponential factor in the Arrhenius equation:

(5-1)

$$-(1/m)(dm/dt) = k_o exp(-E/RT)$$

where m is the sample weight on dry ash free bases and E is the activation energy.

It was experimentally verified that the amount of sample had no effect on observed kinetics, demonstrating that diffusion in the bed was not limiting. A sample weight in the range of 5 ~ 7 mg used in the current reactivity study should be in the regime where there is no mass diffusion limitation. One technique to reduce a chance to be in that regime is to spread the sample particles to reduce the sample depth in a bucket. For this purpose, a pan style with shallow depth is preferable. Samples of various weights from 4 to 15 mg were mounted on the pan style platinum bucket and the reactivities were measured using non-isothermal thermogravimetric analysis. One measure of mass diffusion limitation is to compare the normalized weight loss rates (equation (5-2)) at maximum as a function of initial sample weight.

(5-2)

$$\textit{Normalized weight loss rate } [sec^{-1}] = -\frac{1}{m_i}\left(\frac{dm}{dt}\right)$$

where m is the sample weight in mg, t is time in seconds, and m_i is an initial sample weight in mg (daf).

Figure 5-1 shows the normalized weight loss rate at maximum as a function of initial sample weight (daf). Average rate is 0.001072 [sec^{-1}] with small variation ± 0.000022. There is no observable deviation in the rates as a function of sample weight studied here, 4 ~ 15 mg. Figure 5-2 shows $log_{10}\ k_o$, which is a measure of reactivity, at two different carbon conversion levels. Observed reactivities at 20 and 50 % carbon conversion (daf) are 6.78 ± 0.05 and 6.60 ± 0.03 [log (sec^{-1})], respectively. This, again, shows small variation in 4 to 15 mg sample weight. It was concluded, therefore, that mass and heat transfer limitations do not significantly influence the reactivities reported in this work.

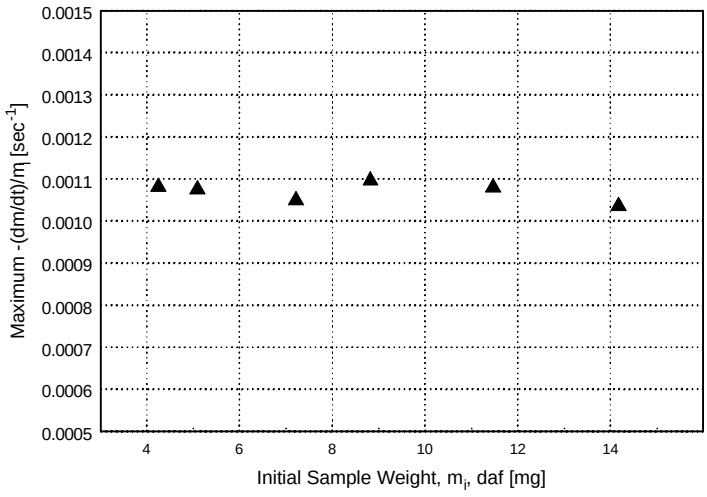

Figure 5-1 Maximum normalized weight loss rate $(-dm/dt)/m_i$ and as a function of initial sample weight (daf). Observed maximum rate is 0.001072 ± 0.000022 [sec^{-1}].

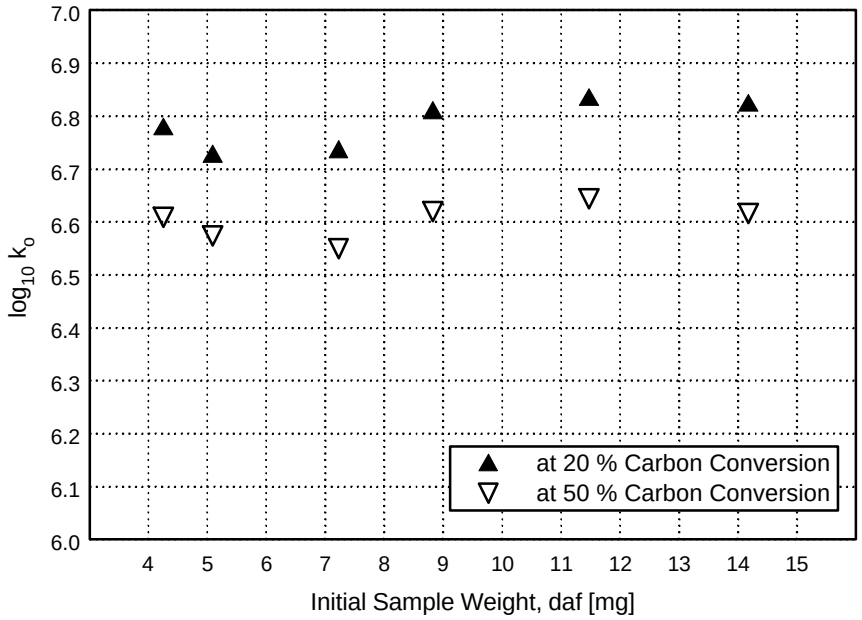

Figure 5-2 ***Log₁₀ k_o*** **at two different carbon conversion levels, 20 and 50 % as a function of initial sample weight (daf). Observed reactivities at 20 % and 50 % are 6.78 ± 0.05 and 6.60 ± 0.03 [Log (sec^{-1})].**

5.4 High-Resolution Transmission Electron Microscopy

HRTEM was performed on the raw char and HTD char samples of Lykens valley #2 and Pocahontas #3. The raw char sample was ground, dispersed in methyl alcohol ultrasonically, placed on a holey carbon film coated copper grid (3 mm in diameter, Ted Pella Inc., Redding, CA, USA), and examined in a JEOL JEM-2010 microscope operating at 200 kV. The HTD char sample was prepared by fluidizing the dry char in a stream of helium gas and immersing the TEM specimen grid into the fluidized powder. This technique avoids the use of a dispersing solvent and is useful when the available sample amount is small. Samples were first examined at moderate magnification to find wedge-shaped fragments that are optically thin at the edge. A number of such edge regions are then photographed at high magnifications in lattice fringe (LF) imaging mode, and representative fields of view selected and reproduced for discussion. Selected images were digitally processed and presented with structure parameters. The details of

the image analysis algorithm can be found elsewhere (see section 6.1). Briefly, the algorithm is made of several steps, including digitization of micrographs, noise reduction by Fourier transform, skeletonization, post-processing, and identification/determination of fringe size and shape statistics.

5.5 Results and Discussion

5.5.1 Example Normalized Rate of Weight Loss Profile

Figure 5-3 shows normalized rate of weight loss profile from selected char samples, which is the plot of the instantaneous sample weight divided by initial sample weight on ash-free basis versus sample temperature. In this profile, the position of the peak is a measure of reactivity, with higher temperature peaks indicating lower reactivities. The samples in this plot are raw chars and HTD chars with 2.6 ± 0.4* second hold time at a peak temperature. As transitions of peak positions as a function of heat treatment temperature (HTT) indicate, a general phenomenon of thermal deactivation can clearly be seen. The oxidation reactivity decreases as HTT increases even at the short hold time of 2.6 seconds. The Pocahontas #3 shows low reactivity for raw chars and relatively low degree of deactivation as HTT increases. For Illinois #6, there is not much difference between the raw and 1020 °C HTD char samples, but there is a relatively high degree of deactivation at high HTT of 2440 °C. Lykens valley #2 shows the lowest reactivity for a raw char and a relatively high decrease when heat treated at 2400 °C. The other chars including PRC showed the similar trends: the higher the HTT is, the lower the reactivity. This reactivity reduction toward reactives by thermal treatment is generally referred to as thermal annealing. Increase in the heat treatment temperature induces changes in the inherent reactivity of the carbon (i.e. active site concentration), changes in the physical structure that affects reactant access to the carbon, and changes in the amount, nature, and distribution of catalytic materials within the carbon [6,23].

* Note that a hold time is slightly different from run to run. An average hold time and a standard deviation of runs are shown here.

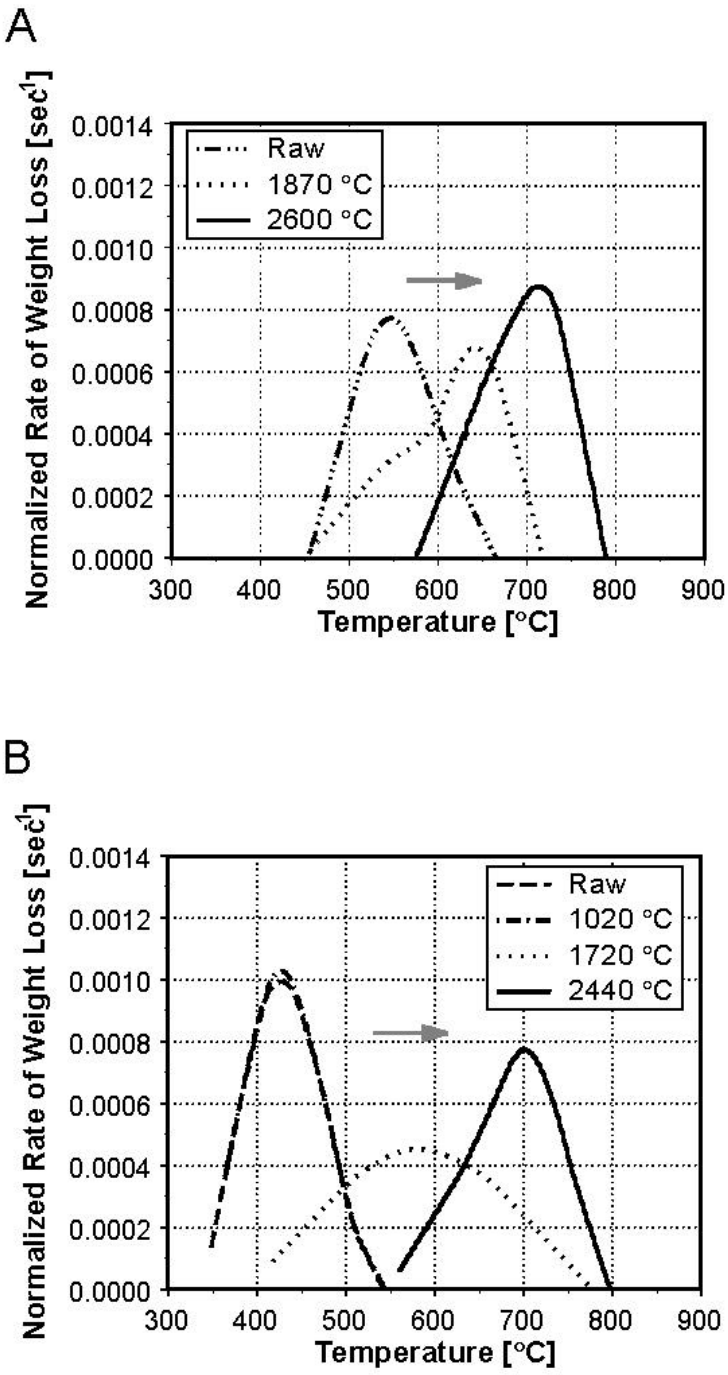

Figure 5-3 (CONTINUED)

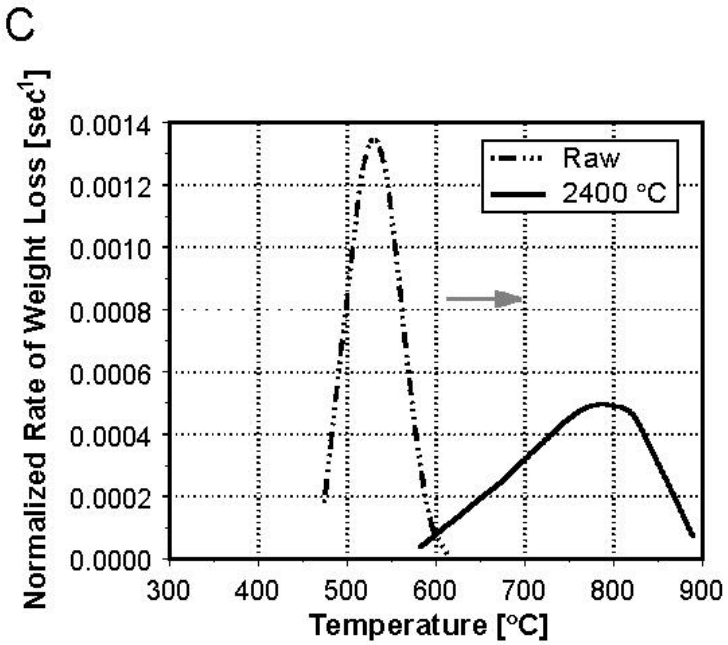

Figure 5-3 Normalized rate of weight loss profiles for Pocahontas #3 (A), Illinois #6 (B), and Lykens valley #2 (C) char samples. Heat treatment temperatures (HTT) are shown in the legend box. The raw char sample was prepared by pyrolysis at 700 °C for 1 hr in flowing He in tube furnace. Heat treated char was prepared in the transient heat treatment device with 2.6 ± 0.4 second hold time at a peak temperature.

5.5.2 Effect of Hold Time at a Peak Temperature

Figure 5-4 shows the effect of hold time as a function of heat treatment temperature (HTT). Note that a direct comparison at one temperature is not possible, since the peak temperature varies slightly from run to run. Figure 5-4-A shows that the reactivity loss trends between 2.5 ± 0.2 and 4.8 ± 0.4 second hold times are similar to each other for Beulah lignite throughout the HTT's. HTD chars with the 4.8 second hold time show slightly lower reactivity without a significant difference from the 2.5 second sample. 118 second char at 1650 ºC has a lower reactivity by a factor of 10 than the shorter hold time char at about 1650 ºC and a similar reactivity to those heat treated at the higher HTT of 1900 ºC. Relatively small increase in heat treatment temperature has more effect in determining a reactivity than a large increase in hold time. In case of high rank

Pocahontas chars, almost same reactivities between 2.5 ± 0.2 and 4.7 ± 0.3 second hold time can be found (see Figure 5-4-B). The effect of the longer hold time is relatively small compared to the case of Beulah lignite, but 116 seconds at 1560 ºC deactivates reactivity by a factor of 2 from those with the shorter hold time. The rest of char samples studied here showed similar features that the difference in the effect of two different hold times of 2 and 4 seconds on reactivity is negligible. Heat treatment temperature and time duration at a peak temperature are generally important parameters in thermal annealing. For our baseline samples, a peak temperature seems to be more dominant factor in determining reactivity than time duration at a peak temperature.[+] We could see a significantly different reactivity only for those heat treated chars with over 100 second difference in hold time. Major thermal annealing might already have taken place at very short times or during the sample preparation step. Subsequent thermal annealing occurs gradually.

[+] From the Figure 5-4-A, reactivity at (1700 ºC, 2.5 seconds) is about 8.1. If hold time increases by 60 times to 118 seconds at a given temperature, the reactivity decreases by a factor of 0.9 to 7.1. The reactivity of 7.1, however, can be reached by increasing the temperature by only 1.1 times from 1700 to 1900 ºC. Small increase (1.1 times in this case) in temperature can match a big increase (60 times) in time duration at a peak temperature in determining reactivity.

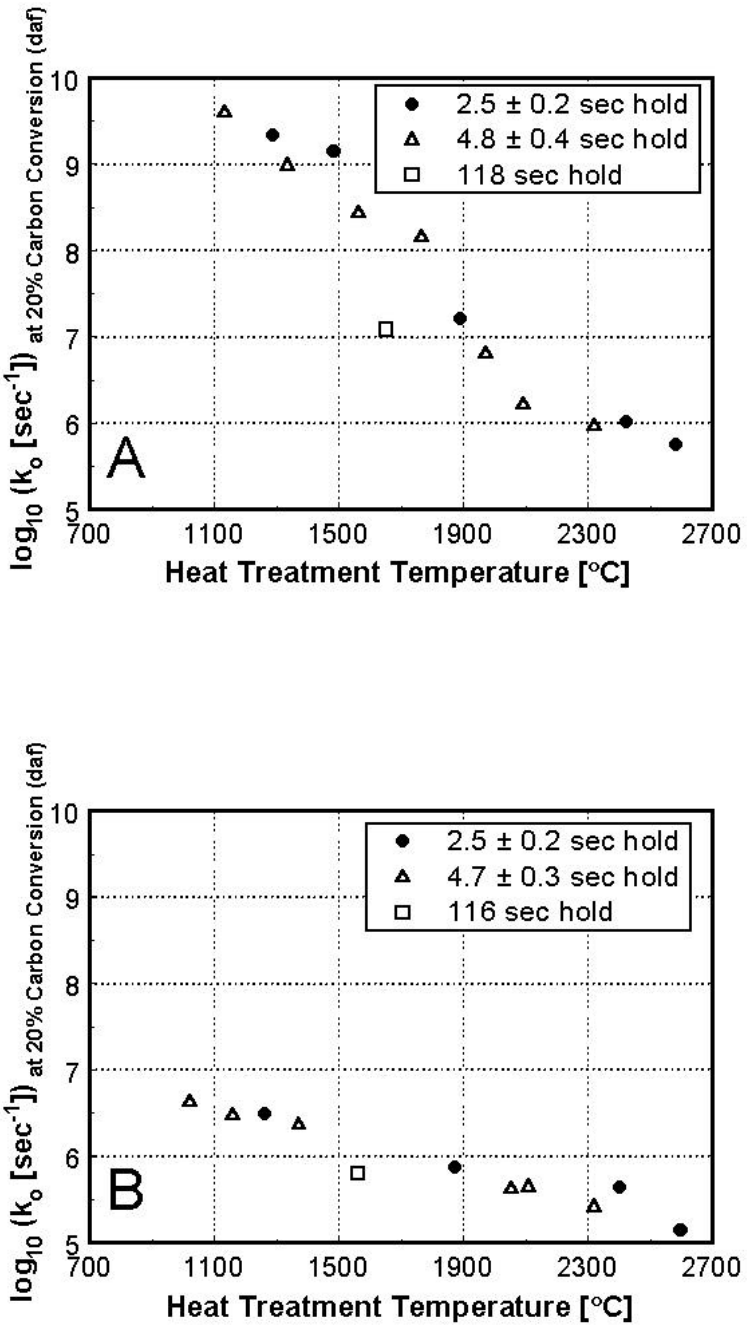

Figure 5-4 Effect of hold time for Beulah lignite (A) and Pocahontas #3 (B): $\text{Log}_{10}\ k_o$ at 20 % carbon conversion (daf) as a function of heat treatment temperature (HTT). Samples were heat treated up to a HTT at 1×10^3 deg/sec and held for a given time at the HTT.

5.5.3 Comparative Reactivity Loss for Various Precursors

Figure 5-5 shows reactivities at 20 % carbon conversion (daf) as a function of peak heat treatment temperature. There are several observations in this plot. First, there is a wide variation of the reactivities at a given temperature. At 700 ºC, the most reactive and the least reactive chars differ in reactivity by 3 1/2 order of magnitude. Secondly, a large effect of peak temperature is observed, e.g. lignite shows loss of 4 1/2 order of magnitude between 700 ºC and 2500 ºC. A general rank dependency is observed with the lower rank samples having the higher reactivity, in agreement with many other studies [24,25,26,27].

With only a few exceptions, samples with high reactivity tend to show high degree of deactivation leading to a convergence in reactivity loss trends among various precursors (see Figure 5-5).

Beulah lignite char with the highest reactivity among the samples shows the highest degree of deactivation by the 4 1/2 order of magnitude between 700 and 2500 ºC. The high reactivity of lignites has been related to the existence of highly dispersed inorganic catalysts in the char [6]. A primary catalyst has been identified as CaO whose sintering, vaporization and incorporation into glassy phases is a primary annealing mechanism. A high volatile bituminous, Illinois #6 coal char shows much higher reactivity than a high rank Pocahontas #3 char at low heat treatment temperature, but the materials show similar reactivities above about 2000 °C. Structural differences might be a major factor. Illinois #6 char has a less ordered structure and a potential for structural ordering upon heating, which involves the loss of aliphatic chains leading to a realignment of the aromatic clusters in the char [28]. On the other hand, Pocahontas has an ordered structure that developed in the raw char preparation (see Figure 5-7-D, discussed later) and thus has a lower potential for annealing. Phenol formaldehyde resin char, with a disordered rigid carbon network, shows little deactivation until 1630 °C. The loss of reactivity becomes apparent at higher temperature (> 2200 °C) and the reactivity becomes similar to that of Pocahontas. The anthracite char shows a relatively high degree of deactivation and the reactivity becomes similar to that of graphite powder at 2400 °C. An interesting observation is that the degree of deactivation for anthracitic char

is larger than that of Pocahontas (lvb) (see section on HRTEM fringe image). Reactivities were also measured for various carbon-content fly ash samples from full-scale pulverized coal fired boilers and are included in Figure 5-5. They originate from high volatile bituminous stem coals heated to peak temperatures of 1600 - 2000ºC in flames. They show a relatively narrow range of reactivities, from 5.9 to 6.6 in $\log_{10} k_o$.

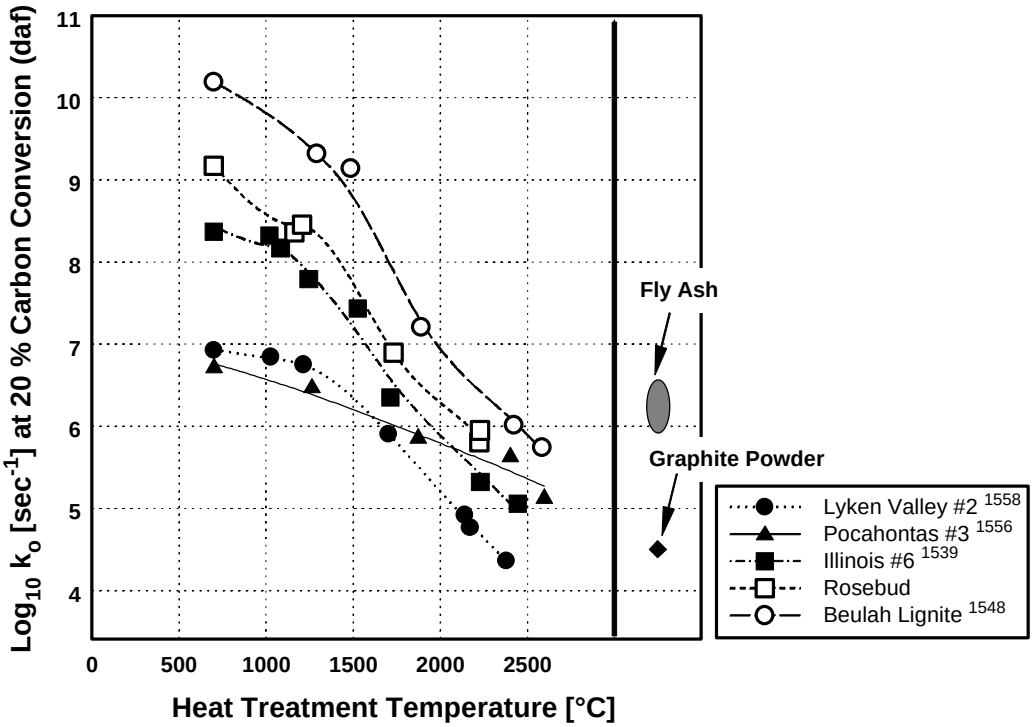

Figure 5-5 $\log_{10} k_o$ at 20 % carbon conversion (daf) as a function of heat treatment temperature (HTT, °C). The reactivities of raw chars are plotted at 700 °C. The reactivities of fly ash samples (LOI = 20 ~ 40 %) and synthetic graphite are included. LOI stands for loss on ignition (weight loss percentage during air oxidation at 1270 K).

5.5.4 Structural Evolution vs. Reactivity Loss

Of particular interest is the very different annealing behavior of the two highest rank coal chars, Pocahontas and Lykens valley (see Figure 5-7). HRTEM was performed on the raw chars and heated chars from both samples and representative regions were

reproduced in Figure 5-7. A high degree of orientational order can be found in Pocahontas #3 raw char and heated chars (Figure 5-7-D, E, F). A small increase in orientation can be found in Lykens Valley #2 from 700 ºC to 1700 ºC (Figure 5-7-A, B), but graphite-like structure can be found in 2400 ºC sample (Figure 5-7-C).

Overall, the anthracite shows much greater degree of structural change during heat treatment and this is a likely contribution to its much higher annealing propensity.

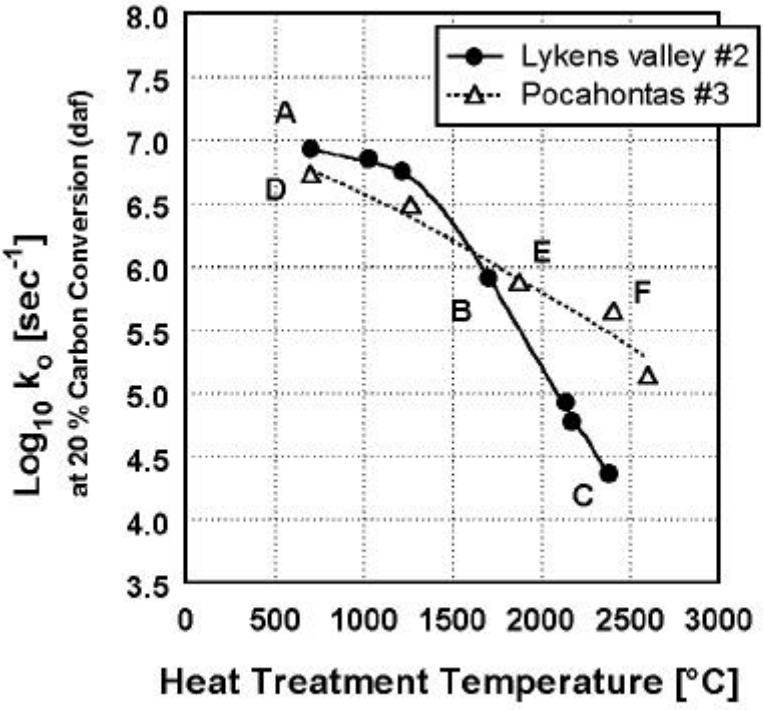

Figure 5-6 Reactivity as a function of heat treatment temperature: Pocahontas #3 and Lykens Valley #2.

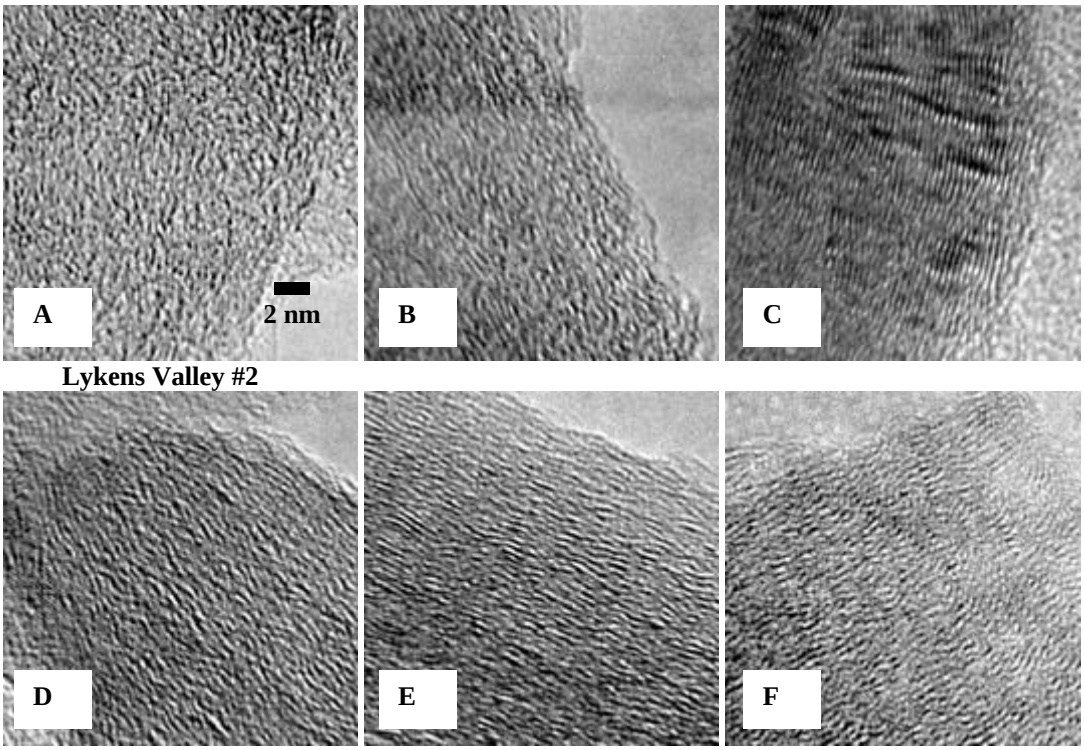

Figure 5-7 HRTEM images from the heat treated samples: Lykens Valley #2; A-, B-, C-, and Pocahontas #3; D-, E-, F- corresponding reactivities are shown in Figure 5-6.

Structure ordering can be clearly compared in Figure 5-8, which shows processed HRTEM images from selected Lykens Valley #2 and Pocahontas #3 char samples using the method described in previous report. Structure parameters, including nematic order parameter, S_{m2N} in entire field, mean fringe length, and tortuosity, are shown under each processed image. From raw char to HTD (1700 ºC and 2380 ºC) chars, anthracite shows large increase in nematic order parameter, S_{m2N} and mean fringe length (Figure 5-8 A, B, and C). High value of S_{m2N} (> 0.8) in HTD anthracite chars, which satisfy mesophasic long range order criterion (see previous report), implies that the anthracite went through liquid transition state. 2380 ºC HTD char shows a large decrease in tortuosity and highly stacked graphene layers with shorter interlayer spacing as shown in Figure 5-8 C. The mean fringe length of HTD anthracite char becomes larger than that of HTD Pocahontas at 1700 ºC or higher HTT. Pocahontas char samples show high S_{m2N} (> 0.9) and low

tortuosity (~ 1.1) in both raw char and 1870 ºC HTD chars (Figure 5-8 D and E). The high S_{m2N} indicates that Pocahontas also went through a liquid transition state, but at much lower temperature (< 700 ºC).

In summary, Lykens Valley, potentially has a high graphitizablity. At 2.5 second HTT (> 1700 ºC), the nanostructure in Lykens Valley becomes more aligned than Pocahontas does and as a result, the reactivity of anthracite decreases more. Pocahontas shows high structural order at low HTT and a less degree of structural evolution at higher HTT. The reason for high early order in Pocahontas is high mobility and the occurrence of a liquid crystal transition.

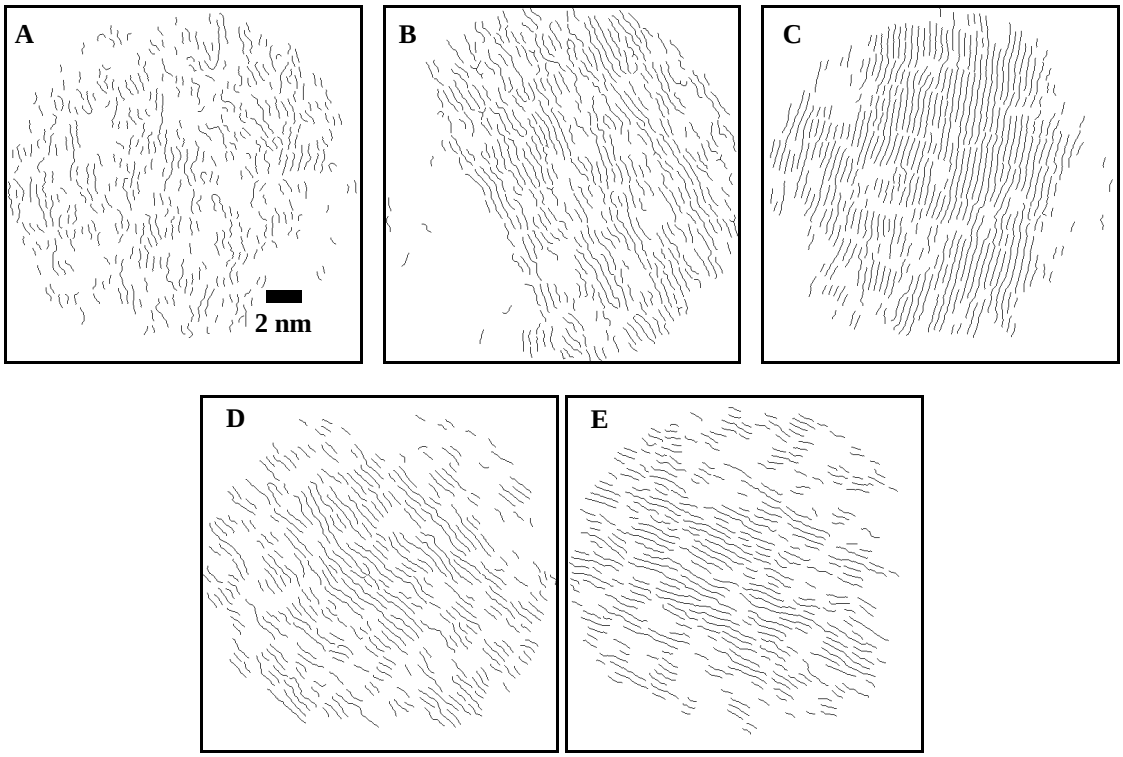

Sample	S_{m2N}	Mean Fringe Length [Å]	Tortuosity
A	0.77	22.1	1.17
B	0.90	31.0	1.17
C	0.97	39.8	1.09
D	0.94	29.6	1.10
E	0.96	29.9	1.11

Figure 5-8 Processed images from selected HRTEM images: Lykens Valley #2, (A) raw char, (B) 1700 ºC HTD char, and (C) 2380 ºC HTD char. Pocahontas #3, (D) raw char and (E) 1870 ºC HTD char.

6 A METHODOLOGY FOR ANALYSIS OF 002 LATTICE FRINGE IMAGES AND ITS APPLICATION TO COMBUSTION-DERIVED CARBONS

6.1 Image Analysis Algorithm

A major challenge for the quantitative treatment of TEM fringe images is the conversion of the complex photographic print into a set of distinct, identifiable fringes that can be analyzed by traditional object-oriented image analysis algorithms. The section below outlines a new preprocessing procedure, which, while not unique or free from subjectivity, is a useful general procedure that yields reproducible fringe populations that reveal the essential differences between samples. A six step algorithm is being used to analyze the set of HRTEM fringe images: (1) digitization of the fringe image, (2) noise reduction through numerical filtering procedures including Fourier transform, (3) identification of a fringe population based on threshold brightness criteria and skeletonization (4) post-processing through identification and separation of the aggregate structures, or identification and reconnection of the disconnected segment structures, (5) determination of fringe size and shape statistics, and (6) interpretation of the statistical results in terms of the structure parameters.

6.1.1 Digitization

Representative regions of fringe image were digitized using a commercial 600 dpi (dot per inch) scanner and stored as 512 × 512 (in pixels), 8-bit grayscale images (see Figure 6-1). True image size can be adjusted by increasing or decreasing resolution of the scanner under the same pixel dimension. We have found during this work that the resolution with 120 dpi or higher resulted in proper description of fringes in the photographic prints. The higher the resolution is, the bigger the image size and the longer the image processing time. Various resolution limits were used to analyze the set of fringe images. The applied resolution limits and true dimensions are listed in Table 6-1.

Original images were enhanced by adjusting brightness and contrast while digitizing. Brightness and contrast settings can affect the final result of image processing. To have a consistency in the processing, a representative image region is

digitized by expanding a tonal range within the selection area from dark gray and light gray to black and white, respectively. An example raw, scanned image is reproduced in Figure 6-1.

Table 6-1 Dimensional calibrations and Resolution limits in Digitization

Magnification in the photographic print **[X 10^6] [a]**	***Resolution limit*** **[DPI][b]**	***True metric dimension of digitized image for 512 pixels*** **[nm]**	***Conversion Factor*** **[nm/pixel]**
~ 2	300	21.7	0.0424
~ 2	120	54.2	0.1059
~ 6	120	22.6	0.0441
~ 3.8	150	39.6	0.0387

a: Nominal magnification from microscope has ±0.05% error
b: DPI stands for dots per inch representing resolution

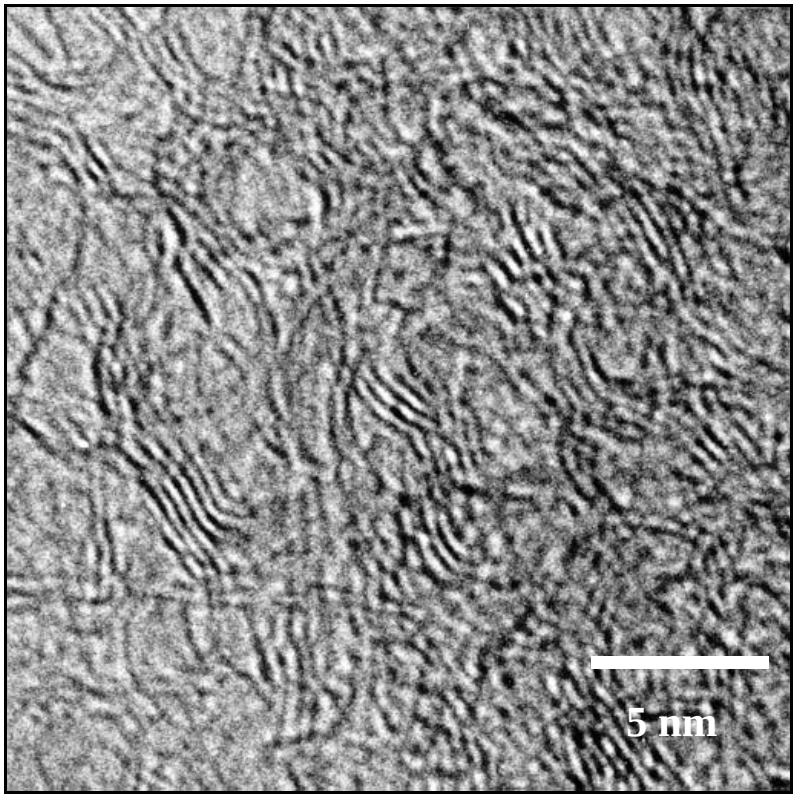

Figure 6-1 Raw, scanned fringe image of partially combusted coal char.

6.1.2 Noise Reduction

Reduction of image noise has been accomplished by Fourier Transform (FT) filtering. For a Fourier transformation, the digitized raw image was filtered through a circular window with a diameter of 256 pixels. While eliminating noise, the FT of the HRTEM image can be used to establish periodicities, and is also used to extract significant structural data from the image. The digitized image is subjected to an FT and the transformed image is filtered through a frequency window centered on the typical spatial frequency for turbostratic carbon (1/3.0~1/4.5 $Å^{-1}$) [1]. After reverse transformation, the crystalline image features are accentuated and perfected, while features in the image having different spatial frequencies (including noise) are weakened. To reduce boundary effects from the frequency window, a gaussian profile extending outwards (and inwards) is implemented on the window. An example FT filtered image is shown in Figure 6-2.

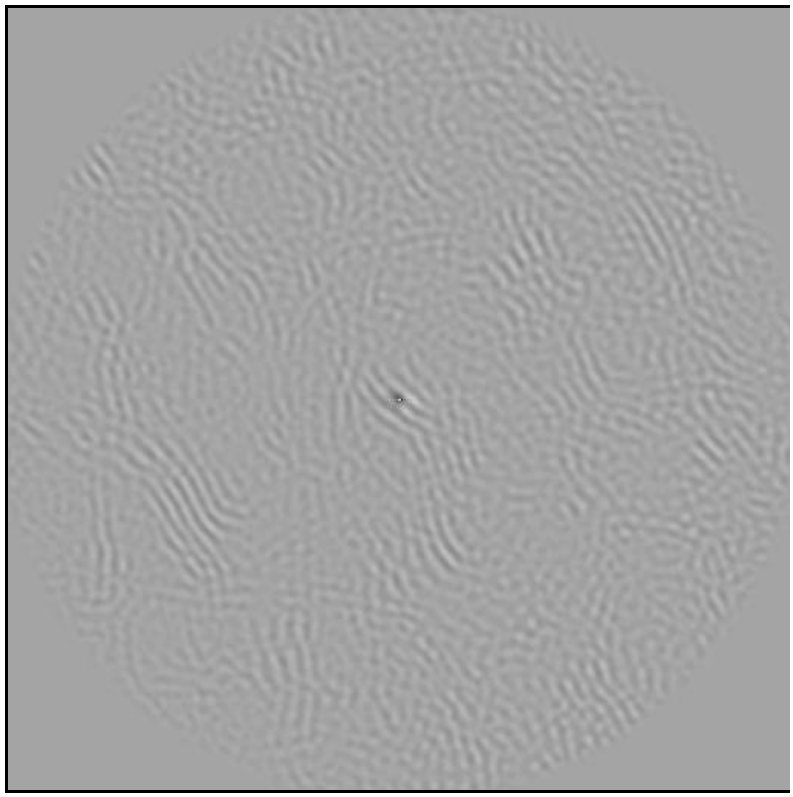

Figure 6-2 FT filtered image of Figure 6-1.

[1] Theoretically the center peak (corresponding to infinite distance on the original image) in the Fourier space is always needed for the reverse Fourier Transformation, therefore an annulus would be insufficient. SEMPER retains the information content of the center peak, and even if the center is manually masked out, the reverse transform can be performed.

6.1.3 Fringe Identification

This step is the most critical to the meaningful analysis of fringe images. The filtered image is transformed to a two "phases" by setting a threshold brightness value for the phase boundary, separating the two phases (here separated as black and white). Single phase regions that are completely surrounded by the opposite phase (and hence isolated from other regions of the same phase) are identified as objects, or particles. These particles can be most clearly seen by converting the image to binary format, in which the dark phase is assigned a brightness of zero and the lighter phase a brightness of 1.

In fringe images one generally seeks to identify the dark fringes in a continuous sea or background of higher brightness corresponding to regions of high electron transmission. Generally, as the threshold brightness is increased above zero, the total number of pixels assigned to the dark phase increases and the number of (dark) fringes increases as well. After a point, further increases in threshold brightness cause fringes to merge and overlap, as the total amount of dark phase increases. Obviously, as the threshold is increased toward 255 (the maximum brightness in an 8-bit image) the area fraction of the dark phase approaches one and there is only one, very large "fringe". This thought experiment clearly illustrates that the number of fringes must pass through a maximum as threshold brightness is varied. Figure 6-3 supports this thought experiment. In recent work at MIT [22,29], fringes have been identified by setting the brightness threshold at the value giving the maximum number of identified fringes.

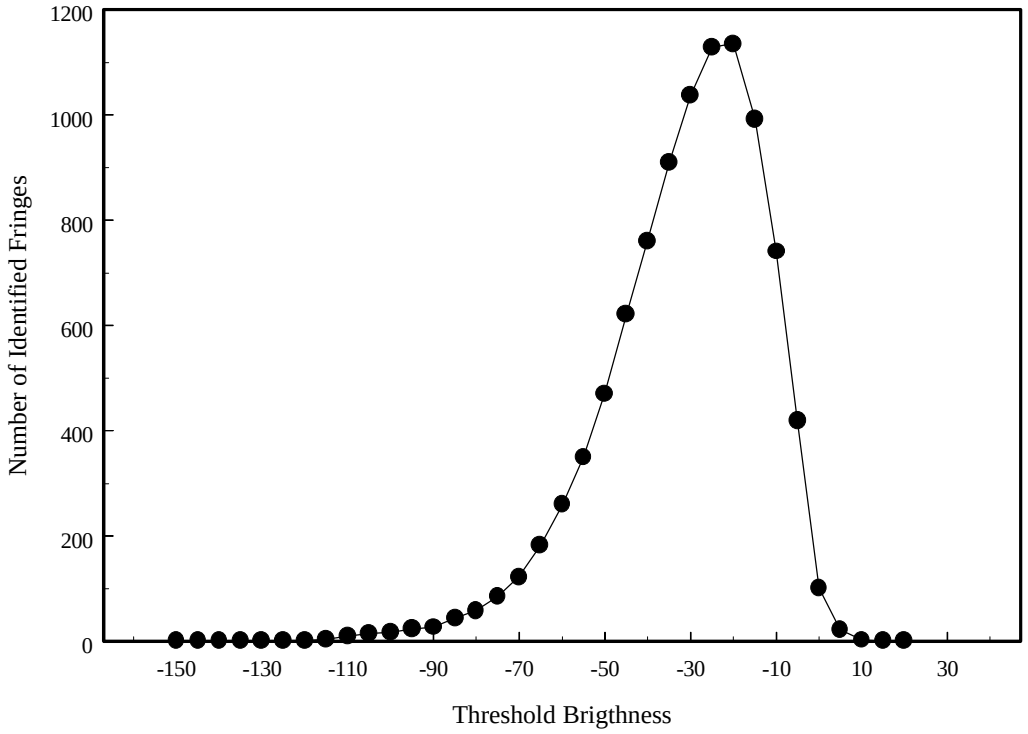

Figure 6-3 Effect of the threshold brightness on the number of identified fringes (from Figure 6-2).

We have found that there is no single value of the threshold that results in proper identification of all fringes. At any threshold value, close examination of the image reveals fringes that have merged with neighbors to produce aggregate geometries, examples of which are structures resembling the letter "*Y*", or the letter "*H*". For this local region of the image, the threshold has been set too high and merging of distinct neighboring fringes has occurred. In the same image, however, one finds series of short linear segments lying along a common axis but separated by small distances. This structure is symptomatic of a threshold brightness that is set too low - a phenomenon that can be explained as follows. There are always small variations in brightness (gray scale) within a single fringe in the raw image. As the threshold value is increased, the darkest portions of the fringe are first to appear, and take the form of disconnected islands. As threshold value increases, the islands grow and merge to form the original fringe. If the

threshold value is too low, the individual elongated islands are identified as fringes, but will appear with the characteristic structure of linear segments lying along a common axis. Our major thrust is to solve this problem and avoid the very real danger of overestimating or underestimating fringe lengths. Our approach is to keep the single threshold value for preliminary identification, but to supplement it with post-processing algorithms that identify and separate the aggregate structures, or identify and reconnect the disconnected segment structures. Extracted binary fringe image of Figure 6-2 using the threshold value at the maximum number of fringes is shown in Figure 6-4.

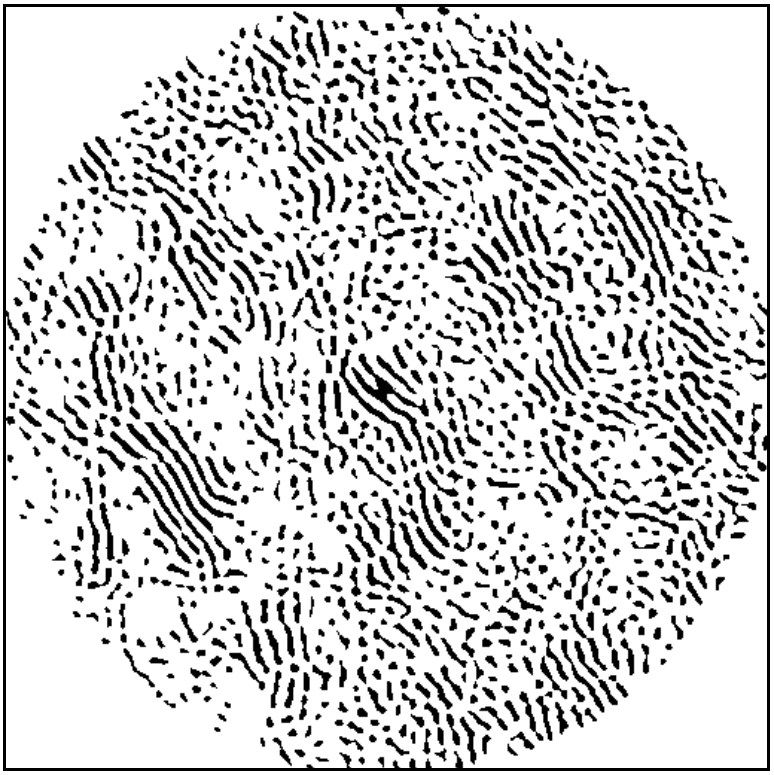

Figure 6-4 Binary, filtered fringe image of partially combusted coal char.

6.1.4 Skeletonization and Post-Processing

An identified fringe in the binary image is thinned (skeletonized) to one-pixel in width — a "skeleton" of the original fringe — while the 8-connectivity is maintained (see Figure 6-5. Two types of pixel connectivity are commonly distinguished, 4-connectivity, in which pixels are defined to be connected to their horizontal and vertical neighbors but

not to their diagonal neighbors, and 8-connectivity, in which diagonal neighbors are also included. The thinning transformation applies a 3 by 3 neighborhood mapping table to each pixel, which selects and erodes neighboring pixels while maintaining a continuous structure around the chosen pixel. After multiple passes, the final result is an 8-connectivity skeleton of the original fringe. The skeleton is a powerful shape factor for feature recognition, containing both topological and metric information. The topological values include the number of end points and the number of nodes where branches meet. The metric values are the mean length of branches and the angles of the branches. An example skeletonized image is reproduced in Figure 6-6.

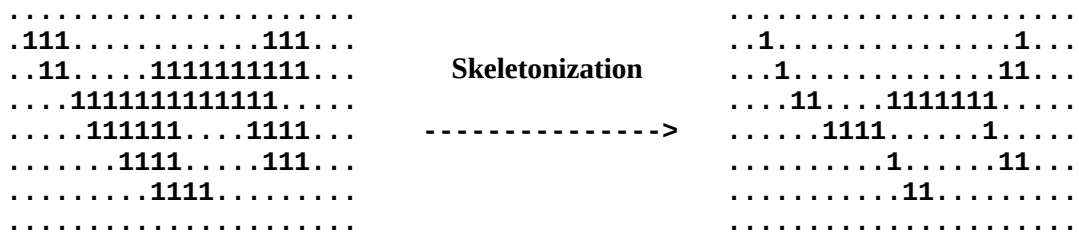

Figure 6-5 Example skeletonization: objects are thinned in sequences of four passes, in which pixels are removed, without affecting the 8-connectivity of objects and removing the end pixels, from the top and left, the bottom and right, the bottom and left and the top and right in turn; the sequence is repeated until the image is stabilized.

The skeletonized fringes are then subjected to a post-processing algorithm comprising: (1) the separation of the aggregate structures, (2) reconnection of the disconnected segment structures, (3) removal of small fringes. First, fringes are numerically inspected until a pixel with three neighbors is found, indicating a junction in a compound fringe. When an intersection is encountered, the angle between each of the lines and its two neighbor segments is calculated. The angle that is closest to 180 degrees is found and the two segments that form this angle are left joined while the third segment is detached by removing the pixel along its length that touches the three neighbor pixel (Figure 6-7 bottom). If the newly formed line contains fewer than the threshold number of pixels, it is removed at this time (Figure 6-7 top).

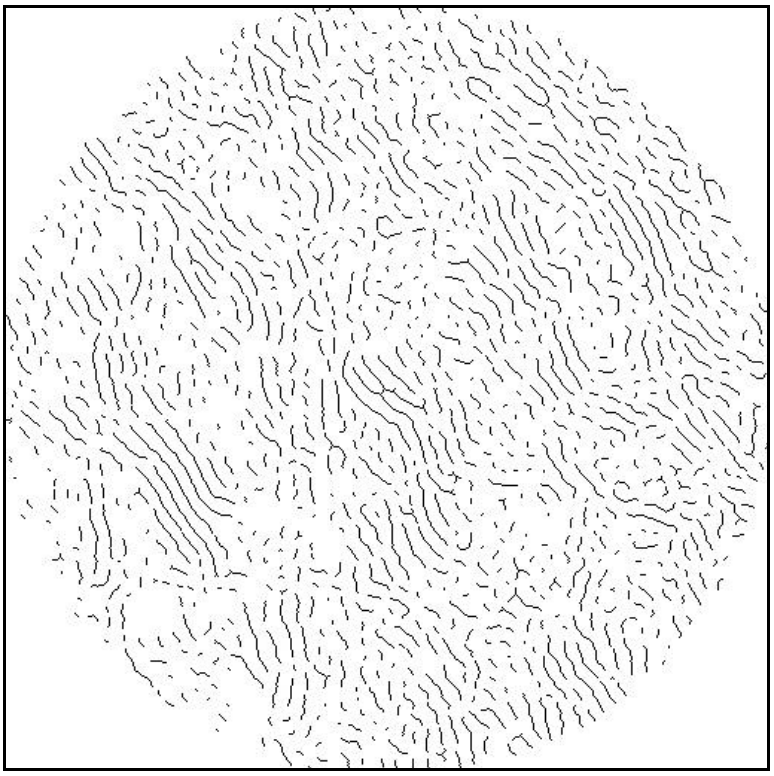

Figure 6-6 Skeletonized fringe image of partially combusted coal char (from Figure 6-4).

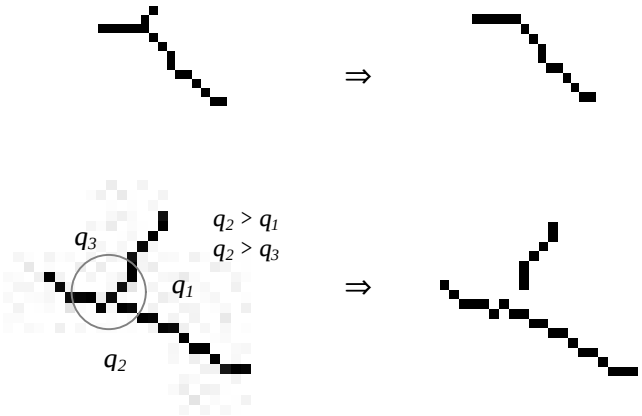

Figure 6-7 An example of separation and removal.

Each fringe is considered once more to identify possible disconnected segment structures. The neighborhood of a fringe end is searched for other fringe ends lying within 10 pixels and having a similar orientation (+/- 30 °) to the original fringe. If such a fringe is found, the two structures are joined (see Figure 6-8).

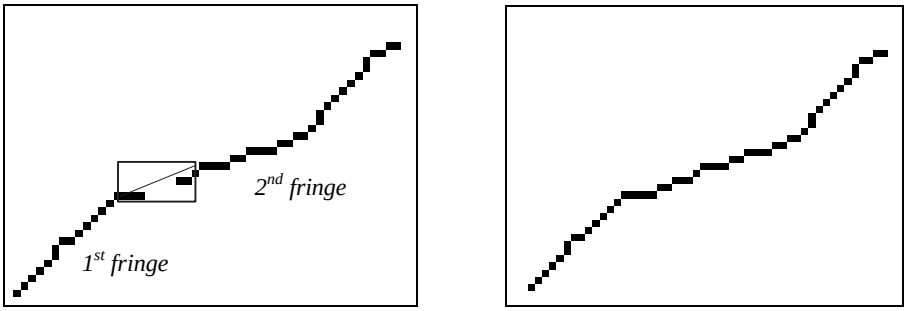

Figure 6-8 An example of reconnection of the disconnected segments.

Finally, fringes with length below 1.5 nm are removed from the fringe population. This last step separates the clearly recognizable fringes from smaller objects that lack sufficient structure to distinguish them clearly from noise or noncrystalline features in the image. Exceptionally short fringes are most likely the result of noise and can be removed without significant loss of data (see Figure 6-7 top). In some sense, the user is free to choose this cutoff, and in doing so adopts a working definition of disordered carbon — in this case all material not found in recognizable fringes above 1.5 nm in length. The 1.5 nm cutoff was chosen for inclusion in the final algorithm by a calibration procedure involving samples whose mean crystallite size had been previously determined by X-ray diffraction line broadening [12]. HRTEM images of these samples were processed and mean fringe lengths sizes determined for various values of the minimum fringe size cutoff. The best cutoff value gave a reasonable match between the mean fringe length and L_a value from the two different techniques (see Figure 6-9).

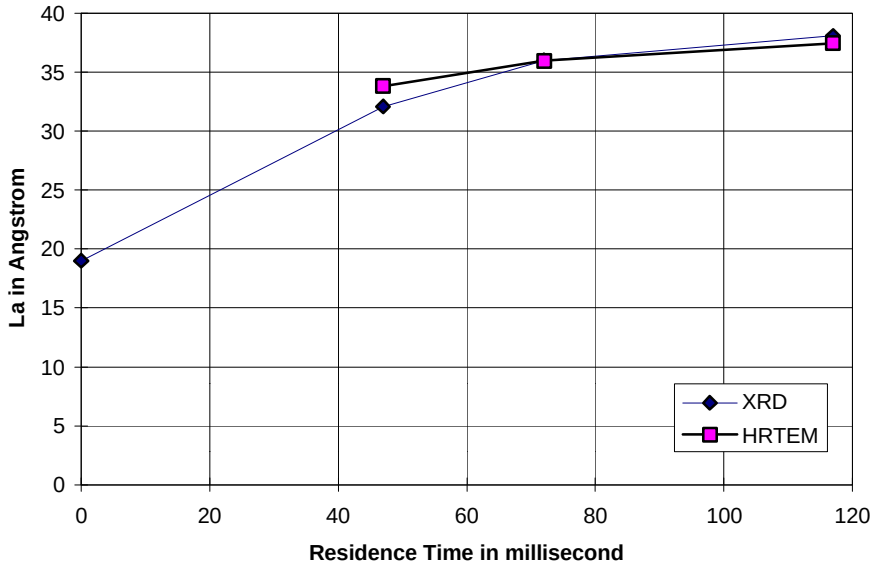

Figure 6-9 Mean crystallite dimension (L_a) from XRD and mean fringe length from HRTEM image analysis.

The entire image is edited in this manner to produce simple binary images which are used in the quantitative analysis of structure (see Figure 6-10). Note that fringe between 0.5 and 1.5 nm are included in the graphical image presentations, but are not used in the calculation of statistics.

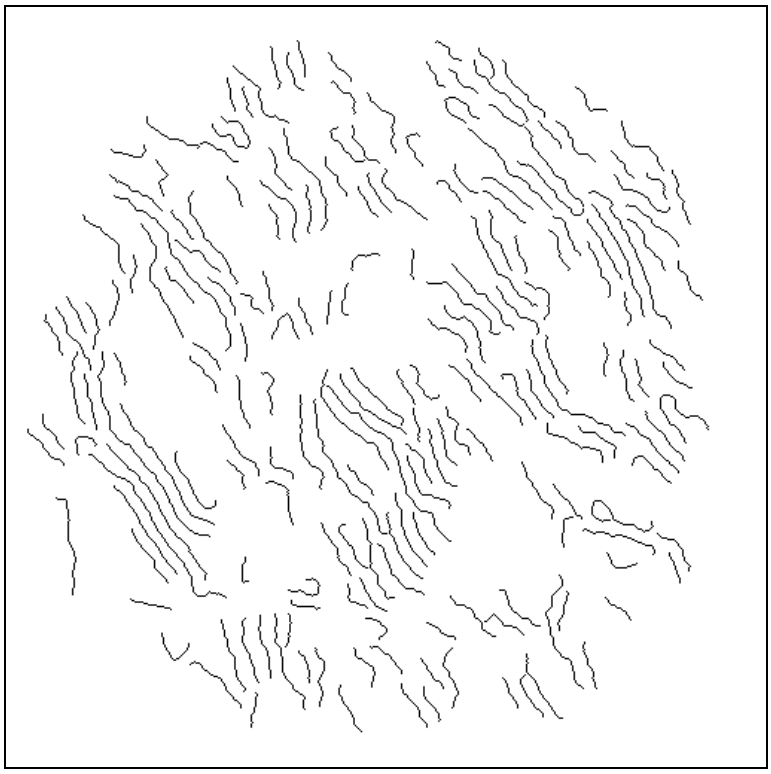

Figure 6-10 Processed fringe image of Figure 6-6

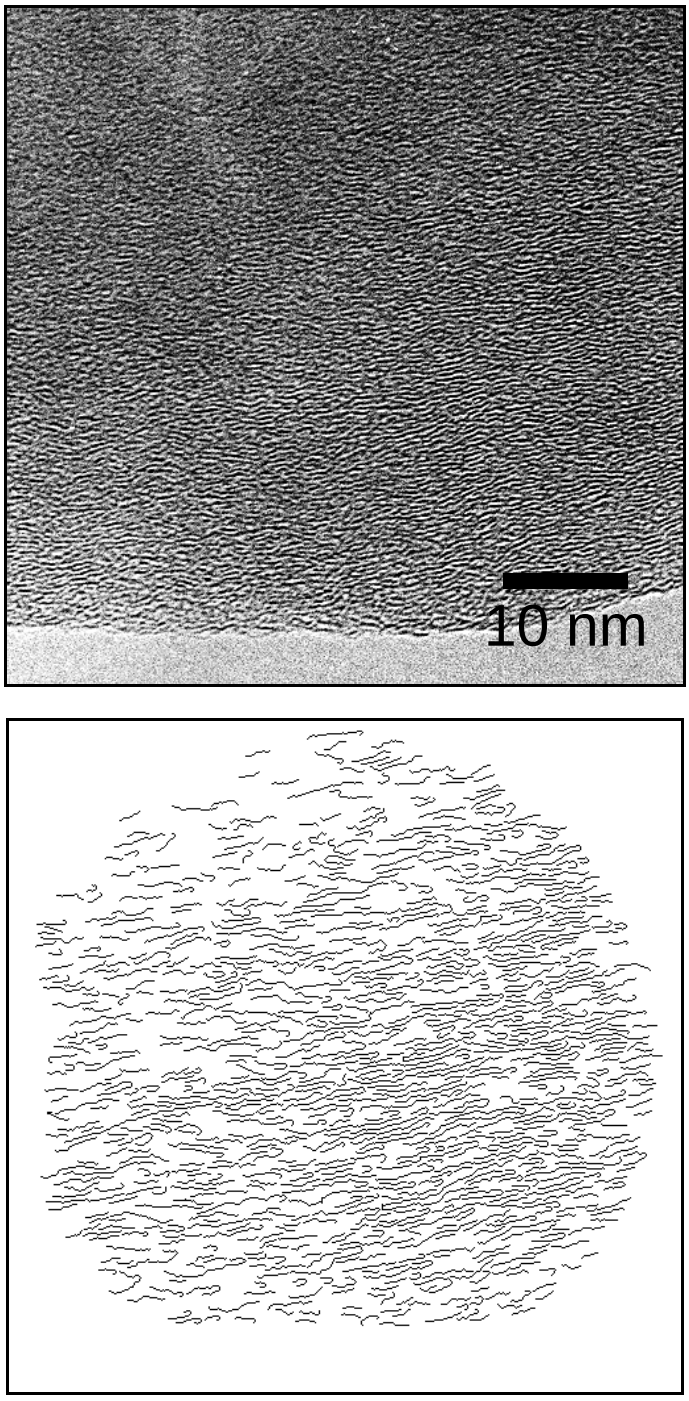

Figure 6-11 Raw and processed 002 LF image of high-rank, low-volatile bituminous coal char (Pocahontas) sampled from an entrained flow reactor in the early stages of combustion. Residence time: 47 msec; particle temperature: ~ 1700 K. Sample shows mesophasic long-range orientational order. (Smallest fringe shown is 5Å in length)

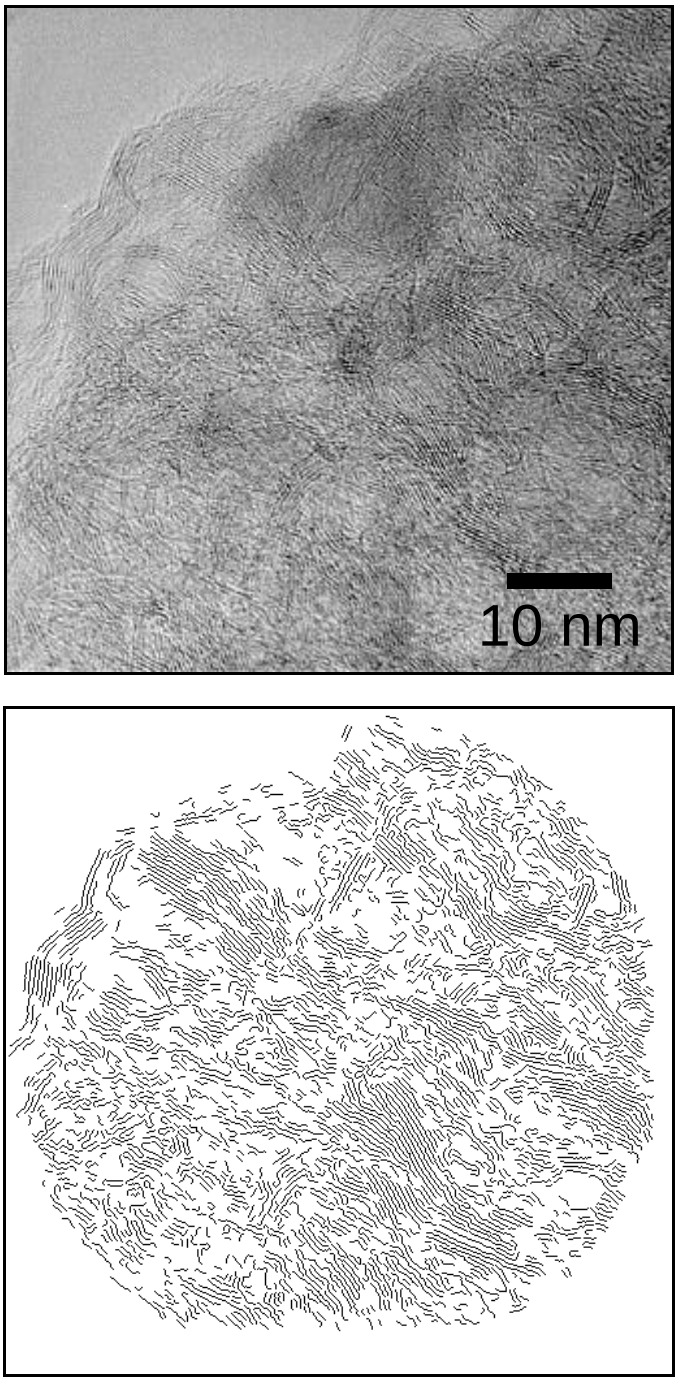

Figure 6-12 Raw and processed 002 LF image of lignite char generated by heat treatment at 2400 K in helium for four seconds. Sample shows primary short-range orientational order in the form of 5 – 10 nm domains along with low-grade statistical long-range orientational order among the domains.

6.2 Structure Parameters

Having reduced the complex fringe image to a set of distinct fringes, it is now possible to define and compute quantitative order indices based on readily-available object oriented image analysis functions. Fringes can be classified according to their size (length), planarity, and spatial arrangement. These structural characteristics will be represented in terms of structure parameters defined during this work: including length, tortuosity, and orientational order parameter. We are particularly interested in characterizing the degree of preferred orientation as a function of length scale — some coal chars exhibit short range order (but no long range order), while often exhibiting gross anisotropy over long length scales (> 1μm). The extent of orientational order is also an important aspect of carbon structure.

6.2.1 Fringe Length

Fringe length (L_i) is calculated by counting the number of pixels along the fringe and computes the length using a calibrated pixel size. This calculation includes a correction factor for diagonally-oriented fringe segments in which the effective pixel size is larger by a factor of $\sqrt{2}$. Mean fringe length is obtained using an averaging technique consistent with X-ray diffraction theory(see equation(6-1))) [30, 31].

(6-1)

$$\sum L_i^{\,2} \Big/ \sum L_i$$

An example distribution of fringe length from the processed fringe image (Figure 6-10) is shown in Figure 6-13. Mean fringe length is 83.2 in pixels (3.53 nm).

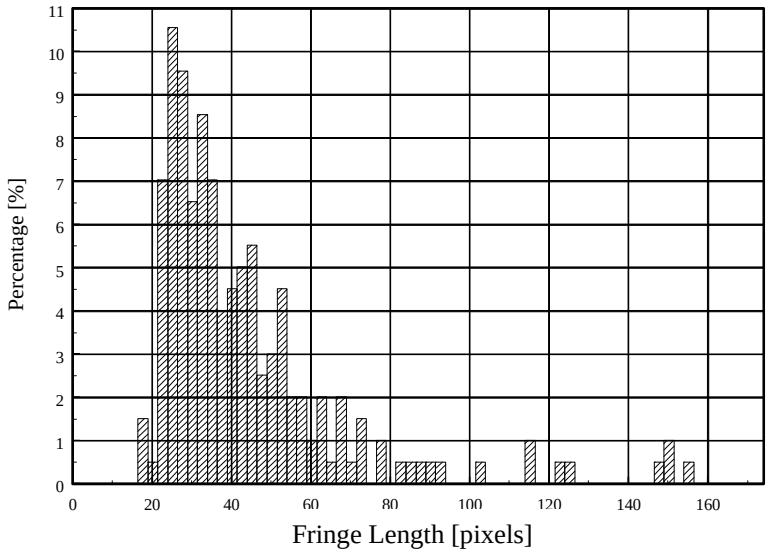

Figure 6-13 Histogram of fringe length in Figure 6-10.

6.2.2 Tortuosity

Tortuosity represents the degree of curvature in the fringe. A simple parameter can be defined by dividing a crystallite diameter by a diagonal length of a box enclosing the individual fringe (see Figure 6-14).

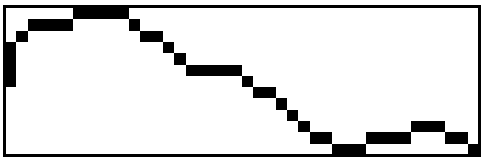

Figure 6-14 A box enclosing the fringe.

Tortuosity has a value larger than one for most cases and one for the straight line. The straighter the line is, the lower the tortuosity. An example distribution of tortuosities from the processed fringe image (Figure 6-10) is shown in Figure 6-15. The mean tortuosity is 1.18.

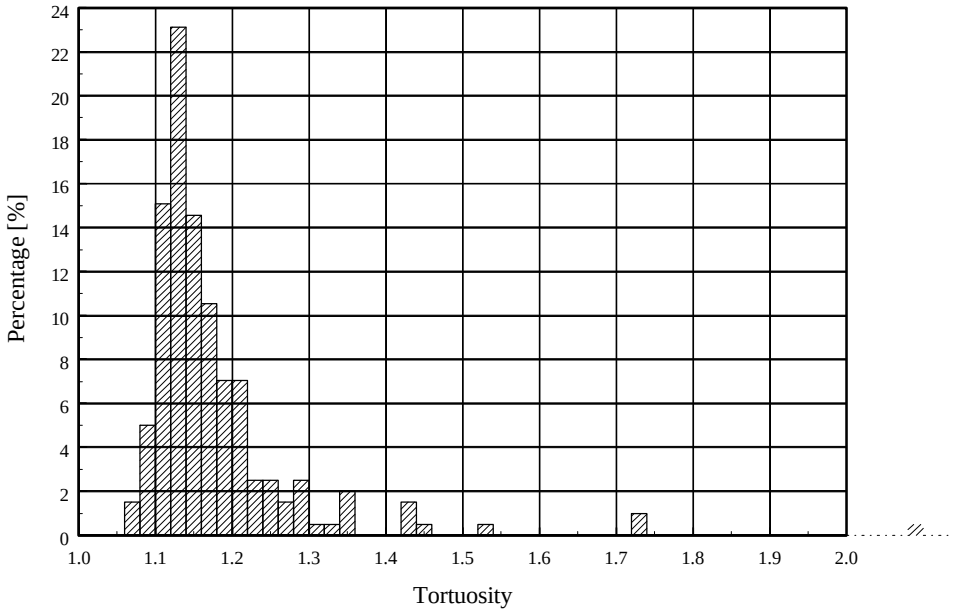

Figure 6-15 Histogram of tortuosity in Figure 6-10.

6.2.3 Apparent Crystalline Fraction

The amount of ordered material varies greatly among fringe images and is quantified here as:

$$\sum L_i \Big/ \left(\sum L_i\right)_{\max} \qquad \textbf{(6-2)}$$

where SL_i is the sum of all recognized layers larger than the acceptance threshold, and $(SL_i)_{max}$ is the same value for a theoretical graphitic structure that fills the image field at 3.35 Å spacing. The image regions that do not contain recognizable layers may contain either porosity, amorphous material, or ordered domains with orientations that do not fulfill the Bragg conditions, it is therefore not possible to associate this parameter with a true crystalline fraction, and $SL_i/(SL_i)_{max}$ is therefore referred to as an "apparent crystalline fraction".

6.2.4 Orientational Order Parameters

Figure 6-16 depicts simple order modes for disk-like molecules in three dimensions and their rod-like projections in two dimensions. Nematic order, a term used to describe liquid crystalline phases, refers to alignment along a unique unit vector describing the preferential orientation of the entire field, that vector being referred to as the director. Note in Figure 6-16 that the director and orientational unit vectors are defined parallel to the long axis of rods (or two-dimensional projection of discs), but perpendicular to the basal planes of disks in three dimensions by convention. Order around a point or pole in two dimensions can be concentric or radial. In three dimensions concentric order can be spherical (as in carbon blacks) or cylindrical (as in some carbon fibers). Radial order in three dimensions can also be spherical (though it is not typical of carbon structures) or concentric, as found in some carbon fibers. Many carbon fibers exhibit axial order, or mixed modes with axial order in the core and concentric order in an outer skin [32]. Equatorial stacking such as found in Brooks-Taylor mesospheres is not treated as a separate category, but as a nematic phase perturbed to curvature by interfacial tension. Because the relevant length scales for BT mesospheres are long (on the order of micrometers), the curvature is gradual and the underlying microscopic order is for most purposes best regarded as nematic. An alternative scheme has been described by Oberlin [16], in which carbon nanostructures are classified as spherical and cylindrical, with nematic order treated as a special case of spherical order in which the radius of curvature is very large. Also, Inagaki [33] considers two types of spherical order, concentric (as in carbon blacks) and equatorial (as in Brooks-Taylor mesospheres) and discusses their formation mechanisms in terms of edge vs. basal plane energies.

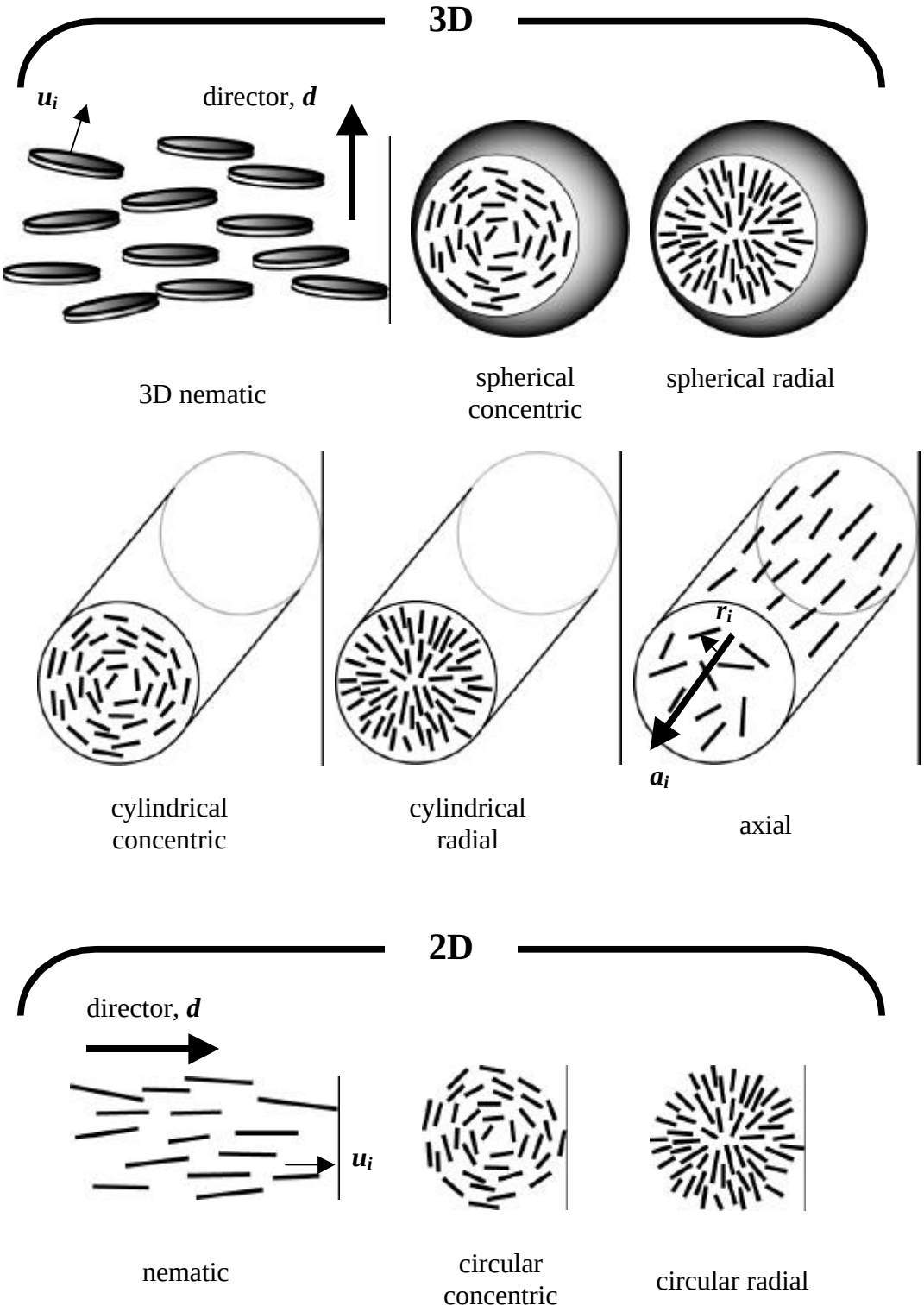

Figure 6-16 Simple orientational order modes among disk-like objects in three dimensions and their two dimensional projection.

Sections below give definitions of quantitative order parameters for the various modes shown in Figure 6-16. The parameters are defined to be one in the case of perfect order and zero for complete disorder (randomly aligned layers). The two dimensional parameters are most useful for the analysis of single HRTEM fringe images, while the three dimensional analogs are primarily useful in computer simulations or in reconstructions of actual structures inferred from TEM image sequences obtained upon sample rotation.

6.2.4.1 Three-dimensional Order Parameters

The lowest orientational order mode for disk-like objects is axial orientation (see Figure 6-16) in which the unit vectors all lie in a common plane, and are thus perpendicular to a unique directional vector. This type of order is seen many carbon fibers, where the preferential axial alignment induced by elongation during fiber spinning and stretching and the extent of axial alignment correlates strongly with the Youngs modulus along the fiber axis [32]. In this simple mode, there is no preferred orientation of the planes when viewing along the axis, An axial order parameter in three dimensions can be defined as:

(6-3)

$$S_{3A} = 1 - 3\left\langle \cos^2(q_i) \right\rangle = 1 - 3\left\langle (\vec{a} \bullet \vec{u}_i)^2 \right\rangle$$

where q_i is the angle between the axis of particle i (the i^{th} directional unit vector, $\boldsymbol{u_i}$) and the axis of symmetry, $\boldsymbol{a}$, and the brackets denote an average (see vector definitions in Figure 6-16). The second term is an equivalent form in vector notation. This order parameter is one for perfect axial order and zero for a phase with completely random alignments. A high value indicates simple axial order or, alternatively, nematic order (a higher order degree). An additional order parameter is required to distinguish the two. The nematic order parameter, often used to describe liquid crystalline phases [34], is defined by:

(6-4)

$$S_{3N} = \frac{3}{2}\left\langle \cos^2(q_i) \right\rangle - \frac{1}{2} = \frac{3}{2}\left\langle \left(\vec{d} \bullet \vec{u}_i\right)^2 \right\rangle - \frac{1}{2}$$

where q_i is the angle between the axis of particle i ($\boldsymbol{u_i}$) and the mean orientation (the director, $\boldsymbol{d}$). For large N, the nematic order parameter is zero when the molecular axis are randomly distributed, and one in a system where the axis of each layer is perfectly aligned with the director. Note that perfect simple axial order yields $S_{3A} = 1$ and $S_{3N} = 1/4$.

A polar order parameter in three dimensions, S_{3P}, can be defined for both spherical and cylindrical symmetry as:

(6-5)

$$S_{3P} = \frac{3}{2}\left\langle \cos^2(q_i) \right\rangle - \frac{1}{2} = \frac{3}{2}\left\langle \left(\vec{r}_i \bullet \vec{u}_i\right)^2 \right\rangle - \frac{1}{2}$$

For spherical symmetry, q_i is the angle between the orientational unit vector $\boldsymbol{u_i}$ and the positional unit vector, $\boldsymbol{r_i}$, that points from the origin or "pole" to the midpoint of disk i (see Figure 6-16). This order parameter is +1 for spherical concentric and zero for disorder (limits are for large N).

For cylindrical symmetry $\boldsymbol{r_i}$ is interpreted as the position unit vector pointing from the midpoint of disk i to the closest point on the cylinder axis. This order parameter is +1 for cylindrical concentric order, and –1/2 for cylindrical radial order (or for simple nematic if the director is the cylindrical axis). To distinguish cylindrical radial order from simple nematic order, one requires the following additional order parameter:

(6-6)

$$S_{3CR} = \frac{3}{2}\left\langle \left(\vec{v}_i \bullet \vec{u}_i\right)^2 \right\rangle - \frac{1}{2} \quad ; \quad where\ \vec{v}_i \equiv \vec{r}_i \times \vec{a}_i$$

where a new vector, $\boldsymbol{v_i}$ is defined as the unit vector perpendicular both to the symmetry axis vector, $\boldsymbol{a_i}$, and to the positional vector, $\boldsymbol{r_i}$. This parameter distinguishes cylindrical radial order (where unit directional vectors are perpendicular to the axis) from

simple nematic order (where the unit vectors are parallel to the axis), being +1 for perfect cylindrical radial order and –1 for simple nematic order.

6.2.4.2 Two-dimensional Order Parameters

The situation in two dimensions is less complex, requiring only two order parameters: nematic and polar. Special attention is paid here to the quantitative calculation of these parameters, as they find active use in the analysis of fringe images. A two dimensional version of the nematic order parameter is defined as:

(6-7)

$$S_{2N} = 2\left\langle \cos^2(q_i) \right\rangle - 1 = 2\left\langle \left(\vec{d} \bullet \vec{u}_i\right)^2 \right\rangle - 1$$

This parameter is one for perfect order and, when N is large, it is zero for a disordered phase with completely random orientations. In the general case the director cannot be found by a simple averaging procedure, but is the eigenvector corresponding to the largest eigenvalue from solution of:

(6-8)

$$Q\,\vec{d} = l\,\vec{d}$$

where ***d*** is the director and Q is the ordering tensor [35]:

(6-9)

$$Q \equiv \left(\frac{1}{N}\right)\sum \begin{pmatrix} x_i x_i - \frac{1}{2} & x_i y_i \\ y_i x_i & y_i y_i - \frac{1}{2} \end{pmatrix}$$

where x_i and y_i are then endpoints of the directional unit vectors for object i. Many carbon materials, particularly non-graphitizing ones, exhibit short range orientational order, but no long range order. It is desirable to be able to calculate the extent of this order as a function of length scale, which is related to the determination of sizes for individual crystallites or molecular orientation domains. A length-dependent nematic order parameter can be determined by selecting a series of circular image regions

each of a fixed radius, computing the order parameter within each circle, averaging the results, and reporting a mean order parameter, *S(r)* as a function of the chosen radius.

6.2.4.3 Modification of Nematic Order Parameter in 2D

We have found that the simple nematic order parameter in equation (6-7) is inadequate for disordered samples at small length scales, where the number of fringes present is often small (< 10). For small *N*, even randomly distributed layers with completely uncorrelated orientations (Figure 6-17) yield order parameters systematically greater than zero. This effect arises when the director is calculated from the small set of fringes themselves, but disappears if the director is known *a priori*. Figure 6-18 shows a stochastic calculation of the expected value of the conventional nematic order parameter for random lines as a function of sample size *N*. For small *N* the expected value is much greater than the desired value of zero. An analytical solution to this problem was derived for $N = 2$ yielding $S_{2N} = 2/\pi$, in close agreement with the numerical solution in Figure 6-18. In the practical analysis of 002LF images, the director is indeed determined from the fringe population, so a modified definition or the order parameter is needed for length-dependent calculations. The modified two-dimensional nematic order parameter is:

(6-10)

$$S_{m2N} = \frac{\left[S_{2N} - F(N)\right]}{\left[1 - F(N)\right]}$$

where *F(N)* is the Shim function in Figure 6-18. The expected value of this parameter vanishes where no order is found and is one for a perfect alignment. An example nematic order parameter as a function of length scale is shown in Figure 6-19.

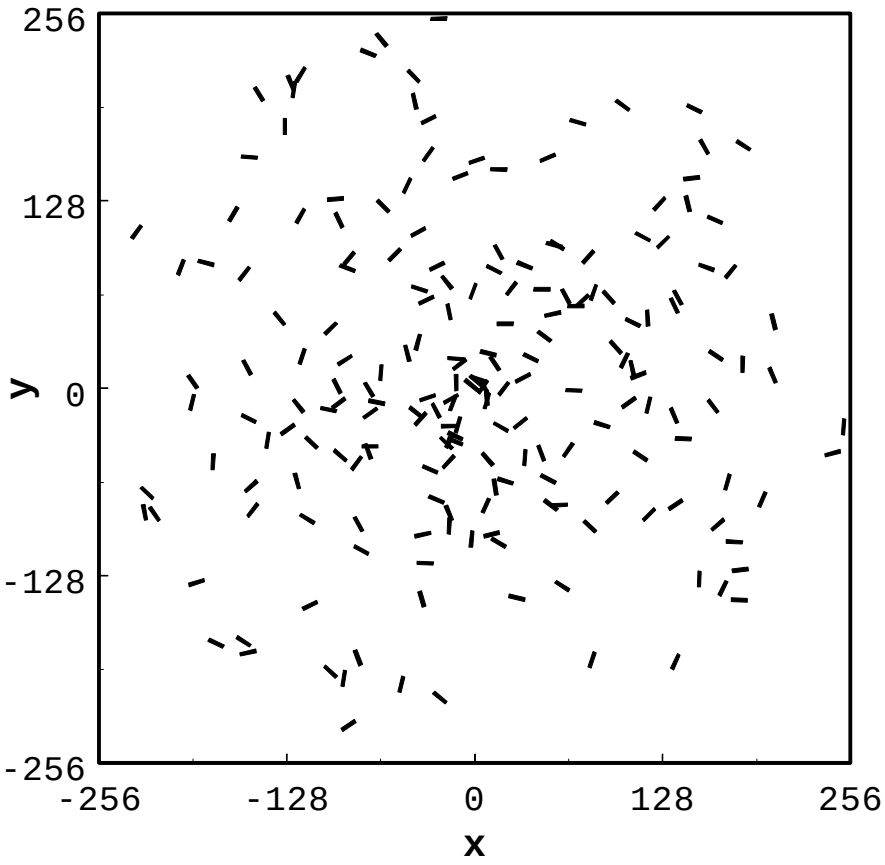

Figure 6-17 Lines with random orientation generated with pseudo random function.

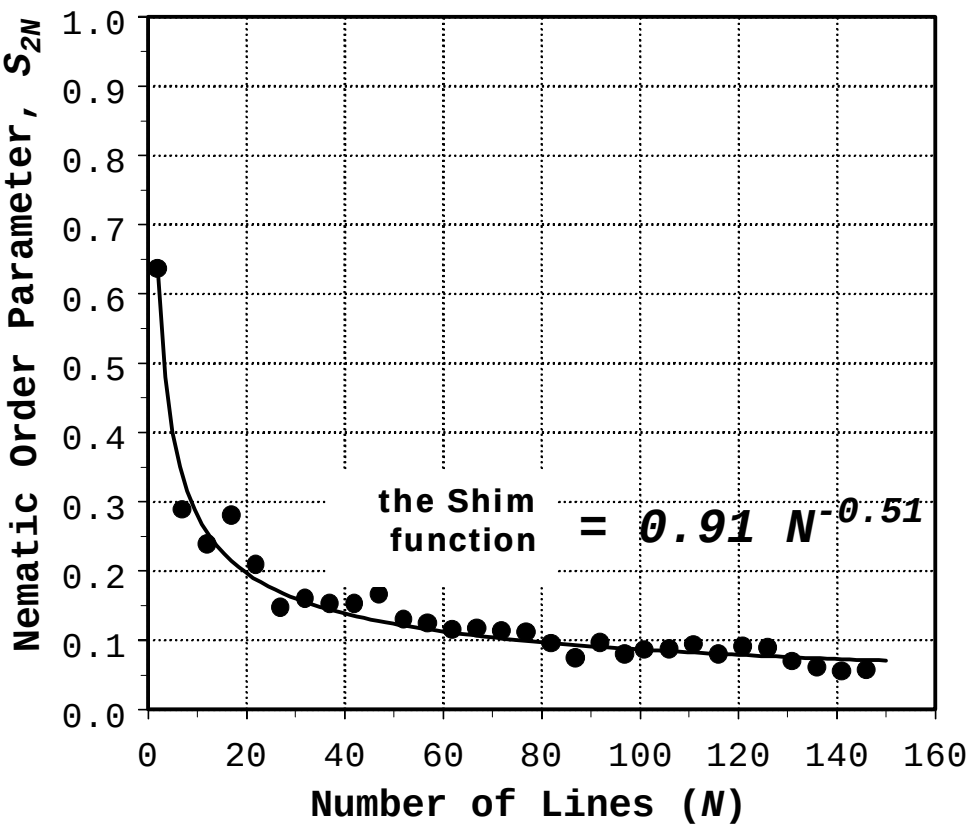

Figure 6-18 Nematic order parameter in two dimensions for sets of N randomly oriented lines (see Figure 6-17) as computed by stochasitic simulation. Analytical solution for $N = 2$ is $S_{2N} = 2/\pi$. The Shim function shown is used to define a corrected nematic order parameter for small sample sets that has an expected value of zero for random orientations.

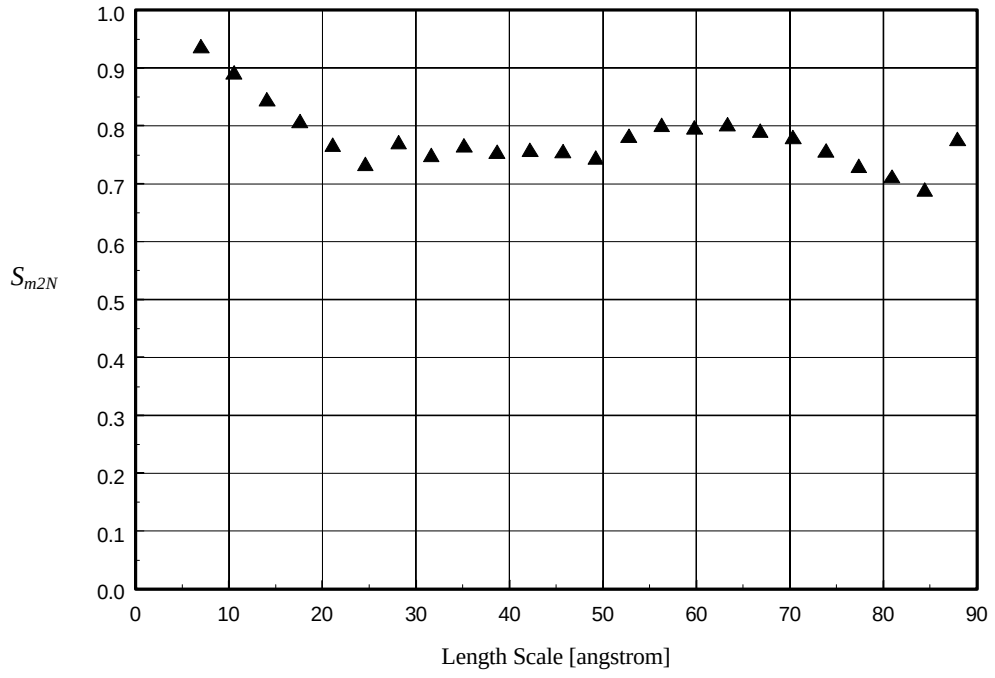

Figure 6-19 Nematic order parameter (S_{m2N}) as a function of length scale from Figure 6-10.

The image in Figure 6-10 shows very high order (over 0.9 in S_{m2N}) at short range and maintains the high order (S_{m2N} ~ 0.75) throughout the all length scale. In fact, the image in Figure 6-10 is from an extracted residual carbon from power plant fly ash and we can expect high degree of orientational order through a thermally induced structure alignment. S_{m2N} for a whole image is 0.78.

With a fixed radius, we can calculate *fractional* S_{m2N}. An example distribution of S_{m2N} in Figure 6-10 with 2.5 nm, r_c is reproduced in Figure 6-20. It shows high population in high order region.

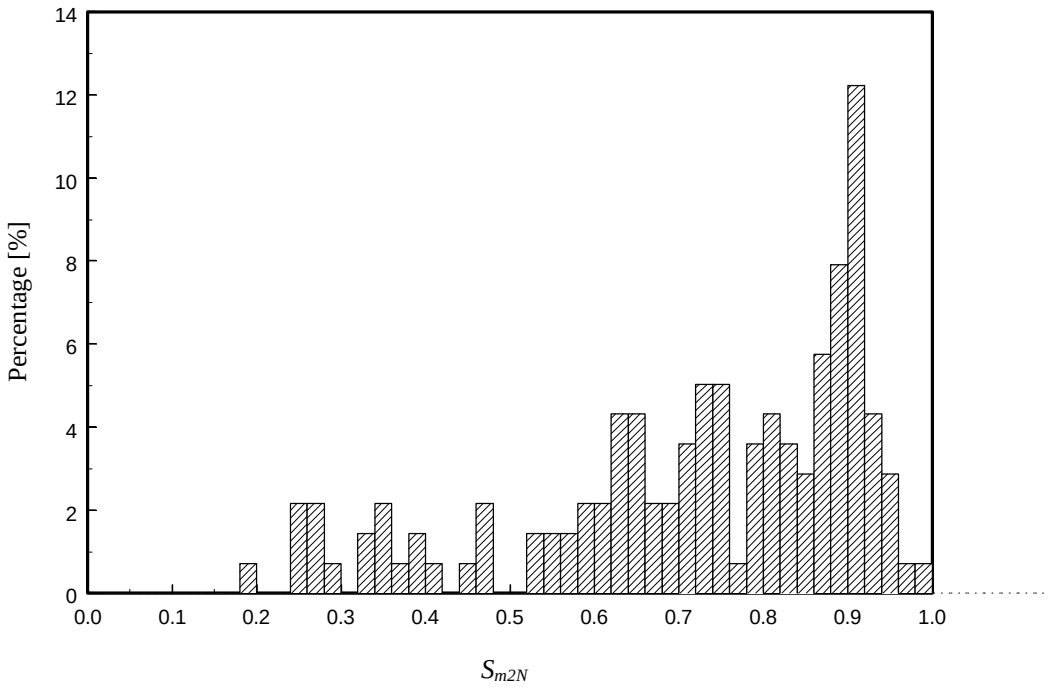

Figure 6-20 A distribution of S_{m2N} with 2.5 nm, r_c in Figure 6-10.

6.2.4.4 Polar Order Parameter

In a similar way, we defined the a two-dimensional polar order parameter for fringes with either concentric or radial symmetry:

(6-11)

$$S_{2P} = 1 - 2\left\langle \cos^2(q_i) \right\rangle = 1 - 2\left\langle (\vec{r}_i \bullet \vec{u}_i)^2 \right\rangle$$

where $\boldsymbol{u_i}$ is the direction unit vector, and $\boldsymbol{r_i}$ the position vector relative to the pole, which in two dimensions is a point. A pole is always chosen prior to calculating S_{2P}, so there is not need to correct the polar order parameter for statistical bias as was done for the nematic parameter. This order parameter has a value of unity for concentric symmetry, -1 for radial symmetry, and zero for lines with random orientation. Schematic of the conceptual polar order parameter calculation is shown in Figure 6-21. Use of this parameter requires specification of the origin or pole. By rastering a fixed aperture of

radius r_c, across the image and computing S_{2P} at each position, an appropriate pole is found at the maximum value for concentric order or the minimum value for radial order.

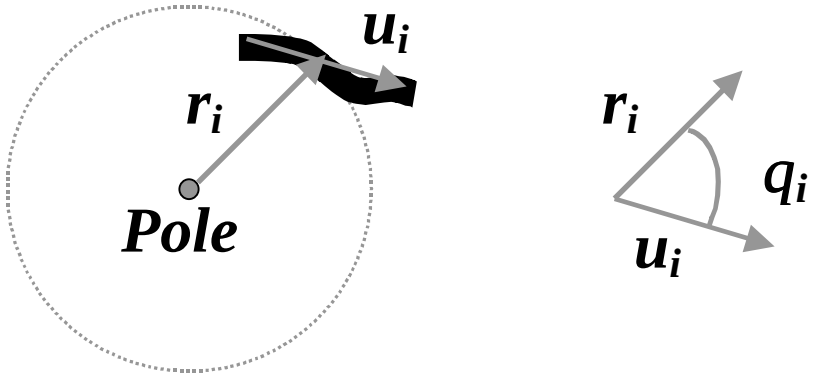

Figure 6-21 Schematic of the conceptual polar order parameter calculation: u_i is a direction unit vector of fringe i, and r_i positional unit vector relative to the pole

An example of this process and results of calculation are shown in Figure 6-22 and Figure 6-23. Figure 6-22 a) shows ethylene soot particle having concentric symmetry, i.e. onion structure with approximately 60 nm radius. The raw image (a) is processed in the same way as described before and the resultant binary image is reproduced in Figure 6-22 b). Figure 6-22 c) shows polar order parameters, S_{2P}, computed for the entire image using various trial poles (x, y ordered pairs) in the image plane. The maximum S_{2P} corresponds to the apparent nucleus of the concentric structure — the optimum pole. Positive values indicate concentric rather than radial order. Figure 6-23 shows length-dependent polar order parameters, S_{2P} (L), vs. length scale, L, of the region of interest. The degree of concentric order is seen to increase from near zero in the vicinity of the pole to about 0.7 at the particle periphery. Such amorphous core regions have been attributed to electron imaging limitations [16] and to increasing strain in the concentric structure associated with high curvature near the pole.

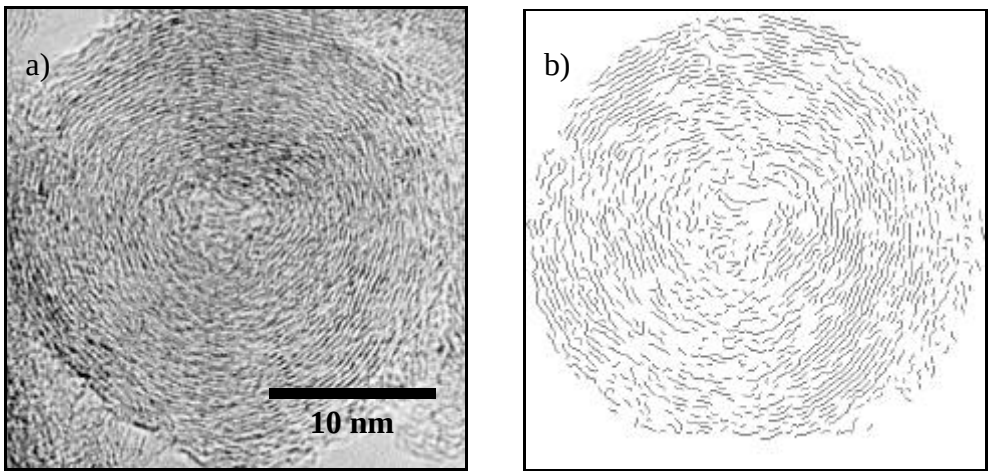

c)

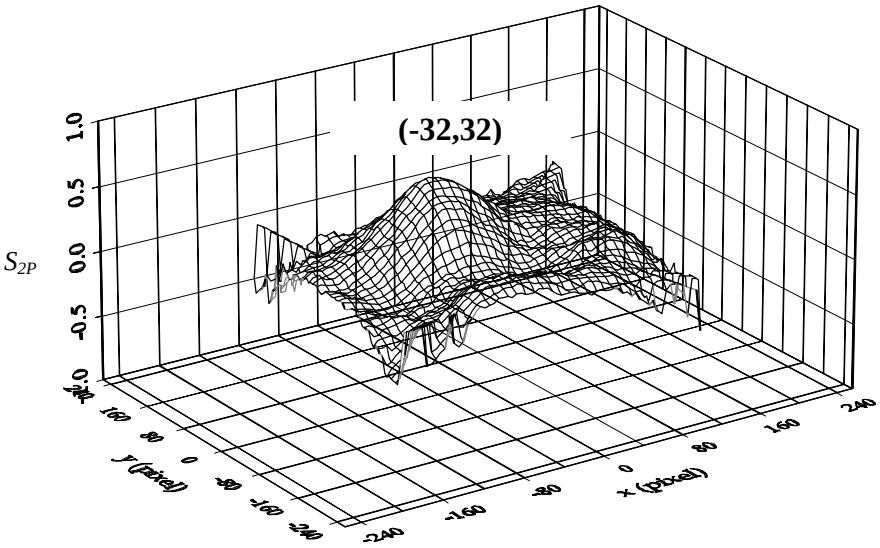

Figure 6-22 a) and b): Raw and processed 002LF image of ethylene soot provided courtesy of Adel Sarofim and Lenore Rainey at MIT. Sample shows characteristic concentric order. c) Application of polar order parameter to the ethylene soot fringe image. Two dimensional map of S_{2P} yields the optimal pole-the apparent nucleus of the concentric structure.

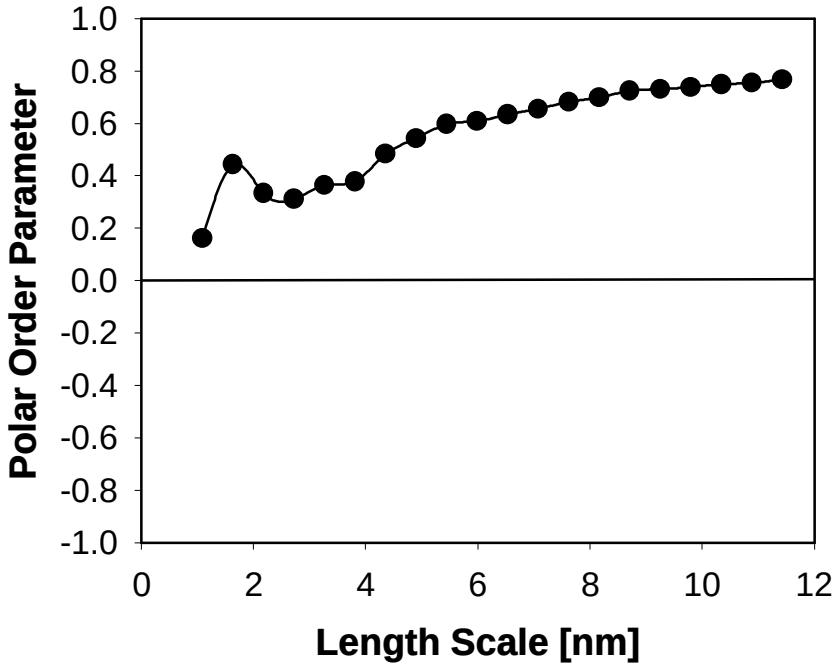

Figure 6-23 Calculation of length dependent polar order parameter at the optimum pole from Figure 6-22 c). Positive values indicate concentric order (rather than radial order) and the extent of order increases with distance from the nucleus.

6.3 An Application to Combustion-derived Solid Fuel Chars

6.3.1 Sample Preparation

An important objective of this work is to characterize the nanostructures of combustion-derived chars from a wide range of solid fuels. Quantitative digital analysis was applied to HRTEM 002 LF images taken from earlier studies in which chars were generated by partial combustion in a well-characterized, high-temperature, entrained flow reactor from Illinois #6 coal [12] and from two biomass samples, switchgrass and southern pine [18]. To complete the set of solid fuel types, additional experiments were performed in this study under the same conditions to generate a series of partially

combusted chars from Pocahontas #3 low-volatile bituminous coal, Pittsburgh #8 high volatile bituminous coal, and Beulah lignite. Properties of the parent fuels are summarized in Table 6-2.

The chars had been generated as described elsewhere [12]. Briefly, a honeycomb flat-flame burner holds a H_2 / O_2 / N_2 flame that produces hot, vitiated air into which single coal or biomass particles (75 – 125 μm in diameter) are fed carried by a small nitrogen flow. The stoichiometry of the reactor's H_2 / CH_4 / O_2 / N_2 flame is tailored to produce postflame gases simulating those in the upper furnace region of pulverized-fuel-fired boilers. The reactor was operated at a gas condition of nominally 1600 K. The reactor and experimental conditions are described in detail elsewhere [36, 37, 38,10]. The reactor is equipped with a rapid-quench, He-injection, water-cooled, sampling probe for removal of partially reacted char particles at known residence time up to 120 msec. Char samples were collected at residence times of 47, 72, 95, and 117 msec, yielding a range of carbon conversions from 0 % (at the end of devolatilization and beginning of char combustion) to a maximum value of 50 – 80 %. Oxygen concentration was systematically varied from 12 to 20 mole-% to produce similar peak particle temperatures (1900 ~ 2000 K) and similar degrees of carbon conversion for each of the precursors. A residence time of 47 msec corresponds, approximately, to the completion of devolatilization, the disappearance of the visible volatile flame, and the onset of heterogeneous oxygen attack on the young char.

The char samples were ground, dispersed in methyl alcohol ultrasonically, placed on a holey carbon grid, and examined in a Phillips Model CM30 microscope (spherical aberration coefficient of 2.0 mm) operating at 300 kV. Samples were first examined at moderate magnification to find wedge-shaped fragments that are optically thin at the edge. A number of such edge regions (typically ten or more) are then photographed at high magnifications (2,000,000×) in fringe imaging mode. Representative fields of view were selected for digital image analysis. An additional Beulah lignite char was prepared by rapid heating (2×10^3 K/sec) in helium to 2400 K followed by a 4 second hold time at peak temperature in a graphite resistance heater. This sample was examined in a JEOL JEM-2010 microscope operating at 200 kV at Brown University. Example images are shown in Figure 4-1, 10, 11, and 21. The image processing was carried out with a

combination of the commercial image analysis package SEMPER™ (Synoptics Ltd., Cambridge, UK) developed for microscopy applications, as well as custom C++ code segments.

Table 6-2 Properties of the Solid Fuels and Chars

Sample	|-------analysis of parent fuel, %daf------|							|--char conversions---|				
								for residence times of: msec				
	C	H	O	N	S	Volatile matter*	Combustion O_2, mol-%	0	47	72	95	117
Pocahontas #3	89.2	4.4	4.9	1.0	0.6	17.0	20	--**	0	27	42	50
Pittsburgh #8	82.9	5.4	8.7	1.7	1.2	39.9	12	--**	0	33	52	57
Illinois #6	75.0	4.8	13.4	1.5	5.4	44.7	12	--**	0	29	62	69
Beulah lignite	64.4	4.6	27.9	1.0	2.1	46.6	12	--**	0	68	90	95
Southern Pine[a]			***			20-25	6 or 12	0	53	73	86	95
Switchgrass[a]			***			20-25	12	0	48	76	91	94

* ASTM standard volatile matter
** raw coals
*** raw material for biomass combustion experiments were chars, prepyrolyzed at 625 ºC
a The conversion levels for biomass chars is the level of the dry-ash -free portions of the chars, calculated by using the refractory element Si as tracer

6.3.2 Quantitative Analysis of Structure

Example processed fringe images are shown in Figure 6-24 (early stages of combustion) and Figure 6-25 (later stages of combustion). Figure 6-26 shows four image regions from a single sample to illustrate the degree of variability in these structures and their derived properties. Complete list of processed HRTEM micrographs during this work is shown in Appendix.

Figure 6-24 clearly shows the variability in structures among the young chars prepared under identical conditions from five parent solid fuels. The two biomass chars and the high-volatile coal chars are quite disordered at this stage in combustion. The

amount of recognizably crystalline material is limited, typical fringe lengths are less than 3.4 nm, many fringes are tortuous, and most fringes appear as singlets or in stacks of two or three. These structures are similar to those observed in slow heating experiments for nongraphitizing carbons, including sacharose [39], and low-rank coals [40]. The lignite shows more order, with stacking heights from 2 – 6 fringes and mean fringe lengths between 3.6 and 4.0 nm. The high-rank coal, Pocahontas, exhibits a very different structure with larger mean fringe sizes (4.2 – 4.4 nm) and a high degree of long-range orientational order. Figure 6-25 shows modest changes in the nanostructures as a function of combustion conditions.

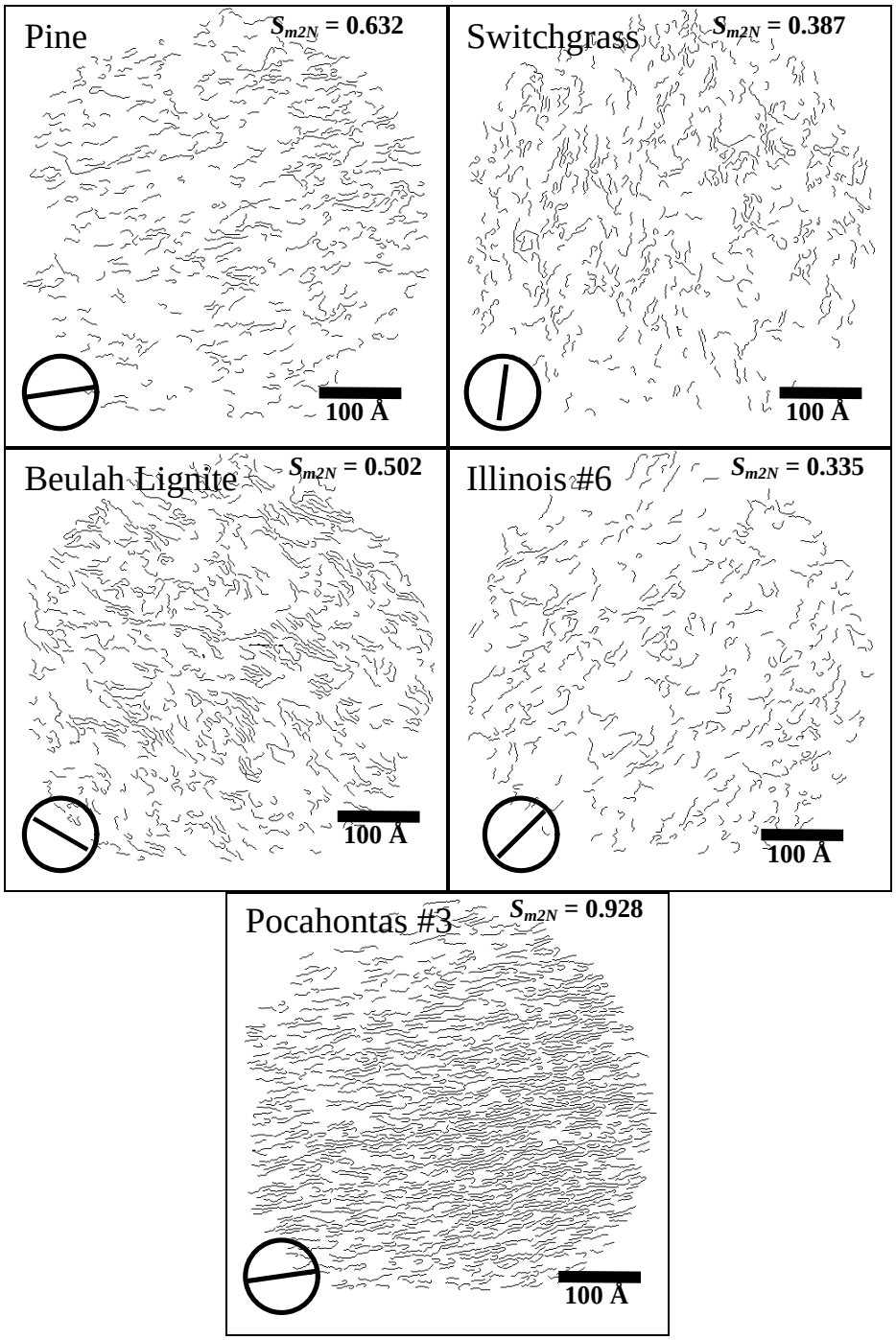

Figure 6-24 Example carbon nanostructures observed in young combustion-generated chars. Residence time: 47 msec; Particle temperatures: 1700 – 1900 K. Circle with embedded line gives the director for the entire field shown.

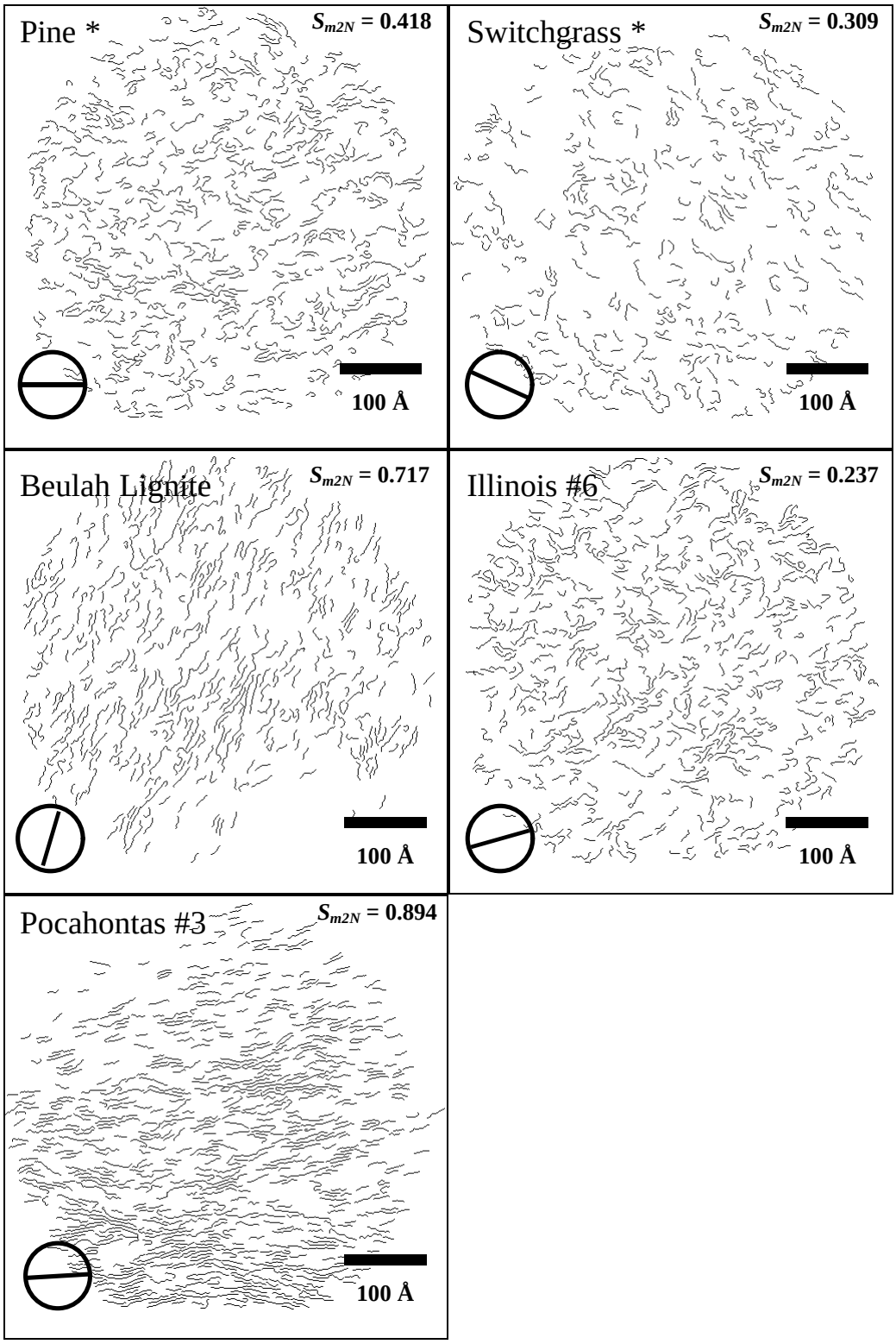

Figure 6-25 Example carbon nanostructures observed in combustion-generated chars from later times. Residence time: 117 msec (or 95 msec as marked with *); particle temperatures: 1700 – 1900 K

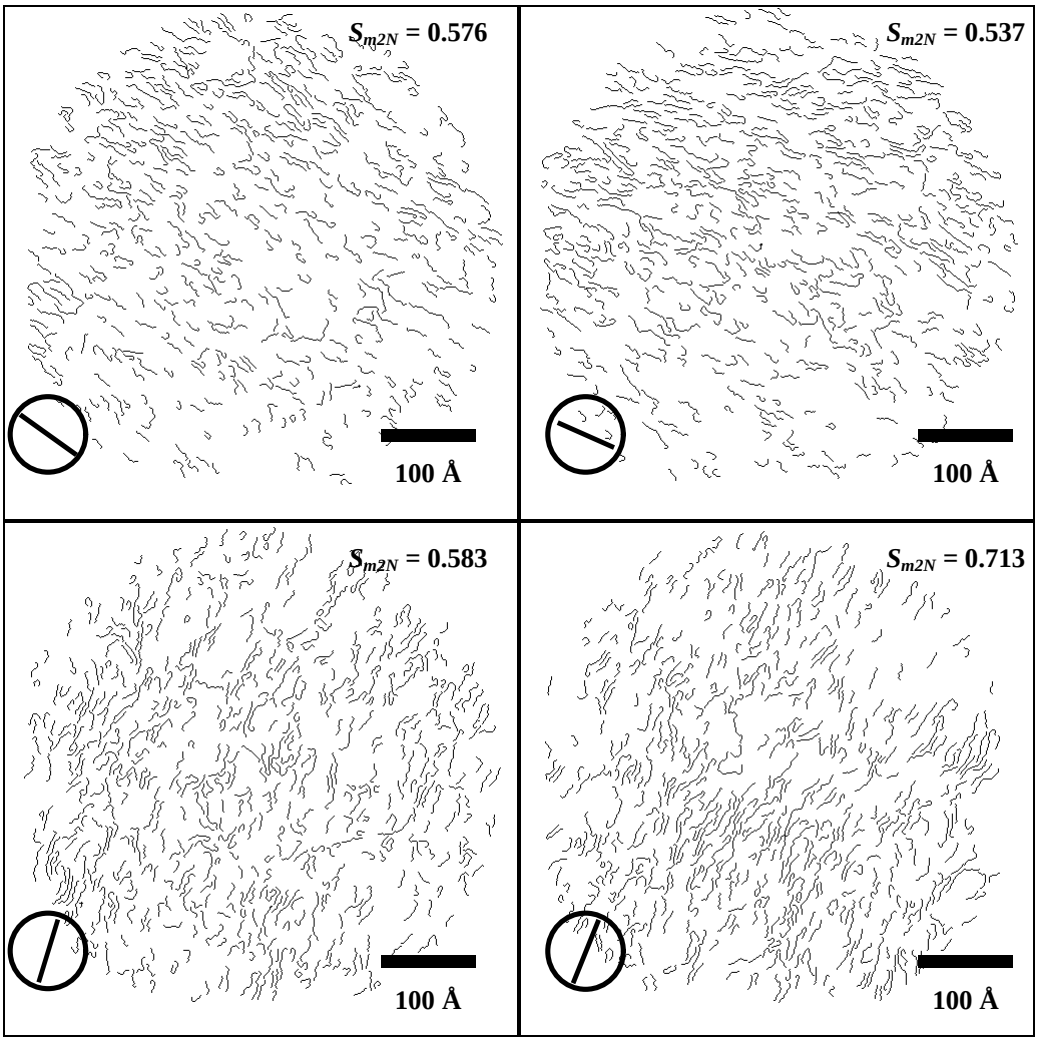

Figure 6-26 Set of four images from Beulah lignite char (residence time: 72 msec), demonstrating the degree of variability in fringe images within a single sample.

The following sections give the quantitative results for mean fringe length, tortuosity, apparent crystalline fraction, and nematic order parameter.

6.3.2.1 Mean Fringe Length

Mean fringe lengths for the suit of coals are shown in Figure 6-27. The lowest rank materials (from biomass) show the smallest sizes among chars investigated and maintain their levels throughout the combustion. The two high-volatile bituminous coals (Illinois #6 and Pittsburgh #8) undergo small increase from 47 msec to 72 msec. Residual carbon from Illinois #6 fly ash has 45 Å in mean fringe length. The high rank

Pocahontas char shows a large mean layer length after only 47 msec of residence time, suggesting an ordering process in the fluid stage of carbonization, which will be discussed in detail in the following section.

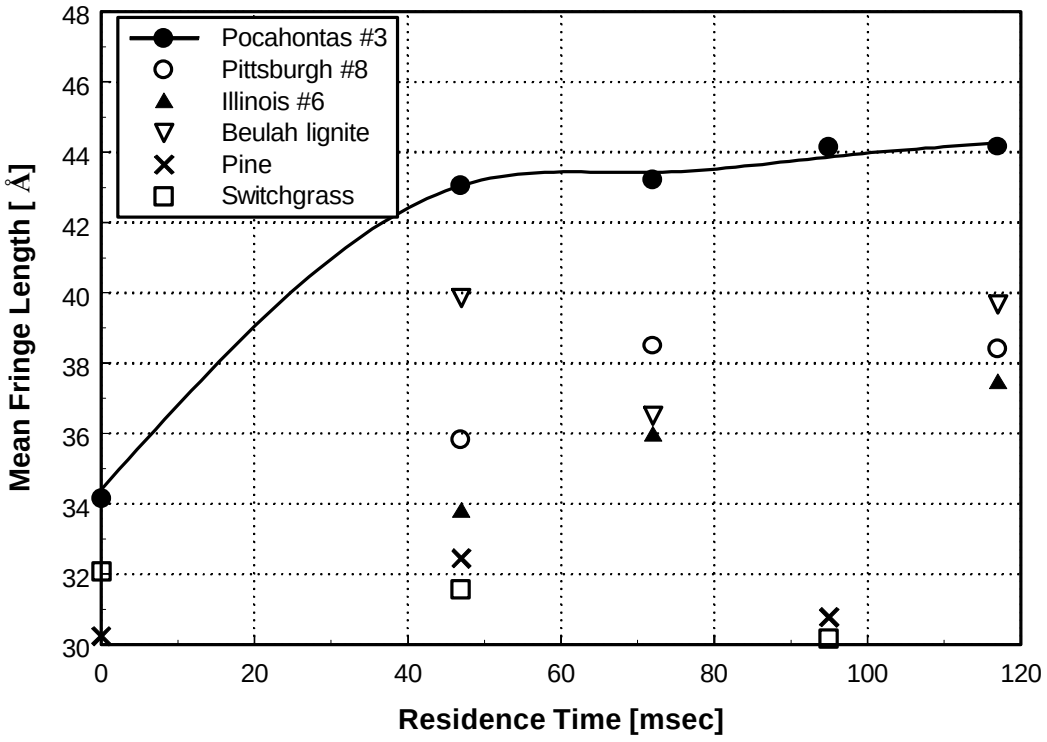

Figure 6-27 Summary of results for combustion-derived chars: mean fringe length vs. combustion residence time. Note: zero residence time represents the raw solid fuel. Image-to-image standard deviations are 1 – 3 Å, so the changes between range 47 and 117 msec are not statistically significant for some precursors.

6.3.2.2 Tortuosity

Figure 6-28 shows mean tortuosity determined from the HRTEM image analysis. Tortuoistiy represents the degree of curvature in the fringe. Tortuosity has a value larger than one for most cases and one for the straight line. As in Figure 6-27, high rank Pocahontas shows a big change from 0 msec (raw coal) to 47 msec. With one exception, the char samples show decreasing tortuosity values throughout the combustion. Beulah lignite and Pittsburgh #8 show increase from 47 to 72 msec and decrease to the value

lower than 47 msec one at 117 msec of residence time. High volatile Illinois #6 shows decrease throughout the combustion process and a tortuosity of residual carbon was calculated as 1.18. Two biomass samples, Southern Pine and Switchgrass show relatively high tortuosity and high statistical deviation image-to-image about 0.1, so the changes between 0 and 95 msec are not statistically significant.

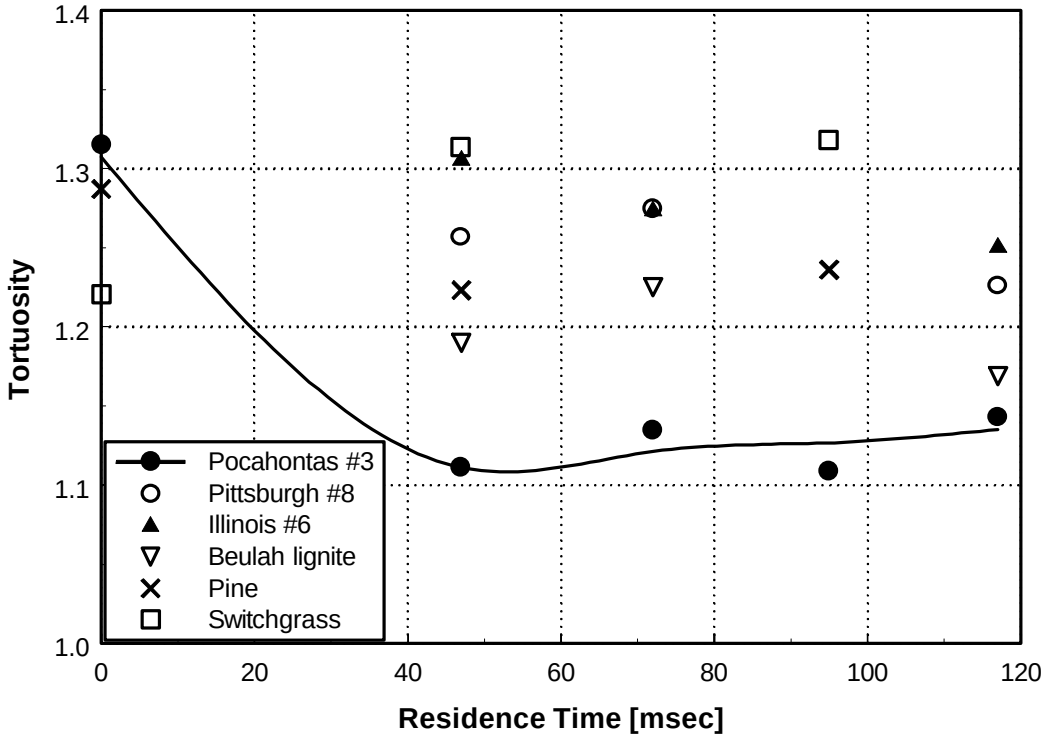

Figure 6-28 Summary of results for combustion-derived chars: mean tortuosity vs. combustion residence time. Note: zero residence time represents the raw solid fuel.

6.3.2.3 Apparent Crystalline Fraction

Apparent crystalline fraction represents the recognizable crystalline material in the image. As shown in Figure 6-29, the fraction shows the same trend as in mean fringe length (see Figure 6-27).

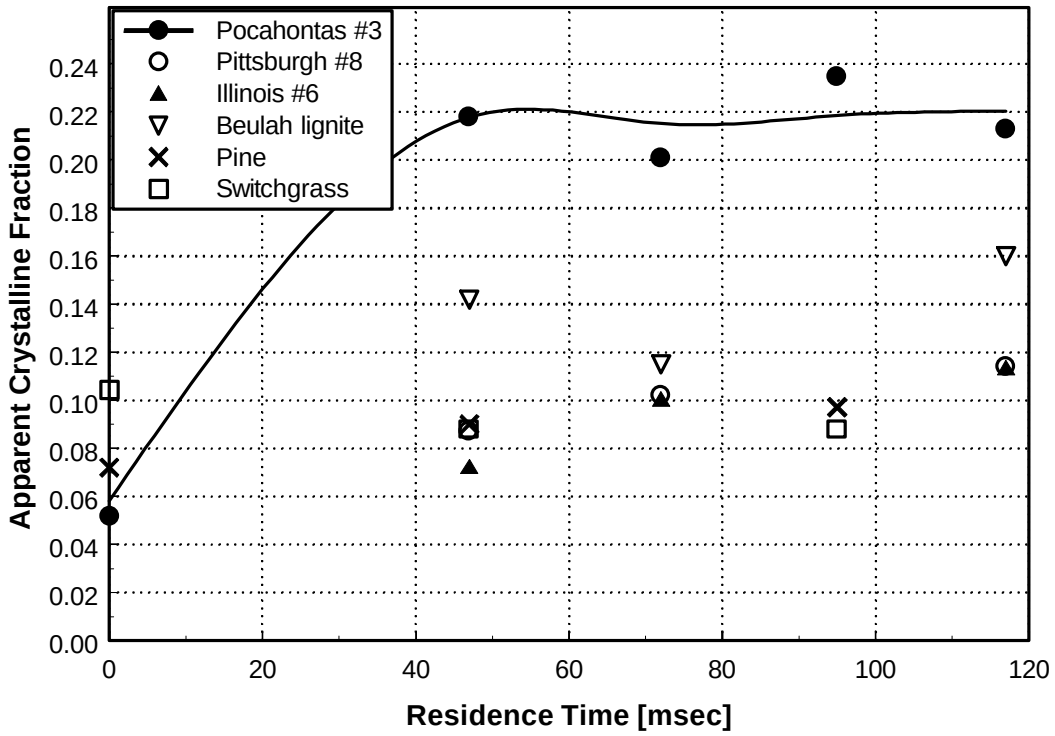

Figure 6-29 Summary of results for combustion-derived chars: apparent crystalline fraction vs. combustion residence time. Apparent crystalline fraction is the fraction of the image area covered by recognizable ordered material and is calculated as $SL_i/(SL_i)_{max}$ where $(SL_i)_{max}$ is computed for an ideal graphitic structure.

6.3.2.4 Nematic Order Parameter in 2D

Two different nematic order patterns are shown in Figure 6-30, which plots nematic order parameter (S_{m2N}) computed as a function of residence time. The high rank Pocahontas chars show a high S_{m2N} (~0.9) at long range (> 20 Å) after only 47 msec and maintain that high order throughout combustion. This indicates possible mesophase formation at early stage of combustion. Illinois shows increases from 47 msec to 72 and from 117 msec to 351 but a decrease from 72 msec to 117 msec. Residual carbon of this char is about 0.68.

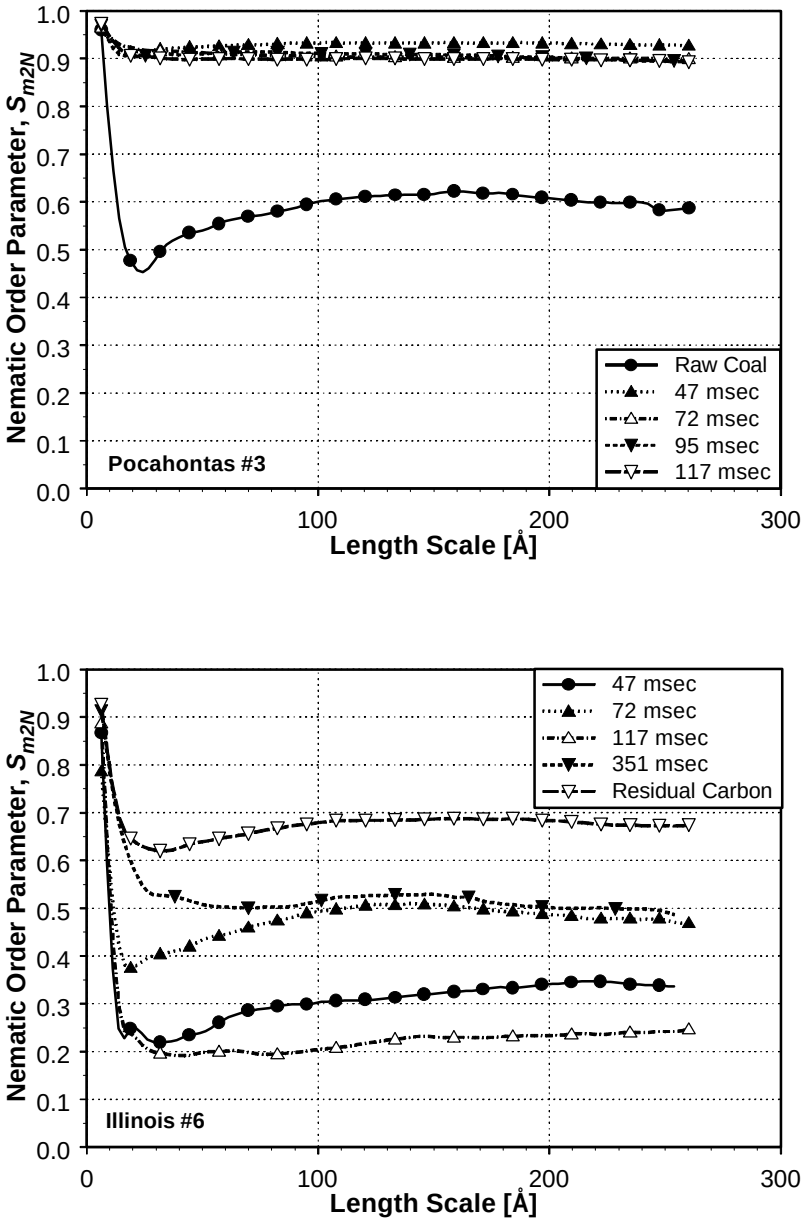

Figure 6-30 Nematic order parameter (S_{m2N}) of Pocahontas #3 and Illinois #6 chars as a function of length scale.

The whole image was scanned with 5 nm diameter circle, and S_{m2N} was calculated within the circle at each location and the results plotted as histograms (see Figure 6-31). From 47 msec to 117 msec, distributions show no significant shift. For residual carbon

from fly ash, a population at higher order increases, indicating the appearance of crystallites with sizes on the order of 5 nm or greater.

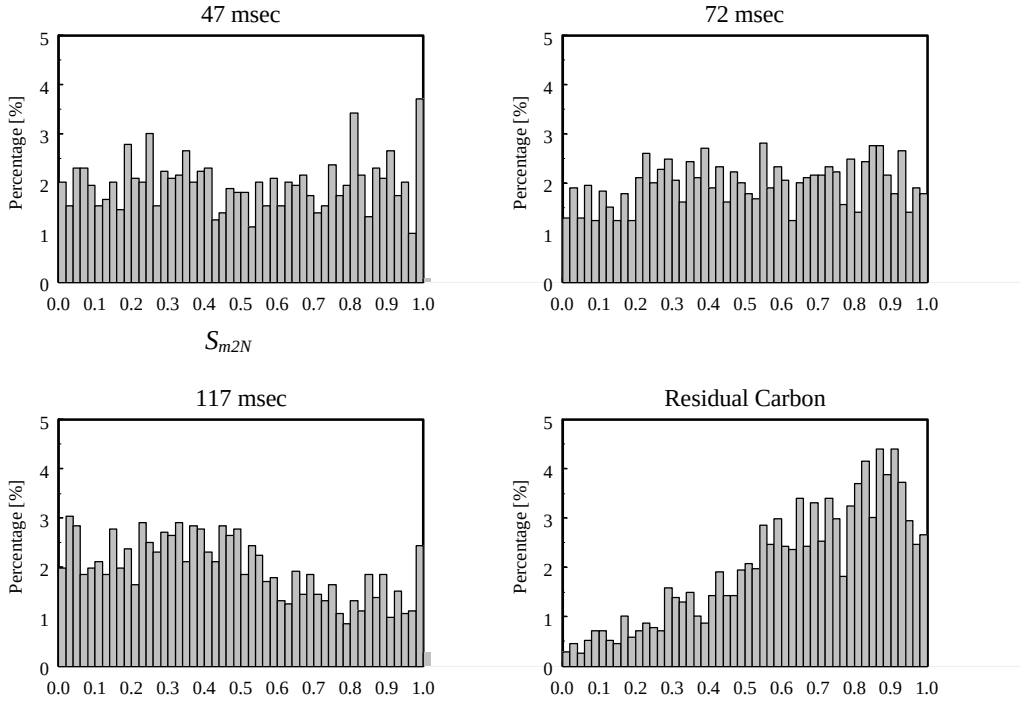

Figure 6-31 Distribution of S_{m2N} for Illinois #6 char samples as a function of residence time with 5 nm dia. over whole area in the image.

The same calculation has been carried out for Pocahontas #3 samples and is reproduced in Figure 6-32. Raw sample shows more or less uniform distribution over the whole possible orders. Only after 47 msec of residence time, Pocahontas samples show a significant shift of population to higher order.

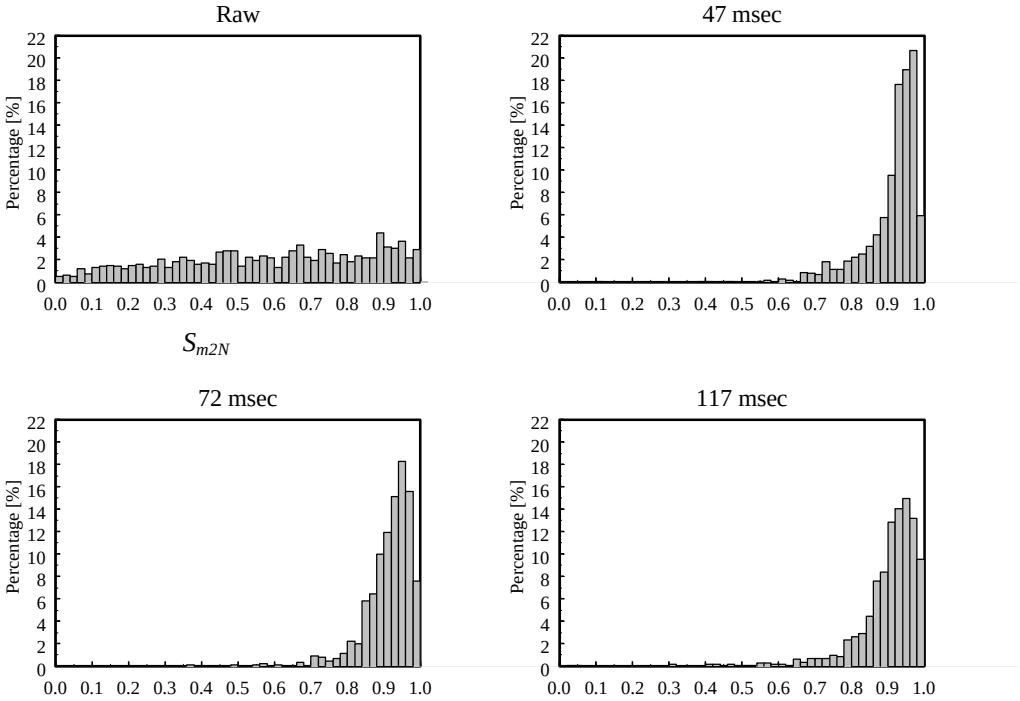

Figure 6-32 Distribution of S_{m2N} fraction in Pocahontas #3 as a function of residence time with 5 nm dia. over whole area in the image.

In summary, there are modest changes in nanostructure as a function of combustion conditions. Illinois #6 shows the largest changes; a significant increase in layer length, decrease in tortuosity, and increase in apparent crystalline fraction during combustion. Pittsburgh shows an increase in layer diameter and apparent crystalline fraction. Pocahontas shows a large increase in layer diameter and crystalline fraction from the raw coal to the chars, but little change during char combustion. The long-range orientational order is established early and does not alter appreciably during combustion. The other samples (lignite and biomass chars) show little changes in nanostructural parameters during combustion.

Overall, it may be said that the major features of char carbon nanostructure are established early in the flame. Only modest changes occur during the bulk of char combustion, and these changes are only observed for the high-volatile bituminous coals. A possible rationalization for these results is as follows. Pocahontas forms highly

anisotropic structures early, during the fluid stage of pyrolysis, and this eliminates the possibility for subsequent rearrangements of a substantial nature that could be easily observed by 002 LF imaging. The late-residence time Pocahontas sample still shows a "meandering" [41] rather than graphitic structure, in which the fringe orientation varies about the director. Apparently the elimination of defects and coalescence of graphene layers which occurs above about 1700 K [42] does not occur significantly under these conditions (100 msec, 1800K). The remaining coals solidify in a disordered state at the end of primary pyrolysis and have the potential to rearrange locally to more ordered states over the course of combustion. The two coals with the highest fluidity during pyrolysis and the least degree of crosslinking (Pittsburgh and Illinois) do undergo some further rearrangements. The biomass and lignite chars on the other hand are highly crosslinked and maintain their disordered states during combustion. This is particularly true of the biomass chars, which exhibit the least nanostructural order of all samples (and thus the most driving force for crystallization) yet show no tendency to develop order during combustion.

The relatively well developed short-range order in the lignite sample is an interesting feature which is not understood. Perhaps the abundant well-dispersed mineral matter which is unique to this sample, and which is responsible for the well-documented catalysis of the oxidation reaction at lower temperatures [6], is also active in catalytic graphitization events. In some locations, regions of circular crystallinity were observed in the vicinity of dark patches, reminiscent of partial carbon shell formation in the presence of inorganic impurities in some carbons [16]. Another contributing factor is the high reactivity of the lignite chars, which under combustion conditions leads to elevation of the particle temperature above the surrounding gas phase, and results in slightly higher peak particle temperatures for the lignite chars, which are estimated at the upper end of the previously quoted range, 1700 – 1900 K.

Figure 6-33 shows length-dependent nematic order parameters for four coal chars and two biomass-derived char sampled from high-temperature combustion environments. The chars are seen to vary greatly in the degree and length scale of orientational order. The switchgrass char shows a high degree of order at short length scales (below about 30 Å), but only a slight ordering tendency ($S_{m2N} < 0.25$) at longer length scales. This

behavior is typical of samples consisting of distinct crystallites or molecular orientation domains oriented nearly at random, and the length at which the order parameter decreases sharply can be used as a 002 LF-based definition of a molecular orientation domain. The same general behavior is observed for the lignite and high-volatile bituminous chars, although the long-range order parameters are higher (0.5 – 0.6). The Pocahontas char is distinctly different, having a high order parameter (S_{m2N} > 0.9) that is maintained at all length scales accessible to this technique (up to 300 Å). The high degree of order and long length scale indicates that the order in Pocahontas was established in the fluid phase through the formation of the liquid crystalline intermediate, carbonaceous mesophase.

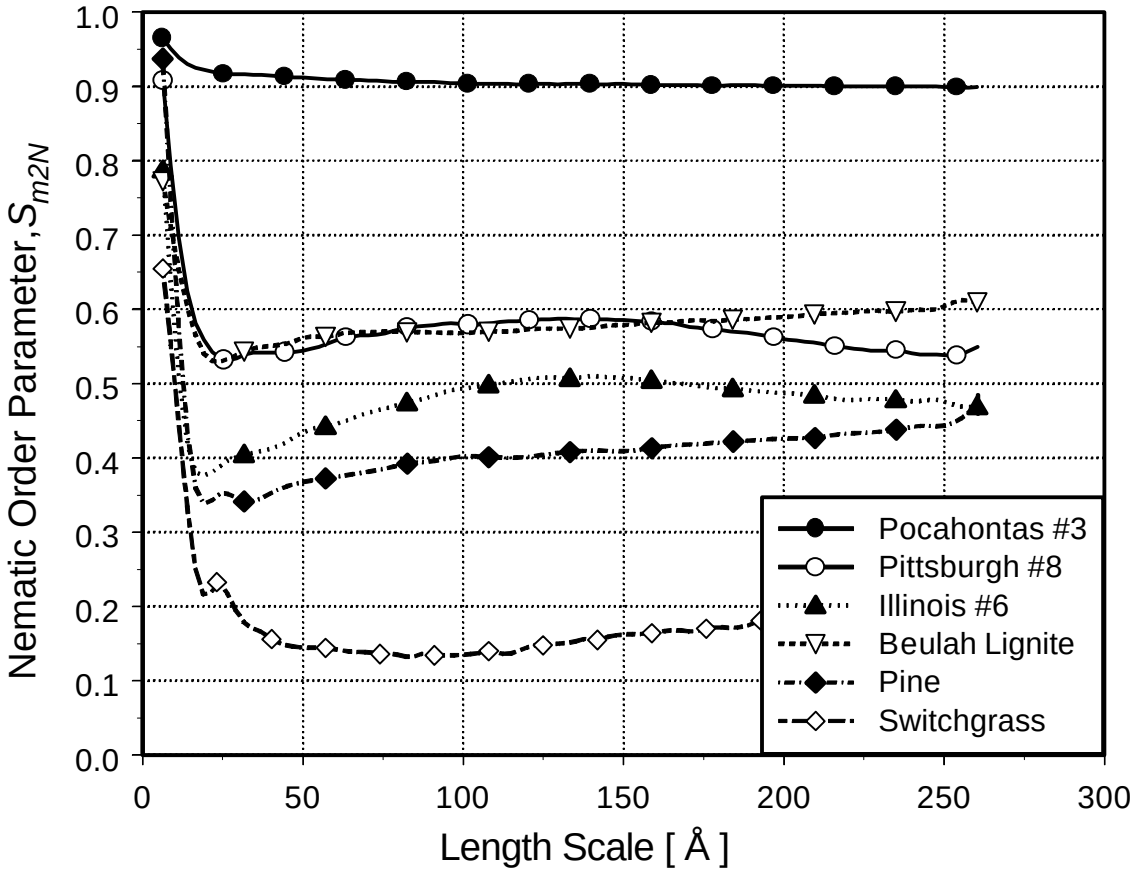

Figure 6-33 Summary of results for combustion-derived chars: modified, length-dependent nematic order parameters, S_{m2N} (r), for chars from six solid fuels. (72 msec for coal chars, 95 msec for biomass chars).

Especially noteworthy in this data set is the significant long-range order in all samples. Even after correction for the apparent order in random lines, each of the samples studied retains a statistically significant non-zero order parameter up to the maximum length scale studied (300 Å). Modified order parameters in the 0.5 – 0.6 range reflect a particularly significant alignment tendency for the three lower rank coals. The next section seeks to answer this question by comparing the long-range order parameters to theoretical predictions from the Maier-Saupe mean field theory for liquid crystals.

6.4 Reactivity and Structure Parameters

The reactivity of the carbon can be related to the size, tortuosity, and orientational order of graphene layers in three fundamental ways. First, as the layers increase in size, the amount of hydrogen and the ratio of reactive edge sites to unreactive interior sites decrease. Second, as the individual layers approach a more perfectly graphitic arrangement of aromatic units, active sites associated with defects, heteroatoms, or non-sp^2-hybridized carbon are lost. Third, as the aromatic layers reach more compact stacking arrangements, the microscopically available surface area decreases. For fast oxidation reactions such as high-temperature combustion, the ultrafine carbon structure can also affect reactivity through its effect on microporous diffusion coefficients [14]. Although the relationship between reactivity and crystalline order is more complex than this simple scheme suggests, reactivity does, in general, decrease with increasing degree of order across the spectrum of carbon materials.

To find a possible relationship between reactivity of char sample and structure parameters defined during this work, previously reported global reactivity data has been plotted vs. various structural parameters (see section 6.2 for the definition of the structure parameters) (see Figure 6-34, Figure 6-35, and Figure 6-36).

Mean fringe length is plotted against global reactivity in Figure 6-34. Reactivity tends to decrease as mean fringe length increases. This trend is clear among bituminous coals: high-volatile Illinois #6, Pittsburgh #8, and low-volatile Pocahontas. Beulah lignite, however, shows high reactivity compared to Illinois #6 at 72 msec residence time, but the two chars have similar mean layer length. The high reactivity of lignite is likely

due to the inorganic matter in the coal, mostly CaO species [6]. Figure 6-35 shows tortuosity vs. reactivity. The more tortuous the layers are, the higher the reactivity. Beulah Lignite is an outlier, again, showing an unusually high reactivity. Figure 6-36 shows the fractional area of image whose S_{m2N} is larger than 0.6 for a given size of 5 nm diameter. The S_{m2N} fraction correlates strongly with reactivity among bituminous coals.

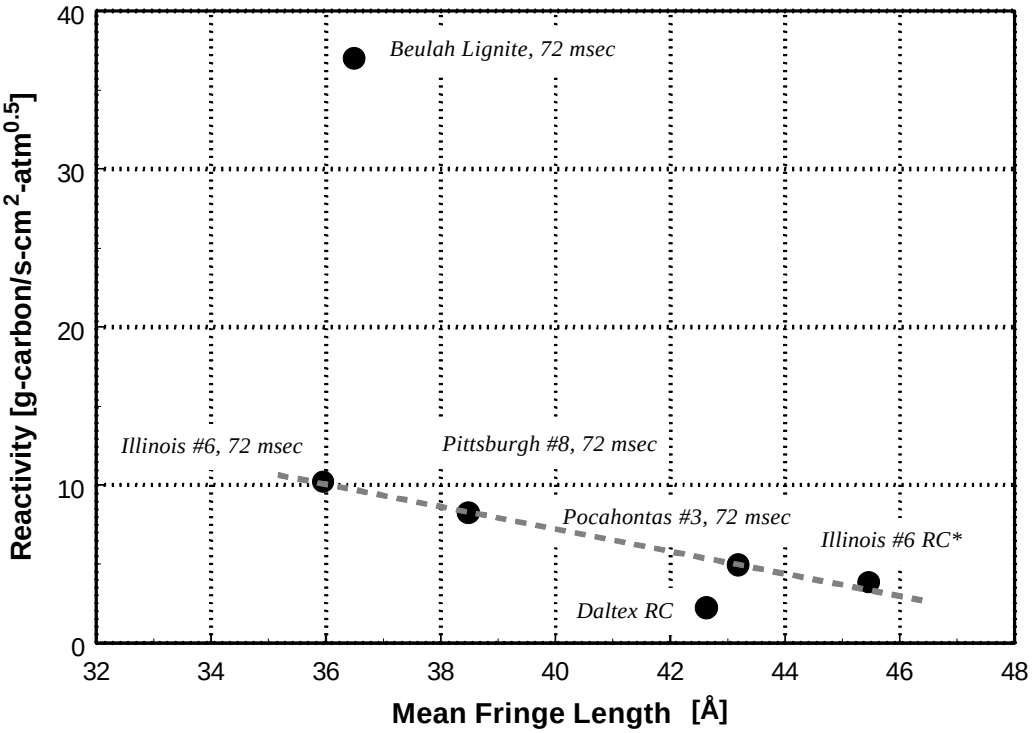

Figure 6-34 Global reactivity as a function of mean fringe length. Char samples were at the residence time of 72 msec. * RC: residual carbon from fly ash.

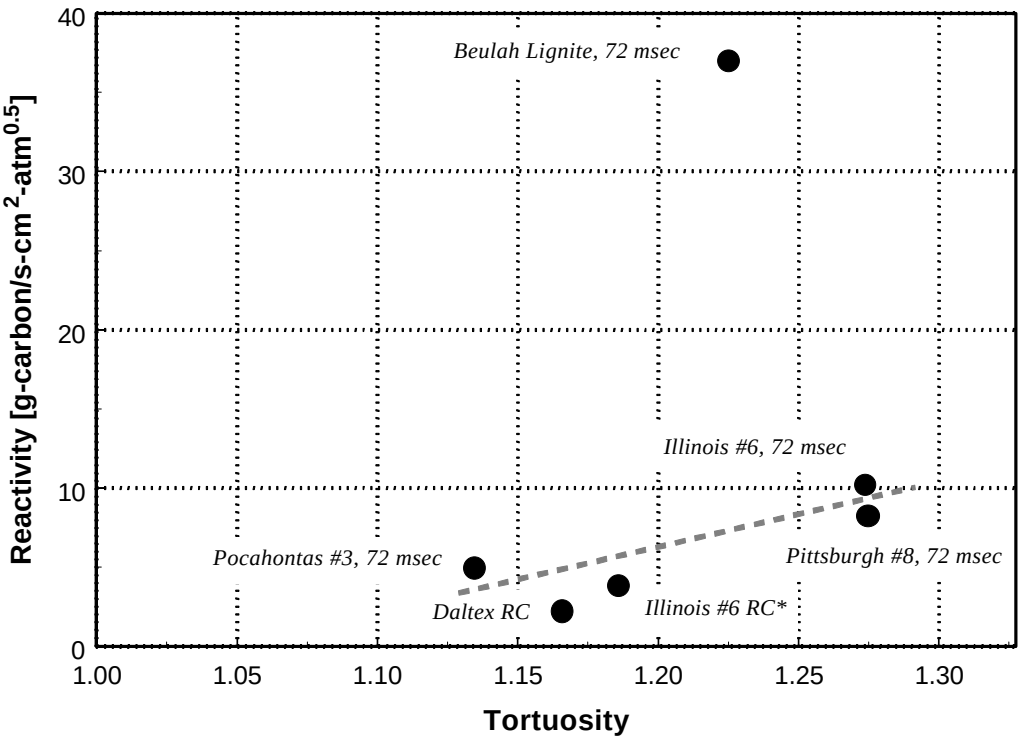

Figure 6-35 Reactivity as a function of tortuosity.

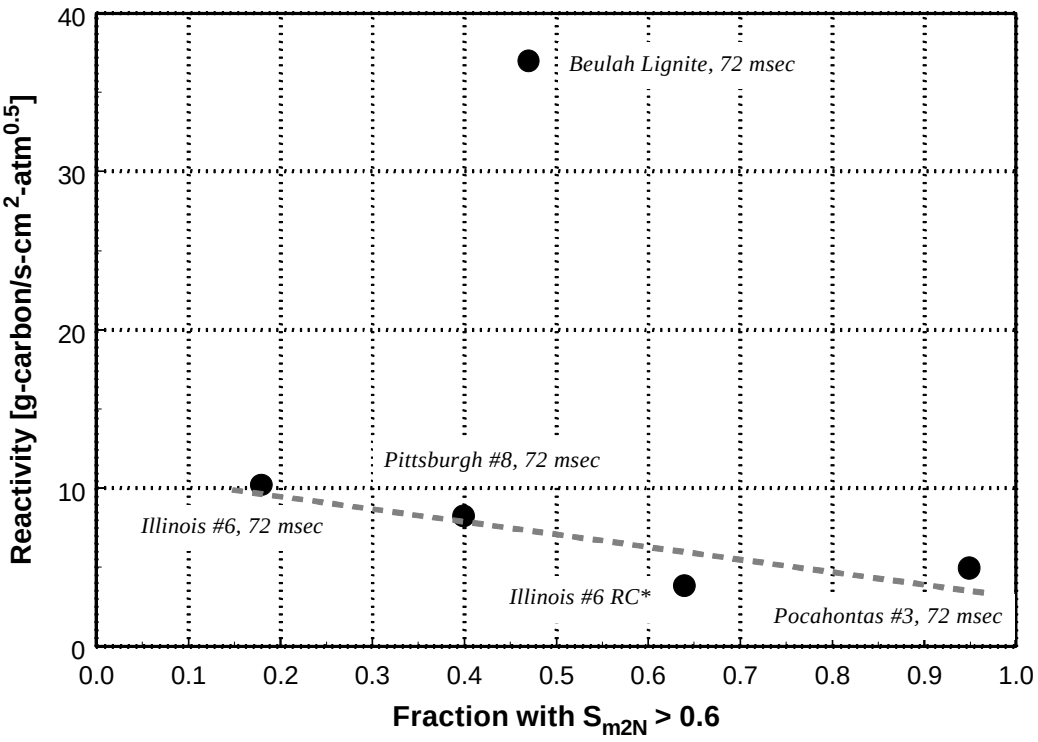

Figure 6-36 Global reactivity as a function of fraction with S_{m2N} > 0.6 with a given 5 nm region of interest.

In summary, the reactivities correlate strongly with the structure parameters which define the crystalline or mesoscale structures in the case of bituminous coals. The evolution of nanostructure of bituminous coals seems to be an important factor determining the oxidation reactivity during combustion. In the case of the lignite, catalytic effects might be more important than carbon structural effects. To better establish the link between the nanostructure and the reactivity, more data are needed.

7 CONCLUSIONS

This work generated new fundamental information on the nanoscale structures of carbonaceous solids and the dynamics of their transformations at high temperature. In addition, this study produced thermal deactivation data at temperatures equivalent to peak particle temperatures in commercial pulverized coal-fired boilers and residence times from 2 sec to 118 sec. The results of this research will provide a basis with which current and future entrained-flow combustion and gasification systems can be optimized for carbon burnout.

7.1 Characterization of Carbon Nanostructure

- An automated digital image processing technique for HRTEM 002 lattice fringe images has been developed that yields semi-quantitative statistics on fringe length and tortuosity, as well as new quantitative parameters describing the mode, degree, and length scale of orientational order. The absolute values of the mean layer length and tortuosity depend on parameters within the digital algorithm, and are therefore not free from subjectivity. The algorithm does yield useful relative indices. The orientational order indices are less sensitive to the choice of digital algorithm parameters and thus have more absolute significance.
- Five order parameters have been defined for quantitative description of simple order modes in disk-like objects in two and three dimensions. For analysis of single 002 LF images, only two order parameters are needed: one nematic and one polar, to represent mesophasic order, cylindrical radial order, and cylindrical concentric order. The order parameters have been corrected for small sample size, allowing values to be determined as a function of length scale-a key feature for characterizing the long and short range order found in carbon materials.

- During high temperature combustion of solid fuels, the major features of char nanostructure are established very early (τ < 50 msec). The young Pocahontas char exhibits long range orientational order, while the remaining materials show predominately short range orientational order. Subsequent combustion (50 msec < τ < 120 msec, T = 1700 – 1900 K) is accompanied by modest increases in layer length, increases in apparent crystalline fraction, and decreases in tortuosity for the high volatile bituminous coal chars. Chars from lower rank coals, as well as the biomass chars, show very little nanostructural rearrangement during the char combustion stage. Chars from the high-rank, low-volatile bituminous coal establish long-range, meandering orientational order early that is unchanged by subsequent combustion.
- A noteworthy observation is the presence of two distinct length scales for orientational order in all but the highest rank solid fuel chars. At short length scales (< 30 Å) a high degree of orientational order is observed reflecting the presence of more-or-less distinct crystallites, or small molecular orientation domains. At larger length scale (> 30 Å), a lesser but significant orientational order is still present, indication that the domains themselves have statistical preference for orientational order.
- HRTEM analysis of high temperature combustion chars reveals large differences in crystal structure as a function of parent coal type and lesser but significant differences as a function of combustion residence time for a given coal char. Generally, as rank or residence time increases, the graphene layers become longer, more nearly planar (less tortuous), and statistically better aligned. Among the bituminous coal chars, reactivity trends show a significant correlation with changes in the crystalline or mesoscale structures observed by HRTEM.

- Among the bituminous coal chars, reactivity trends show a significant correlation with changes in the crystalline or mesoscale structures observed by HRTEM

7.2 Transient Thermal Deactivation

- A new device has been developed for exposing captive powder samples to combustion-like thermal histories while maintaining inert gas environments. The all graphite system is capable of peak temperatures above 3000 K, heating rates of 103 K/s, and hold times at peak temperature from 2 - 200 seconds. Compared to high temperature wire meshes, this graphite system has an advantage that there is no metallic contamination at high temperature and a disadvantage that it cannot do pyrolysis experiments since most volatile matters must be removed prior to heat treatment.
- The intrinsic oxygen reactivity of solid fuel chars is found to decrease dramatically with increasing peak temperature, even for hold times as short as 2 seconds. A typical solid fuel char experiences over three orders of magnitude decrease in reactivity when peak temperature is increased from 700 to 2400 oC.
- The higher reactivity materials generally show a higher propensity for annealing, although there are specific exceptions to this trend. For the set of organic precursors studied here, the reactivity of the 700 oC chars spans 3 1/2 orders of magnitude. The higher annealing propensity of the higher reactivity fuels reduces this variation to 2 orders of magnitude for 1800 oC chars. Excluding the anthracite char, the set of 2400 oC carbons have reactivities lying within a factor of only 10.

- The two highest rank coals show very different annealing behavior, although their low temperature chars have similar reactivities. The higher annealing propensity of the anthracite correlates with its higher degree of structural ordering during heat treatment as revealed by HRTEM.

8 REFERENCES

1 Hurt, R. H.; Gibbins, J. R. *Fuel* **1995**, 74, 471.

2 Beeley, T. J.; Gibbins, J. R.; Mau, C. K.; Pendlebury, K. J.; Williamson, J.; Hurt, R. H., *ACS Preprint, ACS National Meeting*, San Diego, Mrach 1994.

3 Gibb, W., *personal communication*, 1994.

4 Man, C.K.; Beeley, T.J.; Gibbins, J.; Lockwood, F.C.; Williamson, J.; Crelling, J.C.; Hurt, R.H. *Proceedings of the EPRI Conference on the Effects of Coal Quality on Power Plants*, Charleston, S.C., August, 1994.

5 Johnson, C. A.; Patrick, J. W.; Thomas, K. M. *Fuel* **1986**, 65, pp. 1284-1290.

6 Radovic, L. R.; Walker, P. L. Jr.; Jenkins, R. G. *Fuel* **1983**, 62, 849.

7 Suuberg, E.M., in *Fundamental Issues in Control of Carbon Gasification Reactivity* (J. Lahaye and P. Ehrburger, Eds.), 1991, Kluwer, the Netherlands, pp.269-305.

8 Smith, I.W.; Tyler, R.J. *Fuel* **1972**, 51, 312.

9 Levendis, Y.A.; Flagan, R.C., *Combust. Sci. and Tech.* **1987**, 53, 117.

10 Hurt, R.H. *Energy Fuels* **1993**, 7, 721.

11 Hurt, R.H.; Davis, K.A., *Twenty-Fifth Symposium (International) on Combustion*, The Combustion Institute, 1994, 561.

12 Davis, K. A.; Hurt, R. H.; Yang, N. Y. C.; Headley, T. J. *Combust. Flame* **1995**, 100, pp. 31-40.

13 Donnet, J. B., *Carbon*, 1982, **20**, pp. 267-282.

14 Valix, M. G.; Harris, D. J.; Smith, I. W.; Trimm, D. L. *24th Symp. (Int.) on Combustion*, The Combustion Institute, Pittsburgh, PA, 1992, pp. 1217-1223.

15 Marsh, H.; Diez, M.A.; Kuo, K. in *Fundamental Issues in Control of Carbon Gasification Reactivity* (J. Lahaye and P. Ehrburger, Eds.), 1991, Kluwer, the Netherlands, pp205-220.

16 Oberlin, A., in *Chemistry and Physics of Carbon*, Vol. 22, ed. P. A. Thrower, Marcel Dekker, New York, 1989, pp. 1-143.

17 Lewis, I.C. *Carbon* **1982**, 20, 519.

18 Wornat, M. J.; Hurt, R. H.; Yang, N. Y. C.; Headley, T. J. *Combust. Flame* **1995**, 100, pp. 131-143.

19 Fletcher, T.H., *personal communication*, 1993.

20 Hurt, R.H.; Davis, K.A.; Yang, N.Y.C.; Headley, T.J.; Mitchell, G.D. *Fuel* **1995**, 74, 1297.

21 Dobb, M.G.; Guo, H.; Johnson, D.J. *Carbon* **1995**, 33, 1115.

22 Palotás, Á. B.; Rainey, L. C.; Feldermann, C. J.; Sarofim, A. F.; Vander Sande, J. B. *Microsc. Res. Tech.* **1996**, 33, pp. 266-278.

23 Walker, P. L. Jr. *Fuel* **1981**, 60, 297.

24 Hyde, W.D.; Hecker, W.C.; Cope, R.F.; Painter, M. M.; McDonald, K.M.; Bartholomew, C.H. 1989 Western States Catalysis Meeting, Denver, CO, 1989.

25 Chitsora, C.T.; Muhlen, H.J.; Van Heek, K. H.; Juntgen, H. *Fuel Process. Technol.* **1987**, 15, 17.

26 Jenkins, R. G.; Nandi, S. P.; Walker, P. L., Jr. *Fuel* **1973**, 52, 288.

27 Rybak, W. *Fuel Process. Technol.* **1988**, 19, 107.

28 Shim, H. -S. "Nanostructure and Oxidation Reactivity of Carbons Prepared by Rapid Heating" Ph.D. Thesis (Chemistry), Brown University, Providence, RI (1999).

29 Sarofim, A. F. personal communication, 1995.

30 Short, M. A.; Walker, P. L. Jr. *Carbon* **1963**, 1, pp. 3-9.

31 Cullity, B. D. in *Elements of X-ray diffraction*, 2nd ed., Addison-Wesley Publishing Company, London, 1978, p. 383.

32 Johnson, C.A.; Patrick, J.W.; Thomas, K.M. *Fuel* **1986**, 65, 1284.

33 Inagaki, M. *Carbon* **1997**, 35, 711.

34 De Gennes P.G.; Prost, J. *The Physics of Liquid Crystals*, Clarendon Press, Oxford, 1993.

35 Hicklas, K.; Bopp, P.; Brickmann, J. *J. Chem. Phys.* **1994**, 101, 3157.

36 Mitchell, R. E. *Twenty-Second Symposium (International) on Combustion*, The Combustion Institute, 1988, pp. 69-78.

37 Mitchell, R. E.; Hurt, R. H.; Baxter, L. L.; Hardesty, D. R. Sandia National Laboratories Report No. SAND92-8208, 1992.

38 Tichenor, D. A.; Mitchell, R. E.; Hencken, K. R.; Niksa, S. *Twentieth Symposium (International) on Combustion*, The Combustion Institute, Pittsburgh, 1984, p. 1249.

39 Rouzaud, J.N.; Oberlin, A. *Carbon* **1989**, 27, 517.

40 Rouzaud, J. N.; Oberlin, A. Chapt. 17 in *Advanced Methodologies in Coal Characterization*, Elsevier, Amsterdam, 1990.

41 Dobb, M.G.; Guo, H.; Johnson, D.J. *Carbon* **1995**, 33, 1115.

42 Emmerich, F.G. *Carbon* **1995**, 33, 1709.